



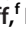
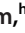







# The Cytomegalovirus M35 Protein Directly Binds to the Interferon- $\beta$ Enhancer and Modulates Transcription of *Irfn1* and Other IRF3-Driven Genes

 Hella Schwanke,<sup>a,b</sup>
 Vladimir Gonçalves Magalhães,<sup>b</sup>
 Stefan Schmelz,<sup>c</sup>
 Emanuel Wyler,<sup>d</sup>
 Thomas Hennig,<sup>e</sup>
 Thomas Günther,<sup>f</sup>
 Adam Grundhoff,<sup>f</sup>
 Lars Dölken,<sup>e</sup>
 Markus Landthaler,<sup>d,g</sup>
 Marco van Ham,<sup>h</sup>
 Lothar Jänsch,<sup>h,i</sup>
 Konrad Büssov,<sup>c</sup>
 Joop van den Heuvel,<sup>c</sup>
 Wulf Blankenfeldt,<sup>c,j</sup>
 Caroline C. Friedel,<sup>k</sup>
 Florian Erhard,<sup>e</sup>
 Melanie M. Brinkmann<sup>a,b</sup>

<sup>a</sup>Institute of Genetics, Technische Universität Braunschweig, Braunschweig, Germany

<sup>b</sup>Virology and Innate Immunity Research Group, Helmholtz Centre for Infection Research, Braunschweig, Germany

<sup>c</sup>Department Structure and Function of Proteins, Helmholtz Centre for Infection Research, Braunschweig, Germany

<sup>d</sup>Berlin Institute for Medical Systems Biology, Max Delbrück Center for Molecular Medicine, Helmholtz Association, Berlin, Germany

<sup>e</sup>Institute for Virology and Immunobiology, Julius-Maximilians-Universität Würzburg, Würzburg, Germany

<sup>f</sup>Leibniz Institute of Virology, Hamburg, Germany

<sup>g</sup>Institute for Biology, Humboldt-Universität zu Berlin, Berlin, Germany

<sup>h</sup>Cellular Proteome Research Group, Helmholtz Centre for Infection Research, Braunschweig, Germany

<sup>i</sup>Institute for Microbiology, Technische Universität Braunschweig, Braunschweig, Germany

<sup>j</sup>Institute for Biochemistry, Biotechnology and Bioinformatics, Technische Universität Braunschweig, Braunschweig, Germany

<sup>k</sup>Institute of Informatics, Ludwig-Maximilians-Universität München, Munich, Germany

Vladimir Gonçalves Magalhães and Stefan Schmelz contributed equally. Author order is alphabetical.

**ABSTRACT** Induction of type I interferon (IFN) gene expression is among the first lines of cellular defense a virus encounters during primary infection. We previously identified the tegument protein M35 of murine cytomegalovirus (MCMV) as an essential antagonist of this antiviral system, showing that M35 interferes with type I IFN induction downstream of pattern-recognition receptor (PRR) activation. Here, we report structural and mechanistic details of M35's function. Determination of M35's crystal structure combined with reverse genetics revealed that homodimerization is a key feature for M35's immunomodulatory activity. In electrophoretic mobility shift assays (EMSAs), purified M35 protein specifically bound to the regulatory DNA element that governs transcription of the first type I IFN gene induced in nonimmune cells, *Irfn1*. DNA-binding sites of M35 overlapped with the recognition elements of interferon regulatory factor 3 (IRF3), a key transcription factor activated by PRR signaling. Chromatin immunoprecipitation (ChIP) showed reduced binding of IRF3 to the host *Irfn1* promoter in the presence of M35. We furthermore defined the IRF3-dependent and the type I IFN signaling-responsive genes in murine fibroblasts by RNA sequencing of metabolically labeled transcripts (SLAM-seq) and assessed M35's global effect on gene expression. Stable expression of M35 broadly influenced the transcriptome in untreated cells and specifically downregulated basal expression of IRF3-dependent genes. During MCMV infection, M35 impaired expression of IRF3-responsive genes aside of *Irfn1*. Our results suggest that M35-DNA binding directly antagonizes gene induction mediated by IRF3 and impairs the antiviral response more broadly than formerly recognized.

**IMPORTANCE** Replication of the ubiquitous human cytomegalovirus (HCMV) in healthy individuals mostly goes unnoticed but can impair fetal development or cause life-threatening symptoms in immunosuppressed or -deficient patients. Like other herpesviruses, CMV extensively manipulates its hosts and establishes lifelong latent infections. Murine CMV (MCMV) presents an important model system as it allows the study of CMV infection in the host organism. We previously showed that during entry into host cells,

**Editor** Anna Ruth Cliffe, University of Virginia

**Copyright** © 2023 Schwanke et al. This is an open-access article distributed under the terms of the [Creative Commons Attribution 4.0 International license](https://creativecommons.org/licenses/by/4.0/).

Address correspondence to Melanie M. Brinkmann, [m.brinkmann@tu-braunschweig.de](mailto:m.brinkmann@tu-braunschweig.de).

The authors declare no conflict of interest.

**Received** 17 March 2023

**Accepted** 4 May 2023

**Published** 8 June 2023

MCMV virions release the evolutionary conserved protein M35 protein to immediately dampen the antiviral type I interferon (IFN) response induced by pathogen detection. Here, we show that M35 dimers bind to regulatory DNA elements and interfere with recruitment of interferon regulatory factor 3 (IRF3), a key cellular factor for antiviral gene expression. Thereby, M35 interferes with expression of type I IFNs and other IRF3-dependent genes, reflecting the importance for herpesviruses to avoid IRF3-mediated gene induction.

**KEYWORDS** M35, type I interferon (IFN) response, IRF3, DNA-binding protein, SLAM sequencing (SLAM-seq), IRF3-dependent genes, interferon-stimulated genes (ISG), MCMV, cytomegalovirus, herpesvirus, innate immunity, immune evasion, pp85 protein superfamily, U14, PRR signalling

Upon host cell infection, viruses promptly encounter the first line of immune defense intrinsic to all nucleated cells, the type I interferon (IFN) response (1). As an integral part of the innate immune system, type I IFN production is activated within a few hours of infection and links detection of a pathogen to induction of an antiviral state in infected and neighboring cells and ultimately in the entire organism. Type I IFNs invoke a broad transcriptional response that induces a cell-intrinsic defense program including specific antiviral mechanisms, induction of proapoptotic and anti-proliferative pathways, and activation of the adaptive immune system. Accordingly, the type I IFN response is essential for the host organism to control infection (reviewed in references 2 and 3).

Expression of type I IFNs is induced upon detection of pathogen-associated molecular patterns (PAMPs) by an array of pattern-recognition receptors (PRRs) (4). The activation signal is subsequently relayed through adaptor proteins and kinases to the transcription factors activator protein 1 (AP-1), nuclear factor  $\kappa$ B (NF- $\kappa$ B), interferon regulatory factor 3 (IRF3), and IRF7, which induce expression of specific sets of genes: AP-1 dimers regulate genes involved in cell proliferation, differentiation, and apoptosis (5); NF- $\kappa$ B activates proinflammatory gene expression (6); IRF3 and IRF7 together regulate expression of IFN- $\alpha$  subtypes (7–9); and NF- $\kappa$ B and IRF3 or IRF7 together with an AP-1 heterodimer of ATF2 and c-Jun are required to activate transcription of the gene encoding IFN- $\beta$  (*Irfb1*) (10–13). Many cell types secrete IFN- $\beta$  as the very first response to infection, and immune cells also produce specific subtypes of IFN- $\alpha$ . These type I IFNs are in turn recognized by the type I IFN receptor, which is comprised of the two interferon- $\alpha/\beta$  receptor (IFNAR) subunits, IFNAR1 and IFNAR2. Activation of IFNAR signaling leads to assembly of signal transducer and activator of transcription (STAT) 1, STAT2, and IRF9 to transcription factor complexes, mainly interferon-stimulated gene factor 3 (ISGF3), finally culminating in induction of hundreds of interferon-stimulated genes (ISGs) (14, 15). In addition, transcription of a small set of ISGs, including *Isg15*, *Irf1*, *Irf2*, *Irf3*, *Mx1*, *Mx2*, and *Rsad2*, is directly activated by IRF3, giving rise to their designation as IRF3-dependent ISGs (16, 17). During viral infection, this IRF3-mediated shortcut in the type I IFN-mediated antiviral response enables induction of gene expression before or in the absence of IFNAR activation (9, 18–20). Thus, IRF3-dependent gene expression provides the host cell with the ability to immediately deploy some of the best studied ISGs to counter the commencing viral infection (21–24).

While the ubiquitously expressed IRF3 is critical to initiate the very first round of type I IFN signaling (8, 25, 26), IRF7 is an ISG itself and crucial for inducing high levels of ISGs and appropriate diversification of the immune response in later rounds of type I IFN signaling, including the upregulation of *Irfn* genes (7, 8, 26–28). The expression of *Irfb1* is first induced by IRF3 and then maintained by IRF7, as these two IRFs can equally transactivate the enhancer element that regulates induction of *Irfb1* (8, 9). Upon PRR signaling, four transcription factor dimers together with cofactors bind to this IFN- $\beta$  enhancer and cooperatively induce *Irfb1* expression (29, 30): one AP-1 heterodimer of ATF-2 and c-Jun, two dimers of IRF3 and/or IRF7, and one NF- $\kappa$ B heterodimer of p50 and p65. The two IRF3 and/or IRF7 dimers bind to four overlapping IRF-recognition elements (IREs) in the center of the IFN- $\beta$  enhancer, with each of the four DNA-binding domains contacting one 5'-

GAAA-3' consensus core element (31–33). The precise sequence arrangement of the IFN- $\beta$  enhancer, together with the structural orientation of the DNA-binding domains bound to this sequence, indicates that the two IRF3/7 dimers bind from opposite sites to the DNA helix to overlapping parts of the sequence (29, 34).

For successful propagation, viruses as obligate intracellular parasites have evolved a multitude of mechanisms to inhibit, circumvent, or modulate the type I IFN response of their hosts at all levels (reviewed in references 30, 35, and 36). Especially, members of the *Herpesviridae* are well known for their many gene products that manipulate the host cells to allow the establishment of lifelong infections. Human cytomegalovirus (HCMV) of the *Betaherpesvirinae* subfamily infects most humans early in life and reaches a seroprevalence of about 83% in the global adult population (37). Different organs and cell types, including fibroblasts, monocytes, endothelial, and epithelial cells, can be infected during primary infection with CMV, with fibroblasts representing the standard cell culture model (38, 39). The type I IFN response is critical to control CMV infection and to protect the host from progression of pathogenesis, although it does not suffice to eliminate CMV from the organism (40–44). Instead, the virus enters a latent state in specific cells of the myeloid lineage, from which it can reactivate under certain conditions (45, 46). Active CMV replication can be life-threatening in immunocompromised patients or be transmitted to a fetus during pregnancy and severely impair development of the unborn child, making congenital CMV infection the leading viral cause of birth defects worldwide (46–48).

To complement cell culture studies of strictly species-specific HCMV, murine CMV (MCMV) presents a well established model system that enables characterization of immune responses in the host organism (reviewed in references 49 and 50). The first identified antagonist of the type I IFN response of MCMV was M27, which impairs IFNAR signaling by targeting STAT2 (51, 52). However, M27 alone does not suffice to efficiently shut off the type I IFN response in macrophages (53), and we identified the tegument protein M35 as the first MCMV antagonist of PRR-mediated *Irfb1* transcription (54) and later on the MCMV m152 protein as a modulator of the adapter protein stimulator of interferon genes (STING) of the DNA-sensing PRR cyclic GMP-AMP synthase (cGAS) (55). Both M35 and its HCMV homolog UL35 are packaged into the virus particles as part of the tegument and therefore enter the host cell directly during infection, and both inhibit type I IFN signaling downstream of cGAS, as well as of the RNA sensor retinoid acid-inducible gene I (RIG-I), but upstream of IFNAR signaling (54, 56, 57). While UL35 impairs signaling at the level of the Tank-binding kinase 1 (TBK1) upstream of transcription factor activation (57), the presence of M35 impairs neither phosphorylation-mediated activation nor nuclear translocation of IRF3 or of the NF- $\kappa$ B subunit p65 (54). By creating viruses deficient for production of UL35 or M35, we determined that these proteins are required for viral control of the type I IFN response and efficient replication in cell culture (54, 57). Consistently, M35-deficient MCMV replicates to lower titers than wild-type (WT) MCMV in mice and does not reach the salivary glands, the organ from which MCMV would spread to the next host (54).

Our observation that MCMV-delivered M35 entered the nucleus prior to activated p65 during infection (54), combined with the fact that p65 is the first and a rate-limiting transcription factor recruited to the IFN- $\beta$  enhancer after induction of PRR signaling (58, 59), emphasizes how fast M35 reaches the nucleus. Moreover, M35-mediated inhibition of *Irfb1* expression was observable both in the context of infection and upon ectopic expression of M35, implying that no further viral factors were required for M35's immunomodulatory activity (54). This underlines the critical role of M35 for successful viral replication and suggests similar importance for the homologous proteins in other herpesviruses, like UL35 of HCMV. However, the exact mechanism of action of M35 remained to be determined. Here, we report on the structural and mechanistic details of M35's immunomodulatory activity. Our results suggest that M35 forms homodimers that directly bind to specific DNA sequences to antagonize recruitment of IRF3 to the promoters of antiviral genes and thus impair the IRF3-driven immediate antiviral response.

## RESULTS

### Purified M35 specifically binds to the sequence of the IFN- $\beta$ enhancer *in vitro*.

Based on our previous findings showing that M35 localizes in the nucleus and antagonizes PRR signaling downstream of transcription factor activation, we hypothesized that M35 might affect *Irfb1* induction by direct binding to the IFN- $\beta$  enhancer. To test for DNA interaction *in vitro* and potentially learn more about M35's structural features, we purified the M35 protein. Since previous analyses of HHV6B U14, a homolog of M35, indicated that the C-terminal part of the proteins was disordered (60), we generated expression constructs for purification of full-length M35 (amino acids [aa] 2 to 519; M35\_FL) and a short version of M35 (aa 2 to 452; M35\_S) corresponding to the structured U14 N-terminal domain (aa 2 to 458). The M35 coding regions were N-terminally fused to a Twin-Strep tag via a tobacco etch virus (TEV) protease cleavage sequence (NStr-; Fig. 1A) for removal of the tag after primary protein purification. Comparable amounts of NStr-M35\_S and NStr-M35\_FL were obtained from transiently transfected High-Five insect cells (Fig. 1B); however, the NStr-M35\_FL eluates contained a second, slightly lower band (Fig. 1B, lanes 7 and 8). As expected, this indicated that the full-length protein could not be purified to homogeneity due to a cleavage site or breakage point. In addition, NStr-M35\_FL and M35\_FL displayed a strong tendency to precipitate, especially at temperatures below 4°C. In contrast, M35\_S could readily be purified after removal of the N-terminal tag. To confirm that the absence of the C terminus did not hinder the immunomodulatory activity of the M35\_S protein, we assessed the effect of M35\_S on the induction of the *Irfb1* promoter (Fig. 1C and D). We cotransfected an expression plasmid encoding the adaptor protein of the RNA sensor RIG-I, mitochondrial antiviral-signaling protein (MAVS), to stimulate expression of a reporter plasmid expressing a luciferase gene under the control of the *Irfb1* promoter (Fig. 1D, EV). As demonstrated before (54), coexpression of full-length M35 with a C-terminal V5/His epitope tag (M35-V5/His) strongly inhibited the induction of the *Irfb1* reporter, and so did coexpression of M35\_S (Fig. 1D). The C-terminal part of M35 is thus not required for its immunomodulatory activity upon ectopic expression, and we focused on M35\_S in the following.

Next, we assessed the ability of M35\_S to bind to DNA in an electrophoretic mobility shift assay (EMSA), using double-stranded DNA (dsDNA) probes with 5'-biotin labels for detection (Fig. 1E). We previously showed that M35 inhibits induction of the human, as well as of the murine *Irfb1* promoter (54). This suggested recognition of both sequences in the case of direct M35-DNA interaction. Since the precise contact sites of the different transcription factors with the DNA nucleotides are known in the human IFN- $\beta$  enhancer (34, 61), this sequence served as main probe to study specific binding (Bio-IFN $\beta$ ). Incubation of increasing amounts of M35\_S (0.1, 1, and 10  $\mu$ M) with the Bio-IFN $\beta$  probe led to a dose-dependent mobility shift, reflecting formation of a protein-DNA complex (Fig. 1E). At 10  $\mu$ M M35\_S protein, a second band with a lower electrophoretic mobility appeared. Addition of a 100-fold excess of an unlabeled competitor greatly reduced the signal of the M35-DNA complex, indicating sequence specificity. Incubation of M35\_S with a biotinylated control probe harboring a random sequence with the same GC content (Bio-scrambled) did not detectably shift the biotin signal, further confirming the specificity of M35 binding to the IFN- $\beta$  enhancer sequence. To determine the binding affinity of M35\_S for DNA, we performed a more detailed titration series of M35\_S in the EMSA using the murine IFN- $\beta$  enhancer sequence as biotinylated probe to provide the natural target sequence M35 encounters in infection (Fig. S1A). Quantification of the probe signals at increasing concentrations of M35\_S (Table S1) and fitting of the data to a saturation model for specific binding returned a dissociation constant ( $K_d$ ) of 2.065  $\mu$ M, with a Hill coefficient ( $h$ ) of 2.775, suggesting cooperativity (Fig. 1F).

From these data, we conclude that the first 452 amino acids of M35 are sufficient to inhibit induction of the *Irfb1* reporter and specifically recognize the essential enhancer sequence of the *Irfb1* promoter *in vitro*. Binding of the IFN- $\beta$  enhancer sequence by proteins of other herpesviruses has been suggested to inhibit *Irfb1* induction by interfering with association of the host transcription factors (62–64). One of these proteins, K-bZIP of the Kaposi's sarcoma-associated herpesvirus (KSHV), was initially identified as

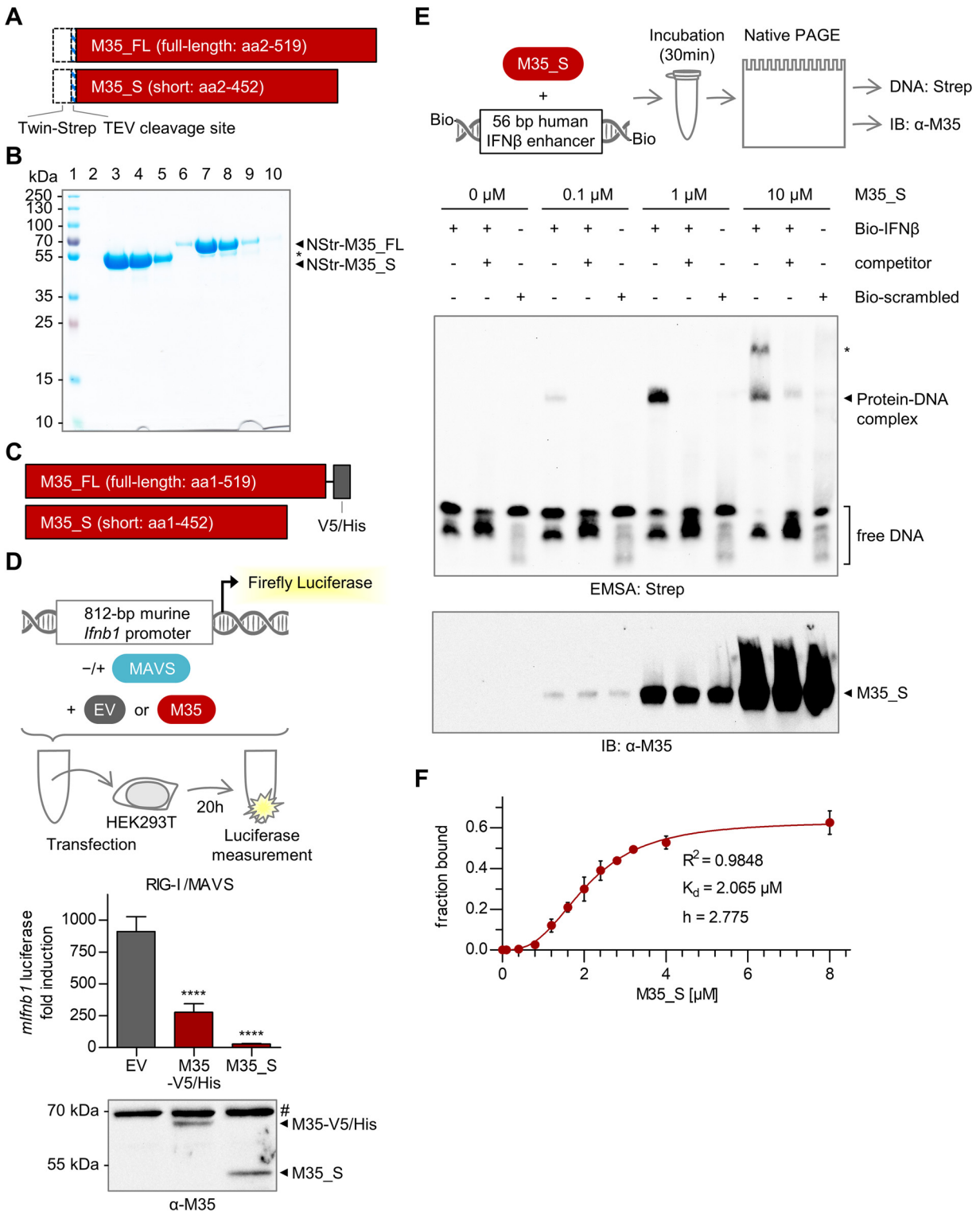


**FIG 1** M35 specifically binds to the interferon- $\beta$  (IFN- $\beta$ ) enhancer sequence *in vitro*. (A) Expression constructs for purification of full-length (M35\_FL) and short (M35\_S) M35. Dashed boxes indicate the N-terminal Twin-Strep tag and tobacco etch virus (TEV) protease cleavage sequence (NStr-). (B) Purification of NStr-M35\_S and NStr-M35\_FL proteins. NStr-M35\_S and NStr-M35\_FL proteins were purified from transiently transfected High-Five insect cells by StrepTactin affinity chromatography. Elution fractions were analyzed by SDS-PAGE and Coomassie staining. Lane 1, marker; lanes 2 to 5, eluate fractions 2 to 5 of NStr-M35\_S; lanes 6 to 10: eluate fractions 2 to 6 of NStr-M35\_FL. \*, degradation product of NStr-M35\_FL. (C) Constructs for transient expression of M35 with C-terminal V5/His tag (M35-V5/His) and of untagged M35\_S. (D) Analysis of M35-mediated inhibition of *Ifnb1* transcription in a luciferase reporter assay. HEK293T cells were cotransfected with the 812-bp murine *Ifnb1* luciferase reporter (*mIfnb1*-FLuc), a *Renilla* luciferase control (TK-RLuc), expression plasmids for Flag-tagged mitochondrial antiviral-signaling protein (Flag-MAVS) (stimulated conditions), or a respective empty vector (EV; unstimulated conditions), and the indicated

(Continued on next page)

stimulator of basal *Irfb1* promoter activity in the absence of PRR signaling but inhibited *Irfb1* promoter activity after induction of PRR signaling (62). Therefore, we tested whether M35 potentially activates the *Irfb1* reporter in the absence of PRR stimulation. Similar to stimulated conditions, however, M35 slightly inhibited (25%) *Irfb1* promoter activity also in unstimulated conditions (Fig. S1B).

**Structure determination reveals formation of M35 homodimers.** The purified M35\_S protein could be crystallized, and the three-dimensional structure was determined at 1.94 Å resolution (Fig. 2A; Table S2), using the homologous HHV6B U14 N-terminal domain (60) (PDB entry 5B1Q) as a search model for molecular replacement. Similar to U14, two M35\_S chains form an antiparallel homodimer with an extended interface along the long protein axis. Comparing the individual chains in the dimer to each other yielded a root-mean-square deviation (RMSD) of main-chain atoms of 0.438 Å. Most of the residues of M35\_S could be located in the electron density, with the exception of the most N-terminal residues 1 to 6, the most C-terminal residues 442 to 452, a fragment of 34 aa in M35 chain A from positions 344 to 376, and 31 aa in chain B from positions 346 to 375, respectively (Fig. 2A). The individual M35 moieties are comprised of 14  $\alpha$ -helices creating an elongated main body with two protuberant  $\beta$ -sheets forming a hairpin (Fig. 2A, middle). The  $\beta$ -hairpin of one monomer reaches out to the  $\beta$ -hairpin of the second M35 protomer of the M35 dimer (Fig. 2A, top), constituting a prominent part of the dimer interface. At the opposite site from the  $\beta$ -hairpins, a groove bends along the interface (Fig. 2A, bottom).

Analysis of the purified NStr-M35\_S protein by size-exclusion chromatography followed by multiangle light scattering (SEC-MALS) confirmed uniform particles of  $103.9 \pm 0.5$  kDa in solution (Fig. 2B). This is about twice the theoretical molecular weight of an NStr-M35\_S monomer (54.5 kDa), suggesting dimerization. Next, we studied the homodimerization of M35 in lysates of eukaryotic cells. Coexpression of M35-V5/His and C-terminally HAHA-tagged M35 (M35-HAHA) in HEK293T cells followed by immunoprecipitation for the V5 epitope showed that M35-HAHA readily coprecipitated with M35-V5/His (Fig. 2C), supporting a homotypic interaction. In contrast, M35-HAHA did not coprecipitate with a different nuclear V5/His-tagged protein of MCMV, M34 (65). Further, analysis of M35 in HEK293T lysates by native PAGE and immunoblot showed that M35 forms one defined species (Fig. 2D). An enhanced green fluorescent protein (eGFP)-IRF3 fusion protein was included as the control and, as expected, dimerized upon PRR signaling activation by overexpression of MAVS. Unlike eGFP-IRF3 dimers, the oligomerization status of M35 was independent of MAVS coexpression.

Taken together, we here present the crystal structure of the domain of M35 that harbors its immunomodulatory activity. M35 forms homodimers, and our results confirm that this is most likely the native state of M35 in cells and independent of PRR signaling.

**The overall protein fold is conserved between M35 of MCMV and U14 of HHV6B, two members of the pp85 protein superfamily of betaherpesviruses, but not their function.** Based on homology with the 85-kDa phospho-protein U14 of human herpesvirus 7 (HHV7), MCMV M35 is grouped in the pp85 protein superfamily that is conserved within the *Betaherpesvirinae*, but not the *Alpha-* or *Gammaherpesvirinae* (66–68). For closer inspection, we performed multiple and pairwise sequence alignments of the mem-

#### FIG 1 Legend (Continued)

expression plasmid for M35-V5/His or M35\_S or corresponding EV. Dual-luciferase measurement was performed after 20 h. Luciferase fold induction was calculated based on firefly luciferase values normalized to *Renilla* luciferase values from stimulated samples divided by corresponding values from unstimulated samples. The data are represented as means  $\pm$  SD combined from three independent experiments. Significance compared to EV was calculated by Student's *t* test (unpaired, two-tailed). \*\*\*\*,  $P < 0.0001$ . The lysates were analyzed by immunoblotting (IB) with an M35-specific antibody. #, unspecific signal. (E) Analysis of M35-DNA binding by electrophoretic mobility shift assay (EMSA). Increasing amounts of M35\_S protein were mixed with a 5'-biotinylated double-stranded 56-bp oligonucleotide probe containing the sequence of the human IFN- $\beta$  enhancer (Bio-IFN $\beta$ ) or a random sequence (Bio-scrambled) for control, respectively. The samples were subjected to native PAGE followed by blotting and detection of the biotinylated probes with a streptavidin-peroxidase conjugate (Strep). Unlabeled competitor (IFN- $\beta$  enhancer sequence) was added in 100 $\times$  excess. A second EMSA gel was immunoblotted and analyzed with an M35-specific antibody. \*, second protein-DNA complex. One representative of three independent experiments is shown. (F) Determination of the binding affinity of M35\_S by EMSA. EMSA was performed as described in panel E with a titration series of 0.1 to 8  $\mu$ M M35\_S protein incubated with the murine IFN- $\beta$  enhancer probe. The band intensities of bound and free probe per lane were quantified using Fiji to calculate the bound probe fraction. The values are plotted as means  $\pm$  SD of three independent experiments. The curve was fitted in GraphPad Prism using the binding-saturation module for specific binding with Hill slope (*h*) to determine the dissociation constant ( $K_d$ ). RIG-I, retinoic acid-inducible gene I.

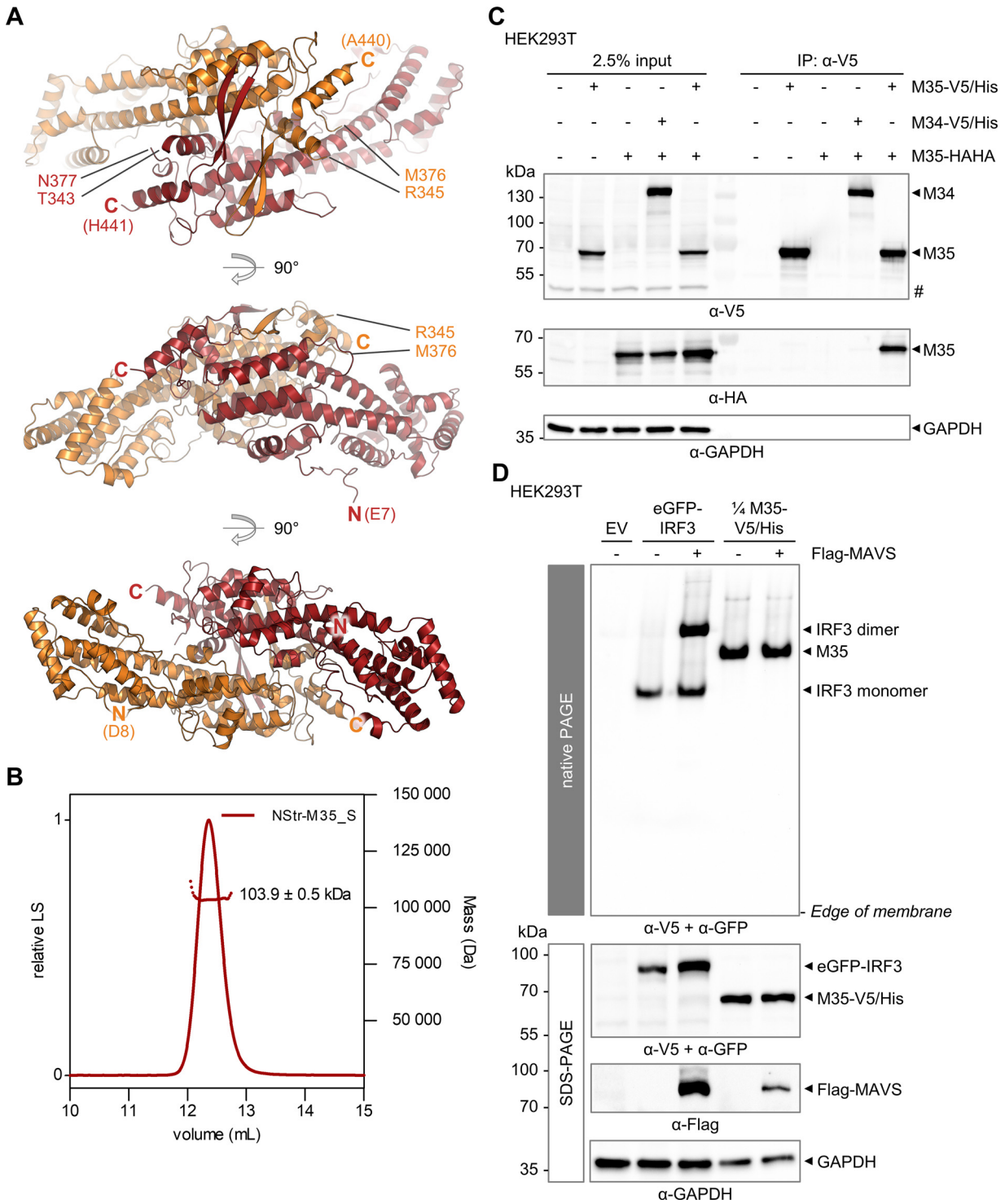


**FIG 2** The M35 protein forms homodimers after crystallization and in cell lysates. (A) Ribbon representations of the M35 protein crystal structure. M35<sub>S</sub> (amino acids [aa] 2 to 452) was crystallized, and its structure was solved at 1.94 Å. M35 monomers are depicted in red (aa 7 to 343 and aa 377 to 441) or orange (aa 8 to 345 and aa 376 to 440), respectively. The visible N and C termini (bold) and the ends of each protein chain are labeled accordingly. The structure is depicted from three perspectives. (B) Size-exclusion chromatography followed by multiangle light scattering (SEC-MALS) of purified NStr-M35<sub>S</sub> protein. (C) Coimmunoprecipitation of M35 in cell lysates. HEK293T were cotransfected with indicated expression plasmids for M35-V5/His and M35-HAHA, M34-V5/His and M35-HAHA (negative control), or single constructs filled up with EV. An anti-V5 immunoprecipitation (IP) was performed 24 h later. The input and IP samples were analyzed by SDS-PAGE and immunoblotting with HA- and V5-specific antibodies. Detection of GAPDH served as the loading control. #, unspecific band. One representative of two independent experiments is shown. (D) Native PAGE of M35 in cell lysates. HEK293T cells were cotransfected with expression plasmids for eGFP-IRF3 (control) or M35-V5/His or the corresponding EV and for Flag-MAVS (stimulated conditions) or the respective EV (unstimulated conditions). The cells were lysed 20 h later (Continued on next page)

bers of the pp85 superfamily (Table S3; File S1). The resulting phylogenetic tree precisely mirrors the division of the betaherpesviruses into different genera, and pairwise sequence comparisons of all proteins to MCMV M35 yielded amino acid identities from up to 50% for the most closely related *Muromegalovirus* homologs to about 20% for the U14 proteins from the genus *Roseolovirus* (Fig. 3A). Aside from M35, only the crystal structure of U14 of HHV6B has been reported so far from the pp85 protein superfamily (60). Superposition of the dimer structures of M35 and U14 clearly reflects their structural similarity (Fig. 3B), despite below 25% shared sequence identity in both global and local alignments (Fig. 3A). While the overall  $\alpha$ -helical fold with the protruding  $\beta$ -hairpin is similar, the RMSD of main-chain  $C_{\alpha}$  atoms of 2.51 Å yielded for the superposition of dimers (717 of 805 resolved residues of the M35 dimer aligned to the residues of the U14 dimer) indicates considerable differences between the two structures.

Little is known to date about the functions of the *Roseolovirus* U14 proteins, and to our knowledge, no U14-mediated inhibition of the type I IFN response has been reported. We generated expression constructs of the HHV6A, HHV6B, and HHV7 U14 open reading frames (ORFs), adding an N-terminal triple V5 epitope tag (3×V5-) for detection (Fig. 3C), and assessed their effects in the *Irfb1* luciferase reporter assay. To test whether these M35 homologs also target the human IFN- $\beta$  enhancer, we cotransfected a reporter containing the human *Irfb1* promoter sequence, again adding the MAVS expression plasmid for stimulation (Fig. 3C). Similar to M35-V5/His, coexpression of analogously designed 3×V5-M35 efficiently inhibited *Irfb1* promoter activation (Fig. 3D), and so did coexpression of the C-terminal tagged HCMV homolog of M35 and U14, UL35-HAHA, consistent with our previous work (57). Of the three U14 proteins, only HHV7 U14 downmodulated induction of the human *Irfb1* promoter ( $P < 0.01$ ), although to a much lower extent than M35. Notably, immunoblots suggested overall lower protein levels of the 3×V5-U14 proteins relative to 3×V5-M35. Still, 3×V5-U14 proteins could be detected after transfection of 100 ng of the respective plasmid, in contrast to M35-V5/His after transfection of only 1 ng of plasmid, which sufficed for significant ( $P < 0.0001$ ) inhibition. To rule out that the epitope tag interfered with the putative function of U14 proteins, additional expression constructs were generated to study U14, UL35, and M35 without any modification (Fig. 3E). Similar results were obtained with the untagged proteins (Fig. 3F). All in all, these data support the notion that at least some features are conserved within the pp85 protein superfamily, but certainly additional studies will be required to shed light on the potential role of the HHV6 and HHV7 U14 proteins during the innate immune response.

**Identification of loss-of-function mutants of M35 by reverse genetics.** The crystallographic structure of M35\_S provided a basis to dissect the contribution of individual structural features to the immunomodulatory activity of the M35 protein. In particular, identification of residues essential for M35's activity might allow connection of the molecular function with a structural feature, such as a putative DNA-binding site. Aiming to disrupt the function of M35, we focused mutagenesis on prominent surface features and used the MAVS-stimulated *Irfb1* reporter assay to screen for loss-of-function derivatives. The WT M35-V5/His protein served as the basis to generate mutants and was included as the control.

First, we deleted the  $\beta$ -hairpins (aa 406 to 424;  $\Delta\beta$ ) or replaced them with a single proline ( $\Delta\beta$ +P) or glycine ( $\Delta\beta$ +G) residue to bridge the distance to the continuing protein chain (Fig. 4A). All three  $\Delta\beta$  derivatives lost the ability to inhibit induction of the *Irfb1* luciferase reporter, indicating that the  $\beta$ -hairpins are an important feature of the M35 protein. Compared to WT M35-V5/His, the mutants yielded slightly reduced protein levels in control immunoblots but were still readily detectable (Fig. 4A).

## FIG 2 Legend (Continued)

and analyzed in parallel by native (upper panel) or SDS-PAGE (lower panel) followed by immunoblotting and detection with GFP-, V5-, Flag-, and GAPDH-specific antibodies as indicated. Lysates of M35-V5/His-expressing cells were diluted 1:4 in lysis buffer to adjust the signal strength in the native immunoblot. One representative of three independent experiments is shown. GAPDH, glyceraldehyde-3-phosphate dehydrogenase; GFP, green fluorescent protein; HA, haemagglutinin tag; IRF3, interferon regulatory factor 3; LS, light scattering.



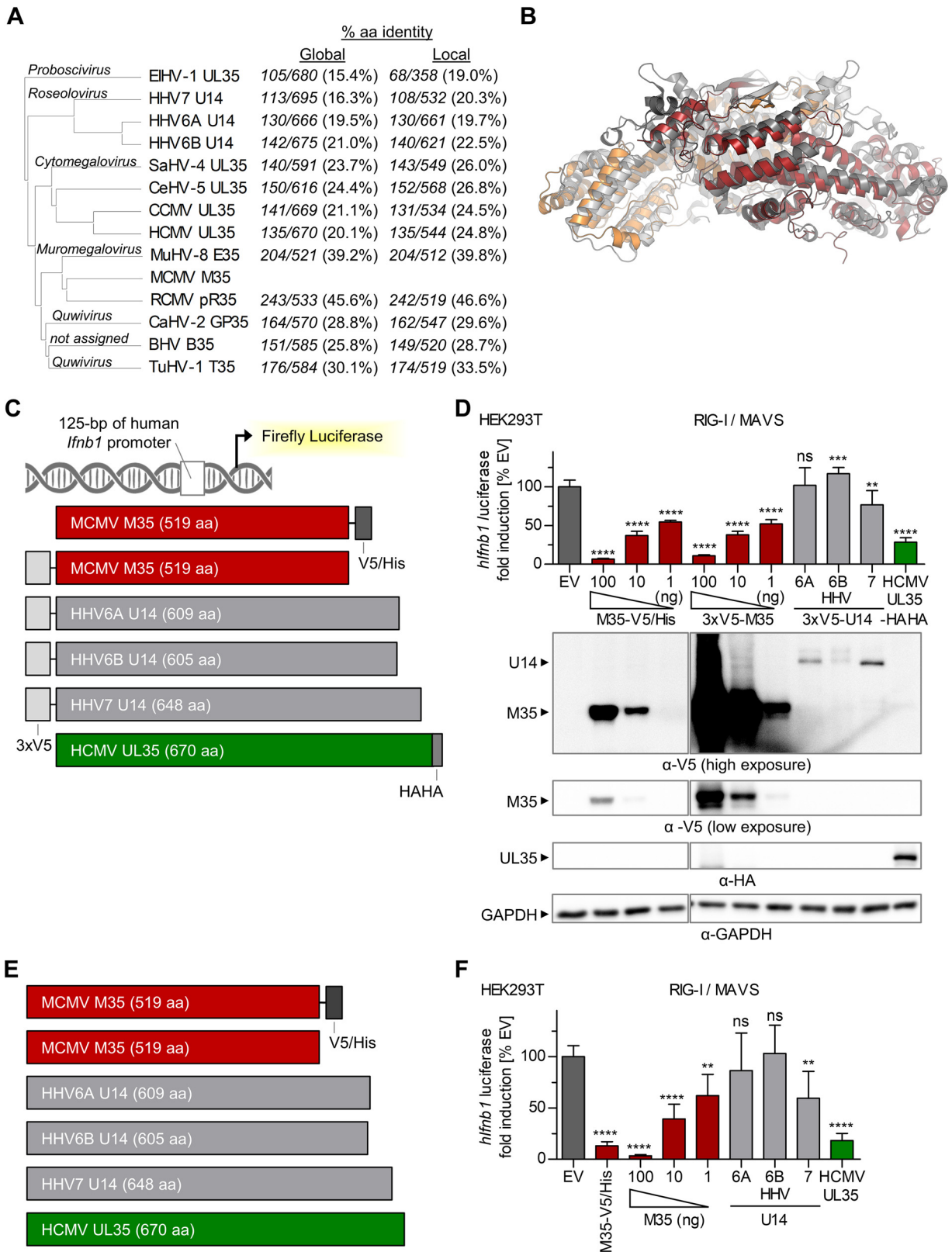


**FIG 3** Comparison of murine cytomegalovirus (MCMV) M35 with the homologous U14 proteins of HHV6A, HHV6B, and HHV7 of the *Betaherpesvirinae* pp85 protein superfamily regarding a potential inhibition of *Ifnb1* promoter induction. (A) Phylogenetic tree of the pp85 protein superfamily of the *Betaherpesvirinae*. Included are homologous proteins from all betaherpesviruses infecting humans and at least one species per genus. The table indicates the percentage of identical amino acids (% aa), as well as aligned and total sequence lengths for all proteins compared to M35 after alignment of sequences from end to end (global) or of the most similar regions (local). (B) Superposition of (Continued on next page)

Second, we assessed the electron surface potential of the dimer and identified a positive surface patch at the side of each M35 monomer formed by eight arginine residues (R10, R20, R99, R102, R217, R257, R260, and R310; Fig. 4B). Since this could provide a site for DNA interaction, we exchanged these residues in different combinations for alanine residues. However, even the exchange of all residues did not impair the inhibitory effect by these M35 derivatives, suggesting that this feature is not critical for the assayed activity.

Third, we inspected the groove that runs along the dimer interface. Due to its bend and asymmetric elevations of the walls at the interface creating deep and shallow stretches, we approximated the size of the groove with a width of about 20 Å from wall to wall (Fig. S2A) and roughly 83 Å from one end to the other (Fig. S2B). These dimensions could accommodate a B-DNA double helix at a length of approximately 21 bp (69), indicating this as a candidate site for DNA binding. We exchanged neighboring positions with surface-exposed hydrophilic residues along the groove for alanine residues, generating four mutants (N42A/R69A, K71A/H72A/R73A, H174A/R177A/D180A, and K438A/R439A; Fig. 4C). The double mutation N42A/R69A abrogated the inhibitory effect of M35, and again, the loss-of-function derivative yielded reduced protein levels compared to WT M35 (Fig. 4C). Individual exchange of the two positions showed that the mutation R69A alone was sufficient to disrupt M35's activity (Fig. 4D). A titration of WT M35-V5/His was included to demonstrate that cotransfection of a hundredth of the standard amount (100 ng) of expression construct for M35-V5/His WT protein sufficed for significant ( $P < 0.001$ ) downmodulation of *Irfb1* promoter induction despite undetectable protein levels in the immunoblot (Fig. 4D). In contrast, M35-V5/His R69A was detectable but did not notably influence luciferase induction, indicating that the reduced protein level was not the sole or the main reason for the loss of function of M35 R69A.

Fourth, we characterized the part of M35 that was not resolved in the crystal structure (M35 aa positions 344 to 376 of chain A and positions 346 to 375 of chain B). In the structure of HHV6B U14 (60), the first part of the corresponding segment constitutes the end of an  $\alpha$ -helix ( $\alpha$ 13) and then forms a loop containing small helix elements ( $\alpha$ 14,  $3_{10}$ -helices  $\eta$ 2 to  $\eta$ 5) that reaches back to the bulk structure close to where it reached out (Fig. 4E; Fig. S2C). Based on the superposition of M35 and U14 (Fig. S2C) and the alignment of the pp85 superfamily (Fig. 4E), we replaced the unresolved residues T343 to R375 of M35 with (i) GSG or (ii) GPG linkers (creating  $\Delta$ T343-R375+GSG, short: GSG, or  $\Delta$ T343-R375+GPG, short: GPG, respectively), or substituted only the segment L349 to K373 starting after the potentially continuing  $\alpha$ 13 helix with a (iii) GSGS linker (creating  $\Delta$ L349-K373+GSGS, short: GSGS). However, despite about 30 amino acids lacking from M35, all derivatives still inhibited induction of the *Irfb1* reporter, indicating that the loop is not critical for the immunomodulatory activity of M35 (Fig. 4E).

In sum, reverse genetic characterization of M35 led to the identification of the  $\beta$ -hairpins at one side of the structure and the surface-exposed R69 at the opposite site as critical parts for the inhibitory function. Interestingly, similar to the  $\beta$ -hairpins, R69 is also located directly at the dimer interface and faces the residue R69 of the second M35 moiety in the homodimer (Fig. S2D). Closer inspection of the electron density revealed that each R69 residue adopts two conformations with similar occupancy, potentially allowing for  $\pi$ -stacking with the opposite R69 residue or for interaction with D44 of the opposite M35 chain, respectively. In this way, interaction of the M35 chains via R69 might contribute to the homodimerization.

### FIG 3 Legend (Continued)

the dimers of MCMV M35 (orange-red) with the homologous HHV6B U14 (gray shades; PDB entry 5B1Q) (60). (C, E) Schemes of the firefly luciferase reporter construct controlled by the 125-bp human *Irfb1* promoter (*Irfb1*-FLuc) and of expression constructs for M35 of MCMV; U14 of HHV6A, HHV6B, or HHV7; and UL35 of human cytomegalovirus (HCMV) with (C) or without (E) tags. (D, F) Analysis of HHV6A, HHV6B, and HHV7 U14 proteins for inhibition of *Irfb1* transcription in the luciferase reporter assay. Luciferase reporter assays were performed as described for Fig. 1D by transfection of HEK293T cells with a Flag-MAVS-expressing plasmid for stimulation, *Irfb1*-FLuc, and indicated expression plasmids for M35, UL35, and U14 proteins with N- or C-terminal tags (D) or without tags (F). Expression constructs for M35-V5/His and 3 $\times$ V5-M35 (D) or untagged M35 (F) were applied in a titration series (100, 10, or 1 ng), filled up with EV to 100 ng; 100 ng was applied for U14 constructs. The data were normalized to EV samples and are represented as means  $\pm$  SD combined from three independent experiments. Significance compared to EV was calculated by Student's *t* test (unpaired, two-tailed). ns, not significant; \*\*,  $P < 0.01$ ; \*\*\*,  $P < 0.001$ ; \*\*\*\*,  $P < 0.0001$ . (D) The lysates were analyzed by immunoblotting using V5- and HA-specific antibodies. Detection of GAPDH served as the loading control. HHV, human herpesvirus.

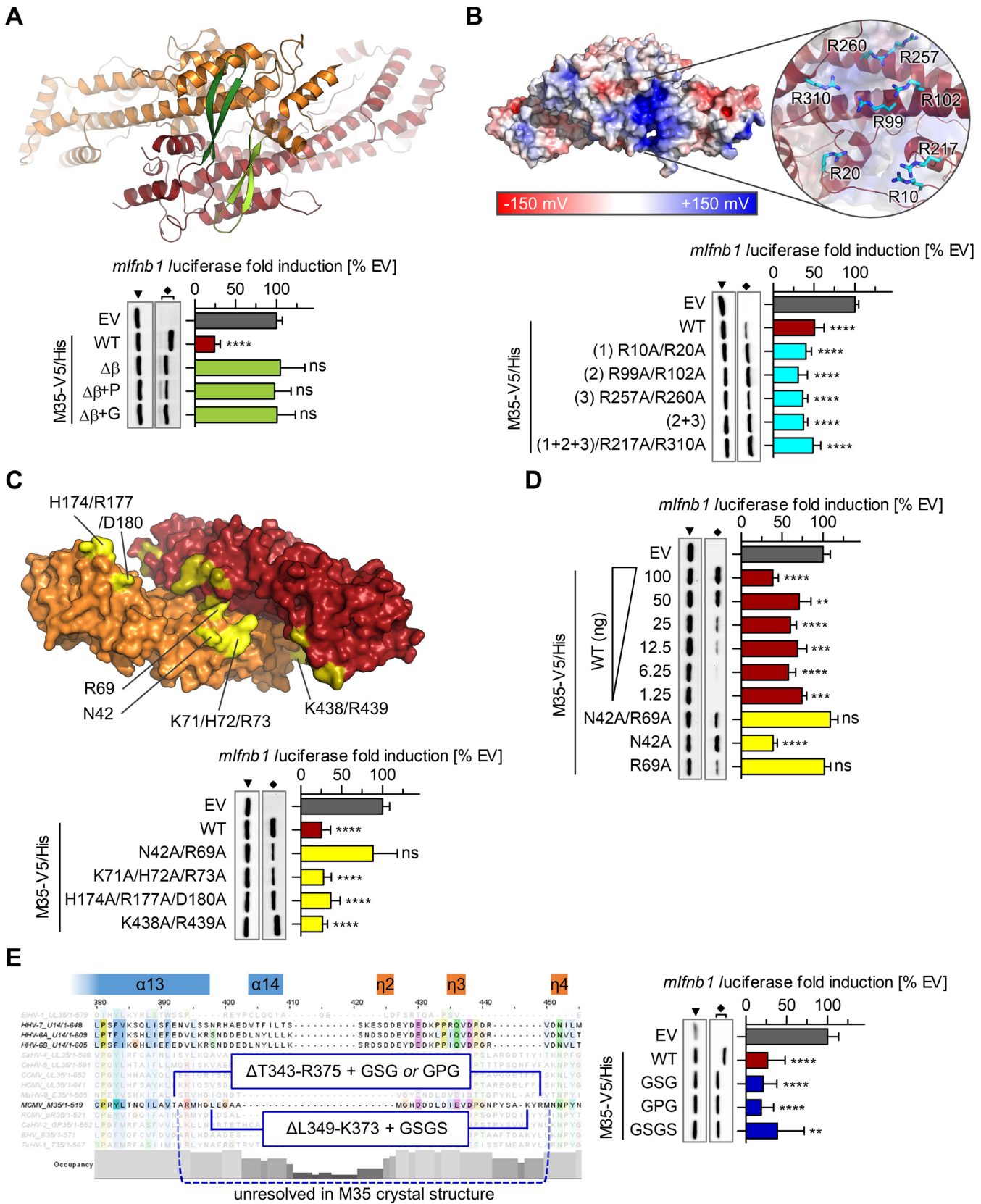


**FIG 4** Identification of loss-of-function mutants of M35 by reverse genetics. Prominent surface features of the M35 structure and screening for of M35 mutants for a loss of inhibition of *lfnb1* transcription in a luciferase reporter assay. (A) Top view of the M35 dimer as ribbon representation, with the two protruding  $\beta$ -hairpins (aa 406 to 424, green shades). The  $\beta$ -hairpins were deleted entirely ( $\Delta\beta$ ) or substituted by a single proline ( $\Delta\beta$ +P) or glycine (Continued on next page)

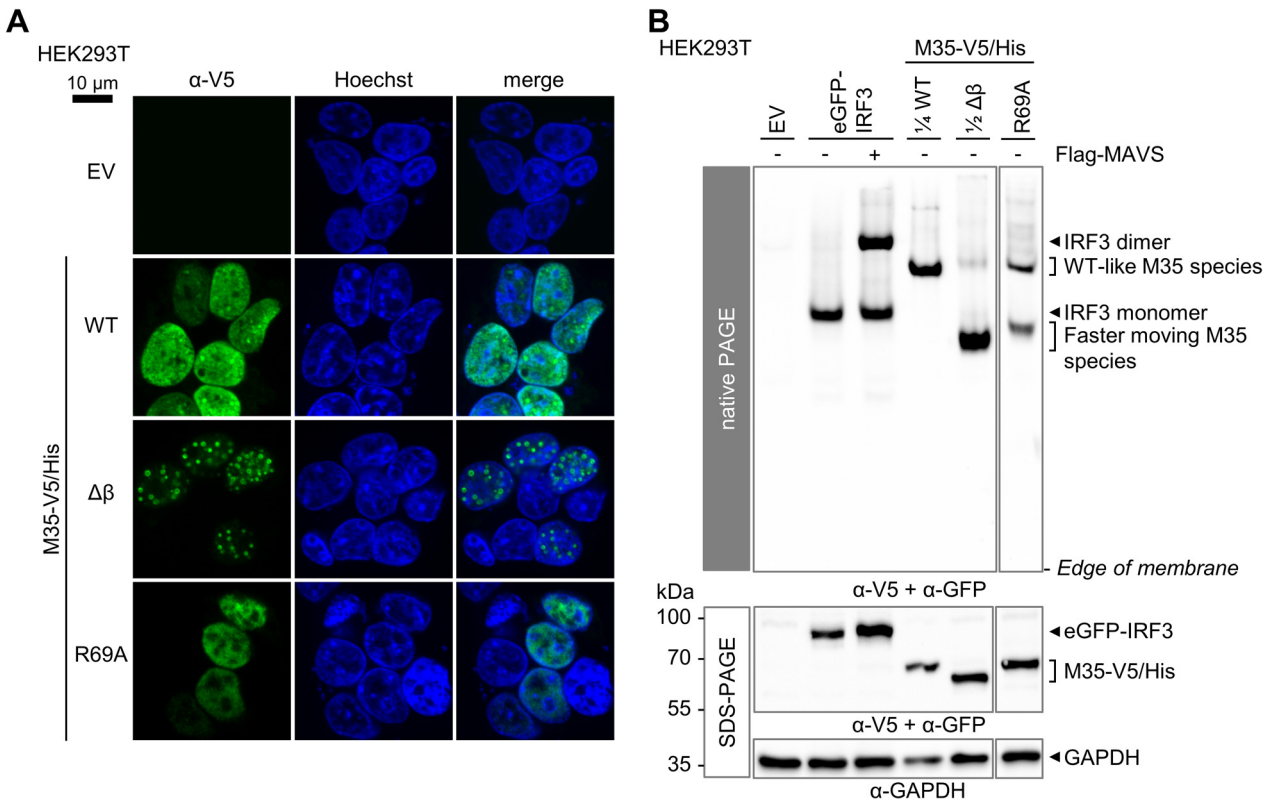


**FIG 5** Identified M35 loss-of-function mutations impair the homodimerization of M35. (A) Immunofluorescence assay of M35 derivatives. HEK293T cells transfected with expression constructs for M35-V5/His WT,  $\Delta\beta$ , or R69A or the corresponding EV were subjected to immunofluorescence labeling with a V5-specific antibody. The nuclei were stained with Hoechst. Bar, 10  $\mu\text{m}$ . The images are representative of at least two independent experiments. (B) Native PAGE of M35 derivatives. Native (upper panel) and SDS-PAGE (lower panel) followed by immunoblotting were performed as described before (Fig. 2D) by cotransfecting HEK293T cells with expression plasmids for eGFP-IRF3, or M35-V5/His WT,  $\Delta\beta$ , or R69A or the respective EV, and for Flag-MAVS (stimulated conditions) or the respective EV (unstimulated conditions), and analysis with GFP-, V5-, Flag-, and GAPDH-specific antibodies. Lysates containing M35-WT and M35- $\Delta\beta$  were diluted as indicated in lysis buffer to adjust the signal strength in the native immunoblot. One representative of three independent experiments is shown.

**Loss-of-function mutants suggest that dimerization is a critical feature of the M35 protein.** As we generated loss-of-function mutants aiming to identify a position that specifically and directly contributes to M35's immunomodulatory function, we further characterized M35  $\Delta\beta$  and M35 R69A. After immunolabeling of transfected HEK293T cells, both M35-V5/His  $\Delta\beta$  and M35-V5/His R69A displayed a nuclear localization (Fig. 5A). Similar to WT M35 (54), the R69A mutant was dispersed throughout the nucleus, while the  $\Delta\beta$  mutation led to the formation of distinct speckles. The overall signal for R69A was weaker compared to WT M35, corresponding to the protein levels detected by immunoblot (Fig. 4D). Further, analysis of the M35 derivatives by native PAGE and immunoblot revealed that the two loss-of-function mutants of M35 were markedly different from the WT protein; only a small fraction of the M35-V5/His  $\Delta\beta$  protein displayed the same running distance as WT

#### FIG 4 Legend (Continued)

( $\Delta\beta$ +G). (B) Side view of the M35 dimer, with depiction of the electrostatic surface potential. Red, negative; blue, positive. (Inset) Closeup of the underlying cluster of arginine residues (cyan sticks). The indicated arginines were mutated to alanine in pairs [10 and 20 (1); 99 and 102 (2); 257 and 260 (3)], or as combinations of R99A, R102A, R257A, and R260A (2 + 3) or of (1) and (2 + 3) (1 + 2 + 3) with R217A and R310A. (C) Bottom view of the M35 dimer as surface representation, showing the groove formed along the dimer interface. Clusters of surface-exposed residues (yellow shades) were mutated to alanine, creating N42A/R69A, K17A/H72A/R73A, H174A/R177A/D180A, and K438A/R439A (indicated on one M35 monomer). (D) The positions of the double mutant N42A/R69A were analyzed individually (N42A and R69A, respectively) alongside a titration series of the wild-type (WT) M35 protein, filled up with EV to 100 ng. (E) Annotated structural elements of HHV6B U14 ( $\alpha$  and  $\eta$  helices) (60) and the alignment of the pp85 protein superfamily served as basis to design mutants (navy) of the unresolved loop of M35, replacing the whole unresolved region (T343 to R375) with a GSG or GPG linker (yielding the mutants  $\Delta\text{T343-R375}+\text{GSG}$ , short: GSG, and  $\Delta\text{T343-R375}+\text{GPG}$ , short: GPG, respectively), or L349 to K373 with a GSGS linker (yielding the mutant  $\Delta\text{L349-K373}+\text{GSGS}$ , short: GSGS). (A to E) Luciferase reporter assays were performed as described for Fig. 1D by transfection of HEK293T cells with a Flag-MAVS-expressing plasmid for stimulation, *mlnb1*-FLuc, and indicated expression plasmids. The data were normalized to EV samples and are represented as means  $\pm$  SD combined from three independent experiments. Significance compared to EV was calculated by Student's *t* test (unpaired, two-tailed). ns, not significant; \*\*,  $P < 0.01$ ; \*\*\*,  $P < 0.001$ ; \*\*\*\*,  $P < 0.0001$ . The lysates were analyzed by immunoblotting with V5- and GAPDH-specific antibodies. Filled arrowheads, GAPDH; diamonds, M35-V5/His derivatives.

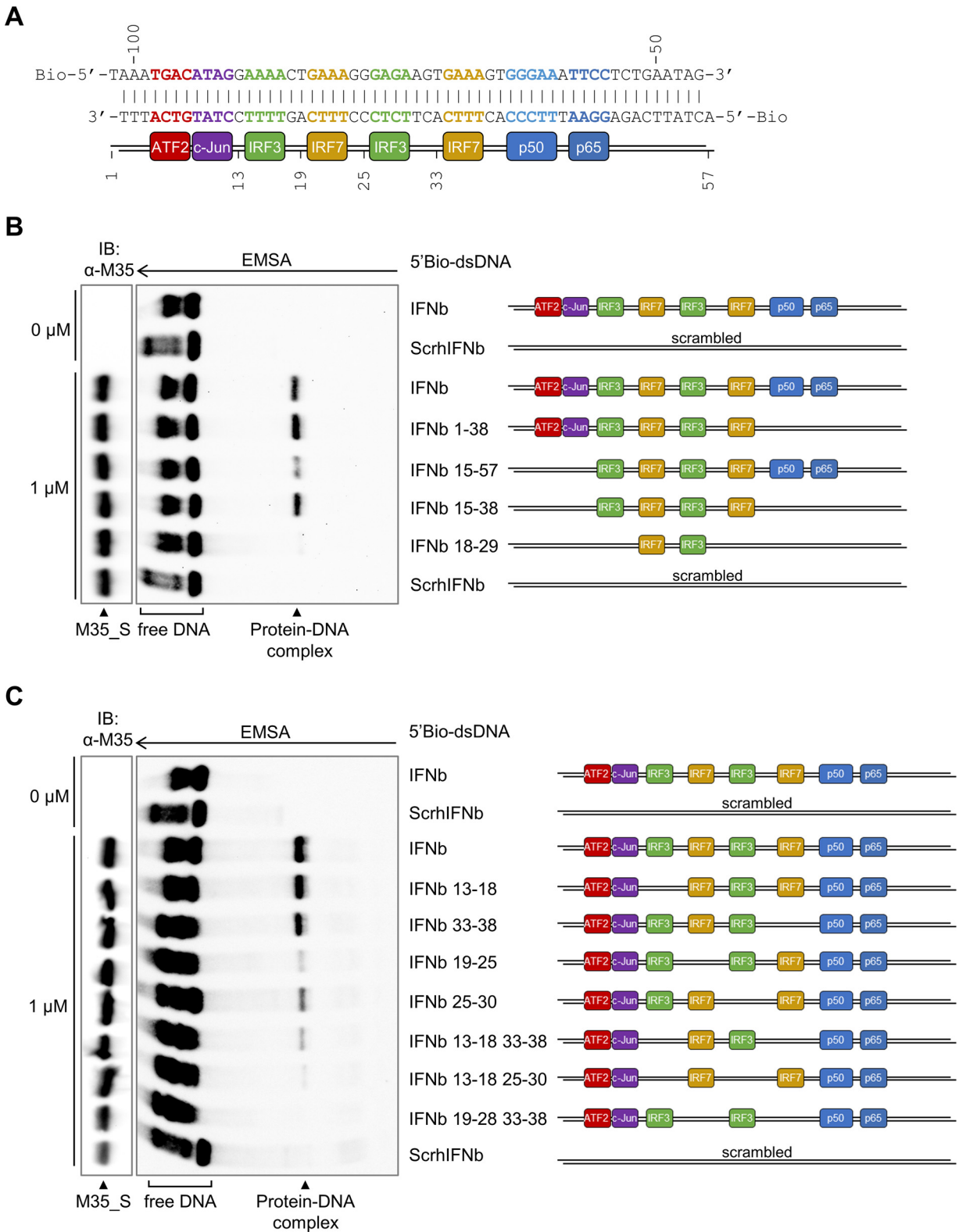


**FIG 6** The consecutive core motifs of the IRF-recognition elements in the IFN- $\beta$  enhancer are required for M35-DNA binding. (A) DNA sequence of the human IFN- $\beta$  enhancer upstream of the *Irf1* gene with positions relative to the transcription start site in bp indicated above the sequence. Both strands were 5'-biotinylated for detection of EMSA probes. Core sequence elements interacting with individual DNA-binding domains are highlighted in the same colors as the respectively bound dimeric transcription factors ATF2/c-Jun (red-purple), IRF3 or IRF7 dimers (domains of one dimer are indicated in green or yellow, respectively), and p50/p65 (nuclear factor  $\kappa$ B [NF- $\kappa$ B], blue) (based on reference 34). The positions within the probe are indicated below. (B, C) EMSAs for M35 binding to specific sections of the IFN- $\beta$  enhancer. EMSAs were

(Continued on next page)

M35-V5/His, and the major share moved faster through the gel, creating an additional band. M35-V5/His R69A gave also rise to the faster migrating protein species, with comparable amounts for this and the WT-like species (Fig. 5B). Based on our description of the WT M35 protein as a dimer (Fig. 2) and the distinct shift between the WT-like and the faster moving species, we propose that the latter represents M35 monomers. This observation indicates that mutations  $\Delta\beta$  and R69A severely impaired homodimerization of M35.

Thus, we conclude that M35  $\Delta\beta$  and M35 R69A lost their ability to inhibit the *Irfb1* promoter due to the impact on their overall integrity and were therefore not included in further analyses. Although we did not directly determine the DNA-binding site, this finding highlights the importance of homodimerization for M35's activity.

**M35-DNA recognition requires successive core motifs of IRF-recognition elements.** To study the protein-DNA interaction further, we next dissected the sequence requirements for M35-DNA binding by EMSA. Using the human IFN- $\beta$  enhancer as a blueprint (Fig. 6A), we replaced specific binding elements while keeping the probe length constant. Note that although the scheme in Fig. 6A indicates alternating occupation of IREs by IRF3 and IRF7 according to the report by Panne and colleagues (34), due to the lack of steady-state IRF7 expression, all IREs will initially be occupied by IRF3 upon primary infection of nonimmune cells.

First, we studied contribution of the different transcription factor-binding motifs by scrambling the recognition elements individually or in combination (Fig. 6B). Lack of the NF- $\kappa$ B (IFNb 1 to 38) or both ATF2/c-Jun and NF- $\kappa$ B-binding motifs (IFNb 15 to 38) still allowed for formation of the M35-DNA complex, although less signal of a protein-DNA complex was observed for the probe lacking only the ATF2/c-Jun motif (IFNb 15 to 57). Overall, this narrowed down the M35-bound sequence to the central repeat of IREs, and congruently, the signal of DNA-protein complex was drastically reduced when only two of the four core IRE motifs were intact (IFNb 18–29). We additionally sought to narrow down whether individual IREs enable M35-DNA recognition with probes in which different combinations of the core 5'-GAAA-3' motifs were scrambled. Analysis of M35-DNA binding with the yielded array of probes revealed that the signal of the protein-DNA complex gradually decreased with fewer immediately successive core IRE motifs (Fig. 6C). This suggests that instead of contacting a short sequence, the M35-binding site broadly overlaps with the binding site of IRF3/7 dimers.

These results show that the M35-binding sequence coincides with the recognition elements for IRF3/7 binding, whereas motifs for NF- $\kappa$ B or ATF2/c-Jun binding were not essential. This finding was in contrast to our previous report, which suggested that M35 targeted NF- $\kappa$ B-mediated transcription (54). We therefore tested whether M35 inhibits *Irfb1* promoter induction when activation was directly dependent on either IRF3 or NF- $\kappa$ B. In agreement with the EMSA data, coexpression of M35-V5/His, but not of the IFNAR-signaling antagonist M27, significantly ( $P < 0.0001$ ) reduced *Irfb1* luciferase reporter activity induced by transient expression of constitutively active IRF3-5D (Fig. S3A). In contrast, induction of the *Irfb1* luciferase reporter by transient expression of the intrinsically active NF- $\kappa$ B subunit p65 was not impaired by M35-V5/His (Fig. S3B). This supports the results here, which indicate that the immunomodulatory activity of M35 is independent of NF- $\kappa$ B or its binding motifs.

**The presence of M35 impairs binding of IRF3 to the host's IFN- $\beta$  enhancer upon stimulation of PRR signaling.** Since M35-DNA binding requires IREs, we next asked whether M35 would impair recruitment of IRF3 to the IFN- $\beta$  enhancer. To address this, we used immortalized mouse embryonic fibroblasts (iMEFs) that stably express the previously characterized M35-myc/His (54) to perform chromatin immunoprecipitation (ChIP) with an IRF3-specific antibody (Fig. 7A). Immunoblotting of chromatin fractions vali-

#### FIG 6 Legend (Continued)

performed as described for Fig. 1E with 1  $\mu$ M purified M35\_S and indicated 5'-biotinylated 56 bp dsDNA probes based on the sequence of the human IFN- $\beta$  enhancer. A probe with a random sequence (scrambled: ScrhIFNb) served as negative control. (B) The sequence sections marked in the probe label were retained, and the remaining flanking sections were replaced for random sequences. (C) The 6-bp sequence sections marked in the probe label were replaced for random sequences to mutate individual parts of the IRF-recognition elements. The arrow marks the running direction of the EMSA gel. One representative of three independent experiments is shown.

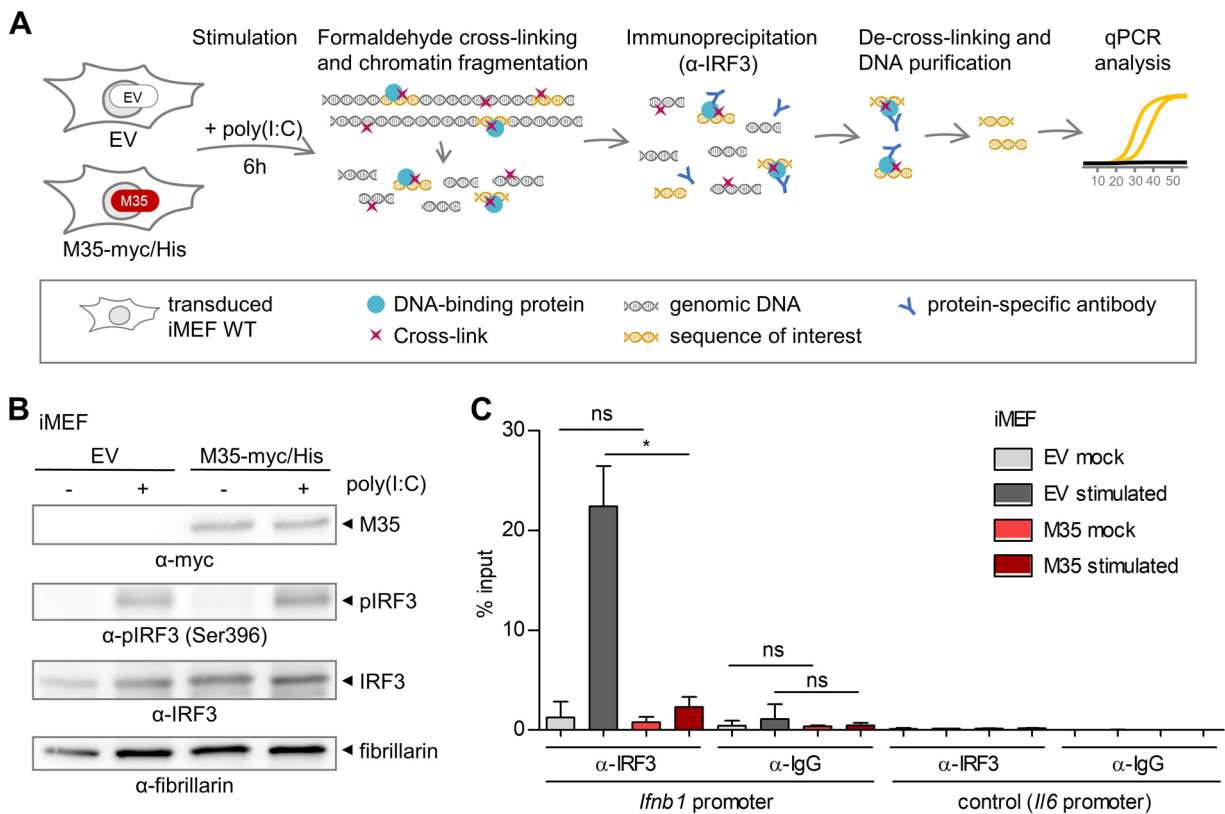


**FIG 7** Presence of M35 impairs binding of IRF3 to the host's IFN- $\beta$  enhancer upon stimulation of pattern-recognition receptor (PRR) signaling. (A) Chromatin immunoprecipitation (ChIP) assay. Immortalized mouse embryonic fibroblasts (iMEFs) stably expressing M35-myc/His or the corresponding EV were stimulated by transfection of poly(I:C) or mock-treated. After 6 h, formaldehyde (FA) was applied to cross-link interactions, and the cells were harvested. Chromatin was isolated, fragmented for processing, and subjected to immunoprecipitation with an IRF3-specific antibody. The precipitated material was de-cross-linked, and DNA was purified and analyzed by quantitative PCR (qPCR) alongside 1% of input material. (B) Immunoblot of chromatin samples from iMEFs. iMEFs were processed as described for panel A and analyzed by immunoblotting with myc-, pIRF3-, IRF3-, and fibrillarin-specific antibodies. Fibrillarin served as a loading control for the nuclear fraction. Shown is one representative of three independent experiments. (C) ChIP for recruitment of IRF3 to the *Irfb1* promoter in presence or absence of M35. ChIP was performed as described for panel A with an IRF3-specific and an IgG control antibody, and the samples were analyzed for enrichment of the IFN- $\beta$  enhancer sequence by qPCR. A primer set targeting the promoter of *Il6* upstream of a predicted IRF3-binding site was used as negative control. Shown are combined data from two independent experiments. Significance was calculated by Student's *t* test (unpaired, two-tailed), comparing mock- or stimulus-treated M35-myc/His to respective EV iMEFs. ns, not significant; \*,  $P < 0.05$ .

dated expression of M35-myc/His and phosphorylation of IRF3 after transfection with the dsRNA mimetic poly(I:C) (Fig. 7B). Enrichment of the *Irfb1* promoter sequences bound by IRF3 was greatly increased in control cells upon PRR stimulation compared to mock treatment (Fig. 7C). Strikingly, stimulation-induced enrichment of IRF3 at this promoter was significantly decreased in iMEFs stably expressing M35-myc/His ( $P < 0.01$ ). This suggests that the presence of M35 in host cells impairs the binding of endogenous IRF3 to its target sequence in the *Irfb1* promoter upon PRR signaling.

Taken together, our data indicate that the viral protein M35 localizes to the nucleus, where it binds to specific host DNA sequences by recognition of motifs in IRF3/7-binding sites. As the presence of M35 does not influence activation or total or stimulus-induced nuclear levels of the transcription factors NF- $\kappa$ B or IRF3 (54), we conclude that binding of M35 to the IFN- $\beta$  enhancer competitively impairs binding of IRF3 to the same site and thus antagonizes induction of *Irfb1* transcription.

**Dissection of the contribution of IRF3-mediated versus type I IFN signaling-mediated induction of antiviral genes in murine fibroblasts.** While type I IFNs represent a major target of IRF3-mediated gene regulation, several reports have demonstrated that during viral infection, IRF3 also regulates expression of a subset of ISGs (9, 19–21). During HCMV infection of fibroblasts, some IRF3-dependent ISGs are upregulated to a similar extent by IRF3 or type I IFN-IFNAR signaling, and others are fully

induced only when both pathways are activated (21). Since the M35 recognition site overlapped with IREs and M35's presence impaired binding of IRF3 to the *Irfb1* promoter after PRR stimulation, we wondered whether other IRF3-regulated transcripts are influenced by M35.

The direct induction of specific ISGs by IRF3 was reported by several groups studying human cells (17, 70) but is to our knowledge less well characterized in murine cells. Aiming to obtain a full picture of M35's effect on mRNA transcription in the host cell, we applied RNA sequencing of metabolically labeled transcripts (SLAM-seq) (71, 72). In this method, the nucleotide analog 4-thiouridine (4sU) is incorporated into nascent RNA for a defined time, and after sequencing, this enables quantification of transcripts synthesized in this time window. For direct comparison of transcripts affected by M35 with those regulated by IRF3 or type I IFN-IFNAR signaling, we first used SLAM-seq to characterize the IRF3-dependent versus type I IFN signaling-responsive genes in murine embryonic fibroblasts (MEFs). Comparison of the responses in primary WT MEFs with IRF3<sup>-/-</sup> or IFNAR1<sup>-/-</sup> MEFs allowed us to differentiate gene regulation dependent on the activation of IRF3 downstream of PRR activation versus in response to type I IFN signaling downstream of IFNAR1/IFNAR2 activation (Fig. 8A). DNA sensing has previously been reported as the most biologically relevant pathway in immune control of initial CMV infection (73). Accordingly, MEFs were stimulated for 4 h by transfection of immunostimulatory DNA (ISD) to detect IRF3-mediated regulation (*Irfb1*) before production of type I IFNs would upregulate ISG expression, or for 3 h by treatment with murine IFN- $\beta$  to detect the peak of the first transcriptional response to canonical IFNAR signaling (*Irf1*, *Rsad2*, *Stat1*; Fig. S4A). Coincubation with 200  $\mu$ M 4sU for 2 h yielded a good incorporation rate (~5%; Fig. S4B and C) and did not change gene expression (Fig. S4D and E). This concentration was thus used in all metabolic RNA labeling conditions.

In total, 10,616 transcripts were detected across all samples. In response to ISD transfection, 28 transcripts were significantly (false discovery rate [FDR]  $\leq$  0.01) up- or downregulated in WT cells, and consistently, none of these were induced after ISD stimulation of IRF3<sup>-/-</sup> MEFs (defined as IRF3-dependent genes; Fig. S5A). Transcripts of type I IFNs themselves were not detected at sufficient levels for quantification. However, we could validate IRF3-dependent induction of *Irfb1* and *Irfn4* by RT-qPCR (Fig. S5C and D). By comparing the response to IFN- $\beta$  treatment between WT and IFNAR1<sup>-/-</sup> MEFs, we determined 2,888 transcripts that were significantly up- or downregulated dependent on type I IFN-mediated IFNAR1/IFNAR2 activation (defined as IFNAR1-dependent type I IFN-responsive [or IFNAR1-responsive] genes; Fig. S5B). Interestingly, another 130 transcripts were regulated by treatment with IFN- $\beta$  also in the IFNAR1<sup>-/-</sup> cells and thus independently of canonical type I IFN signaling (Fig. S5B). These 130 transcripts included well known NF- $\kappa$ B targets such as *Nfkbia*, *Tnfrsf3*, and *Cxcl5* (Table S4), highlighting the importance of defining ISG induction based on required signaling components, such as IFNAR1. Regulation of IRF3-dependent genes upon ISD transfection was comparable between WT and IFNAR1<sup>-/-</sup> cells (Fig. 8B) and vice versa for IFNAR1-responsive genes stimulated by IFN- $\beta$  treatment between WT and IRF3<sup>-/-</sup> cells (Fig. 8C). In addition, both the IRF3-dependent and the IFNAR1-responsive murine genes overlapped significantly (Fisher's exact test,  $P < 0.0001$ ) with IFN- $\alpha$ -responsive genes previously determined in human fibroblasts, as well as a conserved "core" of genes in human and nine further vertebrate species (74) (Fig. 8B and C).

Next, we examined the IRF3-dependent genes more closely. Comparing the IRF3-dependent and IFNAR1-responsive groups revealed that 20 of the 28 IRF3-dependent genes were also responsive to IFNAR1/IFNAR2 activation (Fig. 8D; Fisher's exact test,  $P < 0.0001$ ). Moreover, of the remaining 8 IRF3-dependent genes, another 7 responded to IFN- $\beta$  treatment, although in both WT and IFNAR1<sup>-/-</sup> cells. Overall, the induction of IRF3-dependent genes was even more pronounced after stimulation via IFNAR activation than via PRR signaling (Fig. S5E). Thus, IRF3-dependent genes represent a small subset within the over100-times bigger group of IFNAR1-responsive genes (Fig. S5F). Accordingly, expression of IFNAR1-responsive genes is well correlated between IFN- $\beta$  treatment of WT and IRF3<sup>-/-</sup> MEFs (Spearman correlation  $r = 0.95$ ), but not between ISD stimulation of WT and



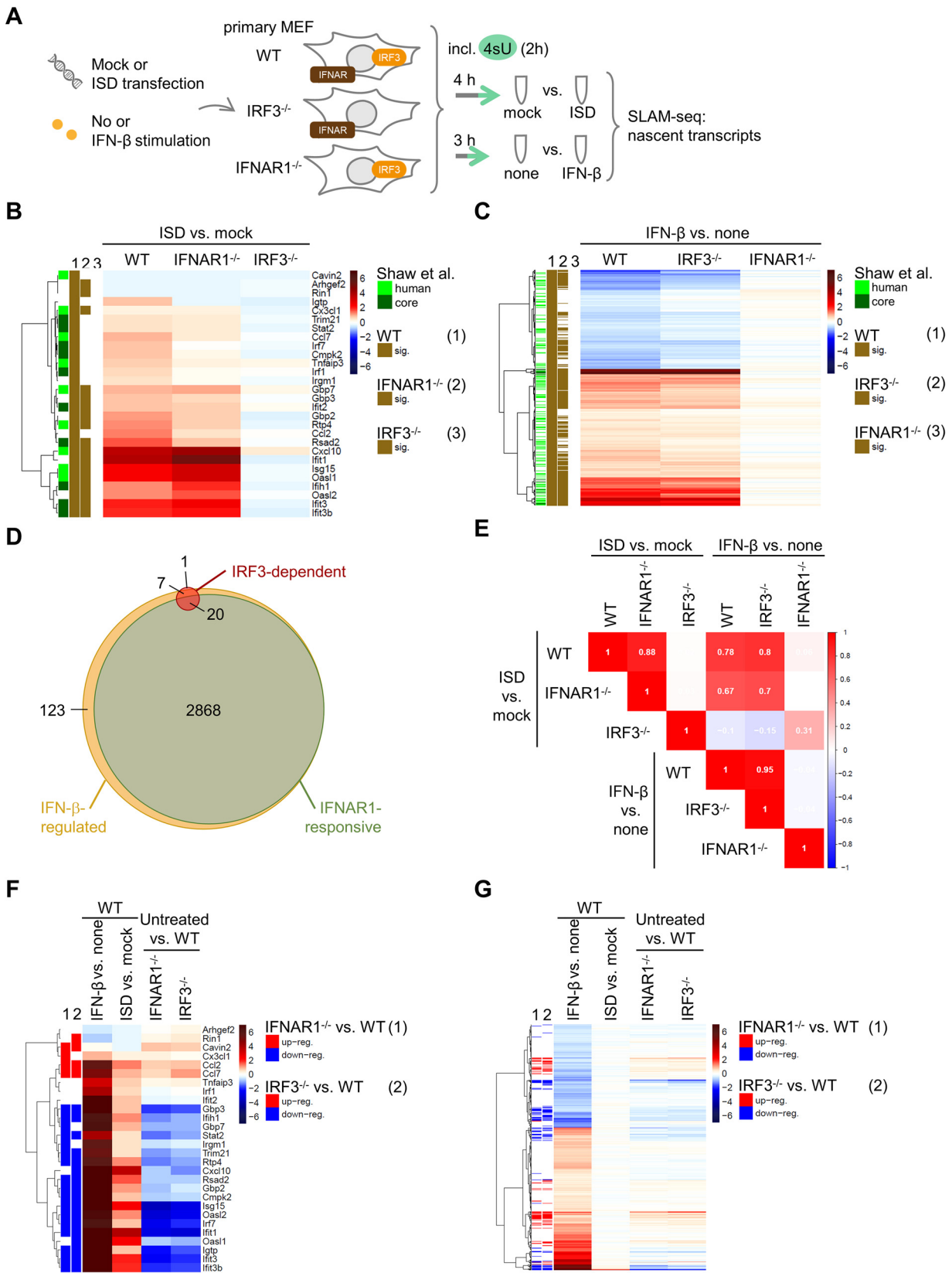


**FIG 8** RNA sequencing of metabolically labeled transcripts (SLAM-seq) for characterization of the dependency of immunostimulatory DNA (ISD)-stimulated transcripts on IRF3 or of IFN-β-stimulated transcripts on canonical type I IFN-IFNAR1/IFNAR2 signaling in murine embryonic fibroblasts (MEFs). (A) Determination of IRF3-dependent and IFNAR1-responsive transcripts. Primary MEFs of WT, IRF3<sup>-/-</sup>, or IFNAR1<sup>-/-</sup> mice (Continued on next page)

IFNAR1<sup>-/-</sup> cells ( $r = 0.06$ ). In contrast, the regulation of IRF3-dependent gene expression correlated well between ISD stimulation of WT and IFNAR1<sup>-/-</sup> cells ( $r = 0.88$ ), as well as between IFN- $\beta$  treatment of WT and IRF3<sup>-/-</sup> MEFs ( $r = 0.95$ ; Fig. 8E).

Furthermore, we observed that the absence of IRF3 or IFNAR1, two key components of the type I signaling system, markedly influenced the basal levels of many transcripts. Interestingly, while signaling via these factors resulted in vastly different numbers of induced genes (28 for IRF3, 2,888 for IFNAR1-responsive activation), similar numbers of transcripts were influenced by both knockouts (1,323 and 1,255 significantly deregulated transcripts in IRF3<sup>-/-</sup> and IFNAR1<sup>-/-</sup>, respectively, compared to WT). While the transcriptional profiles in untreated IRF3<sup>-/-</sup> and IFNAR1<sup>-/-</sup> cells were distinct from WT cells, expression changes compared to WT were highly similar between the two knockouts (Fig. S6A and B). Especially the basal levels of most IRF3-dependent genes were evidently affected by absence of IRF3 or IFNAR1, with most transcripts showing lower basal levels in the IRF3<sup>-/-</sup> or IFNAR1<sup>-/-</sup> cells compared to WT cells (Fig. 8F). Similarly, the knockouts affected the basal expression of many IFNAR1-responsive genes, again with a similar outcome (Fig. 8G). In addition, analysis of the transcripts differentially regulated in IRF3<sup>-/-</sup> or IFNAR1<sup>-/-</sup> compared to WT MEFs for enriched biological processes based on Gene Ontology (GO) indicated that deregulation of the type I IFN signaling system affects not only immune system processes and the response to stimulation but also further processes in multicellular organisms like the regulation of cell motility, cell adhesion, and vasculature development (Table S5).

Overall, we identified 28 IRF3-dependent genes in MEFs and observed that almost all of these were also inducible by canonical type I IFN signaling. Of note, the absence of critical components of the type I IFN response greatly impacted the basal levels of many transcripts, including a large fraction of ISGs.

**M35 modulates expression of several IRF3-dependent genes.** Having defined the IRF3-dependent and IFNAR1-responsive genes in MEF, we next addressed the effect of M35 on cellular gene expression after PRR stimulation, with special regard to IRF3-driven genes. For this, we generated iMEFs that constitutively express M35-HAHA. As expected, these cells showed reduced induction of *Irf3* transcription upon PRR stimulation compared to an empty vector (EV) control cell line (Fig. S7A to D).

Based on the kinetics of *Irf3* expression in EV iMEFs upon stimulation with Alexa Fluor 488-labeled ISD (Fig. S7E), the cells were transfected with ISD or mock-transfected for 2, 4, or 6 h and analyzed by SLAM-seq alongside untreated cells (Fig. 9A). Interestingly, application of the labeling protocol established before (200  $\mu$ M 4sU applied to label RNA for 90 min before harvest) did not achieve sufficient incorporation in this experiment. The underlying metabolic mechanism will require further studies. Accordingly, we had to restrict our analysis to total RNA transcript numbers. As expected from the *Irf3* expression kinetic, 2 h was too early to observe a major response (Fig. S8A, left). To our surprise, there was no striking difference in the gene induction in M35-HAHA compared to EV iMEFs at the peak of *Irf3* transcription (Fig. S7E) after 4 h of stimulation (Fig. S8A, middle). Only 6 h after stimulation, several transcripts were more strongly induced in EV compared to M35-expressing cells (Fig. S8A, right).

### FIG 8 Legend (Continued)

were stimulated by transfection of 5  $\mu$ g/mL ISD for 4 h or mock-transfected or stimulated with 100 U/mL of murine IFN- $\beta$  for 3 h or left untreated. Transcripts were labeled in the last 2 h of stimulation by incubation with 200  $\mu$ M 4-thiouridine (4sU) and analyzed by SLAM-seq. The samples were prepared and analyzed in quadruplicate. (B, C) Heat maps showing the log<sub>2</sub> fold changes (log<sub>2</sub>FC; blue, downregulation; red, upregulation) in the indicated cell lines for the 28 IRF3-dependent genes detected after ISD stimulation (B) or the 2,888 IFNAR1-responsive genes detected after IFN- $\beta$  treatment (C). Transcripts with a false discovery rate (FDR)  $\leq 0.01$  were considered statistically significant. The green marks on the left indicate overlaps with IFN- $\alpha$ -responsive genes in human fibroblasts or conserved (core) between 10 different species (74), and brown marks show significant regulation in the different cells. Genes were clustered according to Euclidean distances with Ward's clustering criterion. (D) Venn diagram showing overlaps of genes regulated in an IRF3-specific manner in response to ISD treatment (IRF3-dependent genes), regulated upon IFN- $\beta$  treatment in WT MEFs (independent of regulation in IFNAR1<sup>-/-</sup> cells), or regulated by IFN- $\beta$  only in WT but not IFNAR1<sup>-/-</sup> MEFs (IFNAR1-responsive genes). (E) Correlation plot showing spearman correlation for pairwise comparisons of log<sub>2</sub>FC for indicated treatments and cell lines for IRF3-dependent genes. Blue, negative correlation; red, positive correlation. (F, G) Heat maps showing the log<sub>2</sub>FC of IRF3-dependent (F) or IFNAR1-responsive (G) genes in WT cells after IFN- $\beta$  or ISD treatment compared to controls and in untreated knockout cell lines compared to WT. Blue, downregulation; red, upregulation. Genes significantly differentially expressed (FDR  $\leq 0.01$ ) in IFNAR1<sup>-/-</sup> (1) or IRF3<sup>-/-</sup> (2) compared to WT MEFs are marked on the left. Blue, downregulation; red, upregulation. IFNAR, interferon  $\alpha/\beta$  receptor.

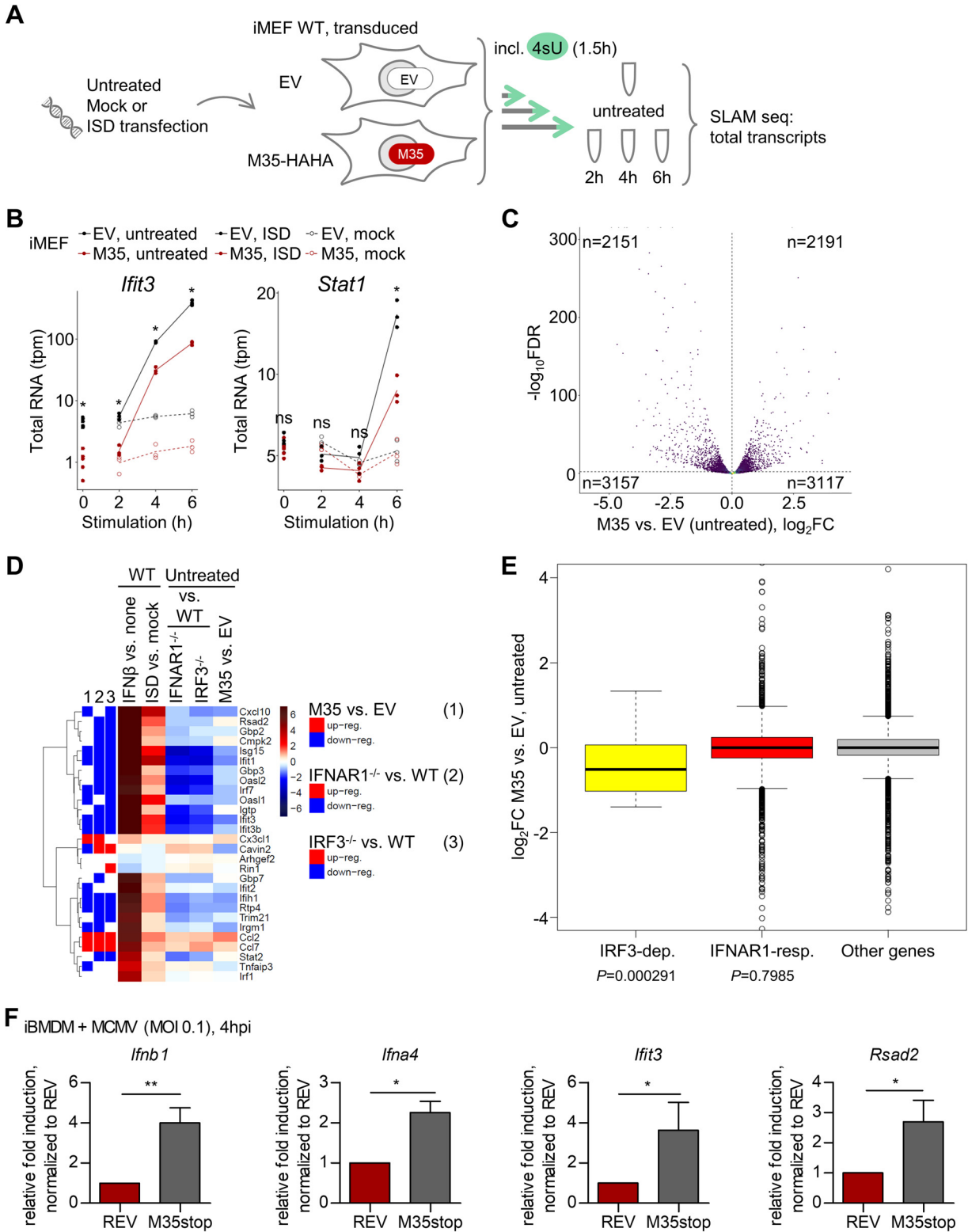


**FIG 9** Presence of M35 modulates expression of IRF3-dependent genes. (A) Determination of the global effect of M35's presence on gene expression. iMEFs stably expressing M35-HAHA or a corresponding EV were stimulated by transfection of 5  $\mu$ g/mL ISD, mock-transfected, or left untreated and incubated for indicated times. Transcripts were labeled in the last 90 min of stimulation by incubation with 200  $\mu$ M 4-thiouridine (4sU). The total transcripts were analyzed by SLAM-seq. The samples were prepared and analyzed in triplicate. (B) Expression kinetics of selected transcripts upon PRR stimulation in EV and M35-HAHA iMEFs. Total RNA counts are given in transcripts per million (tpm). Differences between transcript levels in ISD-stimulated EV and M35-HAHA iMEFs with  $FDR < 0.01$  were considered statistically significant (\*). ns, not significant. (C) Volcano plot showing differential expression of total cellular transcripts in EV compared to M35-HAHA iMEFs in untreated

(Continued on next page)

We then studied the expression kinetic of individual antiviral genes and found that IRF3-dependent genes such as *Ifit3* were well induced in EV cells after stimulation, as expected, but also in M35-expressing cells (Fig. 9B). After 6 h of stimulation, transcription of type I IFN signaling-dependent genes like *Stat1* was upregulated, reflecting activity of IRF3-dependently produced type I IFNs and subsequent IFNAR signaling. Induction of these genes was lower in M35-expressing cells, presumably due to the reduction of type I IFN production in the presence of M35. This indicates that on top of the putative direct effect(s) of M35, indirect effects of M35's antagonism of type I IFN induction contribute to gene regulation after 6 h of stimulation.

Although the presence of M35 had no major effect on the fold change of induction upon stimulation compared to control cells, our analyses revealed that thousands of transcripts already exhibited different basal levels in M35-expressing cells (Fig. 9C): A total of 2,151 transcripts were downregulated and 2,191 transcripts were upregulated in the presence of M35 compared to control cells (FDR < 0.01) even in the absence of IRF3 activation. Focusing first on the IRF3-dependent genes due to the proposed antagonism of M35 with IRF3-DNA binding, we found that more than half of the IRF3-dependent genes were differentially regulated in the presence of M35 (16 of 28 genes;  $P = 0.06$ ; Fig. 9D). Of those, 13 IRF3-dependent genes were significantly downregulated, and 3 were upregulated. Remarkably, the pattern of up- or downregulation of basal expression of IRF3-dependent genes in stably M35-expressing cells was highly similar to the pattern observed in the IRF3<sup>-/-</sup> or the IFNAR1<sup>-/-</sup> MEFs (Fig. 9D). Accordingly, the transcriptional profile of the IRF3-dependent genes in M35-expressing cells compared to EV cells correlated positively with IRF3<sup>-/-</sup> and IFNAR1<sup>-/-</sup> MEFs and negatively with the induction of those genes by ISD transfection (Fig. S8B). Regarding the effect of M35's presence on IFNAR1-responsive genes, we found that M35 caused differential regulation of a significant fraction of these transcripts (overlap of 1,373 genes,  $P < 0.0001$ ), but the regulation did not correlate with the trends of any of the other tested conditions (Fig. S8C and D). Finally, we compared basal levels of IRF3-dependent, IFNAR1-responsive, and all further transcripts in M35-expressing versus EV control cells. This revealed that the presence of M35 overall significantly downregulated IRF3-dependent gene expression, while this tendency was not observed for IFNAR1-responsive or other regulated genes (Fig. 9E).

All in all, we observed that the presence of M35 broadly affects basal gene expression in iMEFs, similar to knockouts of IRF3 or IFNAR1, and specifically downregulates expression of IRF3-dependent genes. While this effect was independent of PRR stimulation, this result supports our findings that M35 specifically modulates transcription of IRF3-targeted genes aside from *Ifnb1*.

To address a direct modulation of IRF3-dependent gene induction by M35 in the infection context, we compared the response elicited by MCMV M35stop, a recombinant that lacks M35 due to introduction of a Stop cassette within the ORF in the viral genome, to the revertant virus (MCMV REV) in which expression of M35 was restored. We infected immortalized bone marrow-derived macrophages (iBMDMs), because the effect of M35 on viral replication was best observable in these cells (54), and assessed

### FIG 9 Legend (Continued)

conditions as  $\log_2FC$  ( $x$  axis), plotted against  $-\log_{10}$  of the FDR ( $y$  axis, with significantly [FDR < 0.01] regulated transcripts above the dashed horizontal line). The numbers indicate total up- ( $\log_2FC > 0$ ) or downregulated ( $\log_2FC < 0$ ) transcripts in the respective sections. (D) Heat maps showing the  $\log_2FC$  in the indicated SLAM-seq samples for the 28 IRF3-dependent genes. Blue, downregulation; red, upregulation. Genes differentially expressed (FDR  $\leq 0.01$ ) in M35-expressing (1) compared to EV iMEFs or in IFNAR1<sup>-/-</sup> (2) or IRF3<sup>-/-</sup> (3) compared to WT MEFs are marked at the left. Blue, downregulation; red, upregulation. (E) Box plots showing the distribution of  $\log_2FC$  in M35-HAHA compared to EV iMEFs for IRF3-dependent ISD-responsive genes (IRF3-dep.), IFNAR1-dependent IFN- $\beta$ -responsive genes (IFNAR1-resp.), and other differentially expressed genes (other genes). The  $P$  values comparing median  $\log_2FC$  for IRF3-dependent and IFNAR1-responsive genes, respectively, to other genes were calculated by Wilcoxon rank sum test and are indicated below. (F) Response of IRF3-dependent genes upon infection with MCMV with or without M35. Immortalized bone marrow-derived macrophages (iBMDMs) pretreated with 1  $\mu$ M ruxolitinib (IFNAR signaling inhibitor) were infected with MCMV M35stopRevertant (REV) or MCMV M35stop (M35stop) at a multiplicity of infection (MOI) of 0.1 or mock-infected. The cells were harvested 4 h post-infection for reverse transcription (RT)-qPCR analysis. Relative fold induction of *Ifnb1*, *Ifna4*, *Ifit3*, and *Rsad2* transcripts was calculated based on the housekeeping gene *Rpl8*, and the values were normalized to REV-infected samples. The data are shown as means  $\pm$  SD and combined from two (*Ifna4*) or three (*Ifnb1*, *Ifit3*, and *Rsad2*) independent experiments. Significance compared to infection with REV was calculated by Student's  $t$  test (unpaired, two-tailed). \*,  $P < 0.05$ ; \*\*,  $P < 0.01$ .

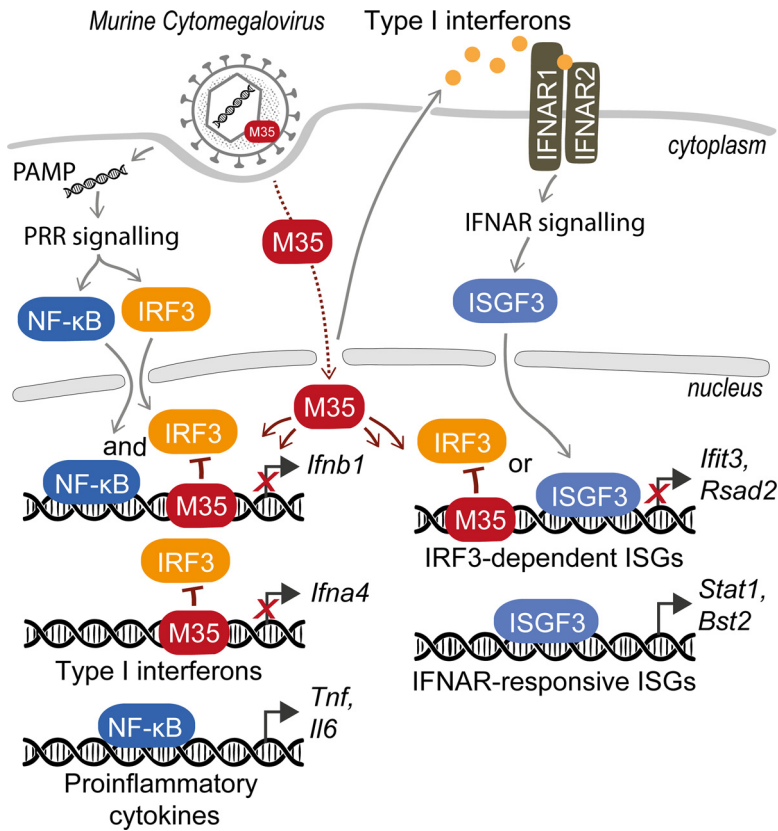


**FIG 10** M35 binds to specific host promoters and interferes with IRF3-dependent gene expression. Upon infection of a host cell with MCMV, pathogen-associated molecular patterns (PAMPs) are sensed by pattern-recognition receptors (PRRs) and activate the transcription factors NF- $\kappa$ B and IRF3. NF- $\kappa$ B induces expression of proinflammatory cytokines, NF- $\kappa$ B and IRF3 together induce expression of *Ifnb1*, and IRF3 regulates expression of further type I interferons (IFNs) and induces a subset of the interferon-stimulated genes (ISGs). Released type I IFNs activate the type I IFN receptor (IFNAR). IFNAR signaling induces assembly of different transcription factor complexes, mainly ISG factor 3 (ISGF3), which further drives expression of various ISGs. During MCMV infection, the viral tegument protein M35 is released and rapidly shuttles to the nucleus. M35 binds to IRF3-targeted recognition elements in host promoters and thus antagonizes recruitment of IRF3, resulting in inhibition of IRF3-driven gene expression.

induction of individual transcripts after 4 h by RT-qPCR. To rule out that type I IFN production and subsequent IFNAR signaling influenced the results, the cells were additionally treated with the IFNAR signaling inhibitor ruxolitinib (75) (Fig. S9A). As expected, the absence of M35 resulted in a higher increase of *Ifnb1* and *Ifna4* transcription early after infection (Fig. 9F). Moreover, transcription of the IRF3-dependent genes *Ifit3* and *Rsad2* was significantly increased upon infection with MCMV M35stop compared to MCMV REV. Comparing the fold inductions of the analyzed transcripts reflects that the transactivation of *Ifnb1* is among the strongest responses at this early time point after infection (Fig. S9B). Expression of *Stat1* was not detectable after infection, as expected after inhibition of type I IFN signaling. In contrast to IRF3-driven expression, transcription of the NF- $\kappa$ B-dependent genes *Nfkb1a* and *Tgfb1* was not affected by the presence or absence of M35 during infection (Fig. S9C). This demonstrates that the tegument protein M35 directly antagonized IRF3-mediated gene induction early during MCMV infection and that this is independent of M35's inhibition of type I IFN expression and subsequent IFNAR signaling (Fig. 10).

## DISCUSSION

To successfully establish persistent infections, members of all herpesvirus subfamilies dedicate a substantial number of gene products to target PRR signaling and induction of type I IFNs (76). We previously identified MCMV M35 as the first CMV antagonist of type I

IFN expression and showed its crucial role during infection of the host. In this study, we characterize the structure of the M35 protein and describe the mechanism that this potent immune modulator applies to pave the way for a successful infection.

A previous study of M35's homolog HHV6B U14 had indicated instability of the full-length proteins due to intrinsically disordered C termini (60). In line with this, the M35 full-length protein was unstable after purification. However, the major N-terminal part of M35 (aa 2 to 458) could be purified and allowed to crystallize the protein and solve its structure. Importantly, this structured domain retained the immunomodulatory activity of M35, demonstrating its contribution to the protein's function. A loop structure near the  $\beta$ -hairpins was not resolved in the crystal structure of M35, but reverse genetic analysis showed that this loop is not essential for M35's function. The corresponding segment was resolved in the structure of HHV6B U14 (60), suggesting that the part generally allows crystallization. Instead, we propose that in the crystal form of M35 obtained here, this region lacked the necessary contacts to keep the loops in an ordered conformation. Combining the data of the crystal structure, SEC-MALS, coimmunoprecipitation, and native PAGE, our findings demonstrate that M35 forms homodimers and does so independently of experimental conditions. This is in contrast to the prediction by Wang and colleagues suggesting that MCMV M35 and HCMV UL35 would not dimerize because they featured markedly different residues at the interface than the *Roseolovirus* U14 proteins (60).

Although the MCMV M35 crystal structure is overall similar to that of HHV6B U14, the relatively high RMSD value yielded for comparison of both dimers indicates substantial deviations, reflecting that these proteins are representatives of a family that has diverged significantly in the course of evolution. Consistently, our investigations suggest that the immunomodulatory function is not generally conserved in the members of the pp85 protein superfamily. In line with our observations, a recent study shows that HHV6A U14 does not significantly modulate the activity of the 125-bp human *Irfb1* promoter in the absence of PRR stimulation, although it interacts with p65 and increases expression of NF- $\kappa$ B dependent promoters (77). Still, downmodulation of *Irfb1* promoter induction by HHV7 U14 indicates that at least one further homolog might share M35's immunomodulatory activity. Comparably low protein levels were obtained for all U14 proteins, although they were expressed from the same vector as M35. The inhibitory phenotype of HHV7 U14 was weak compared to M35, but since it was observable with both epitope-tagged or untagged variants and despite the low expression level, we conclude that the effect is specific to the HHV7 U14 ORF and that the protein levels very likely do not explain the differences in the putative U14 activities. We recently reported that the HCMV homolog of M35, UL35, also impairs IFN- $\beta$  production, although modulation occurs at a different level than by M35 (57). This highlights that while the two CMV homologs assumed related roles to support viral replication, they adapted different strategies to inhibit type I IFN induction. It remains to be determined whether HHV7 U14 influences *Irfb1* expression using a similar mechanism to M35 or UL35 or even uses a yet unknown way, but this is beyond the scope of this study.

Using reverse genetics, we found that the pair of  $\beta$ -hairpins, which seems to interlock the M35 moieties like two thumbs interlock a handshake, is essential for M35's function. Interestingly, another critical residue, R69, is localized at the opposite side from the  $\beta$ -hairpins but also directly at the dimer interface. Conspicuously, protein levels of both loss-of-function derivatives ( $\Delta\beta$  and R69A) were reduced compared to WT M35 in cell lysates, but since very small amounts of WT M35 protein sufficed to inhibit luciferase induction in our *Irfb1* reporter assay, this alone would not explain the loss-of-function. The formation of distinct nuclear speckles of M35  $\Delta\beta$  further added to the impression that this loss-of-function mutation corrupted the protein. In contrast, M35 R69A displayed a WT-like nuclear distribution. Remarkably, native PAGE showed that both  $\Delta\beta$  and R69A severely impaired dimerization, revealing that exchange of a single position could critically influence integrity of the M35 dimer. This finding highlighted

that dimerization is an essential feature of M35 and related to the immunomodulatory function.

The purified M35<sub>S</sub> protein enabled us to confirm specific binding of M35 to the IFN- $\beta$  enhancer dsDNA *in vitro*. At high M35<sub>S</sub> concentration, a second band appeared that ran higher than the initial DNA-protein complex. This might indicate (i) the formation of multimeric complexes in which M35-DNA complexes interact with not DNA-bound M35 proteins or (ii) formation of higher-order complexes in which several M35 dimers bind to the DNA probe, as observed at high concentrations of IRF3 (32). Cooperative binding was also indicated from affinity measurements by the Hill coefficient ( $h > 1$ ). Assuming that M35 binds to DNA as dimeric entity and given that no other viral or cellular proteins were present in the reactions, these observations support the possibility of binding of several M35 dimers to one dsDNA strand. The overlapping IREs span about 25 bp in total, and the IRF3/7 dimers are proposed to bind from two sides. Likewise, and in agreement with M35's binding prerequisites, M35 could bind with two dimers, each from one side of the DNA duplex.

The IFN- $\beta$  enhancer sequence itself is accessible for transcription factors in steady state (78), supporting a model of direct M35-DNA binding. We determined a  $K_d$  of 2  $\mu$ M for binding of M35 to the murine IFN- $\beta$  enhancer sequence, but since concentrations applied in EMSAs refer to the M35<sub>S</sub> monomer, this translates into a  $K_d$  of about 1  $\mu$ M for dimeric M35. Based on the EMSA and ChIP, we propose that M35 antagonizes binding of IRF3, which displays a similar range of affinity ( $K_d \sim 1 \mu$ M) (79). However, for successful recruitment to the IFN- $\beta$  enhancer, IRF3 requires PRR signaling-induced phosphorylation, dimerization, and interaction with the coactivator CBP/p300 to overcome its intrinsically low DNA affinity (80, 81). Accordingly, with a  $K_d$  of 6 nM, the phosphomimetic IRF3-5D dimer features a distinctively higher affinity than WT IRF3 (79). We have to consider, however, that all of these affinity measurements examined isolated proteins and synthetic dsDNA probes, depriving their interactions of the natural environment. Application of the purified M35 protein gave rise to a specific protein-DNA complex, demonstrating that in general, no host factors or further viral factors are required for M35-DNA binding. Still, host factors, DNA modifications, and the environment of the promoter in the cell could greatly influence the ability and affinity of M35 to bind to DNA and contribute to its efficient recruitment. In this way, the relatively weak intrinsic affinity of M35 in the low micromolar range could suffice to antagonize binding of endogenous IRF3 after PRR activation. SLAM-seq showed that stable expression of M35 inhibited but did not abolish the induction of IRF3-dependent genes, potentially reflecting displacement of promoter-bound M35 by IRF3 in the course of the response. Against our expectations, constitutive expression of M35 led to downmodulation of IRF3-dependent gene expression already in unstimulated cells. Nevertheless, exogenous expression enabled study of the immunomodulatory activity of M35, and ChIP demonstrated that recruitment of IRF3 to the *Irfb1* promoter was severely impaired in M35's presence. In the context of infection, viral factors such as the reported interaction partners of M35 may further regulate its immunomodulatory activity (82), and characterization of their interplay will greatly add to our understanding of CMV immunomodulation.

To formally validate binding of M35 to the host DNA in its native environment, we performed ChIP experiments with the stably M35-expressing cell line or of host cells infected with MCMV REV and MCMV M35stop. However, while M35 protein itself could be precipitated with an epitope tag- or M35-specific antibody, we could not detect specific enrichment of any host DNA sequences after M35-specific immunoprecipitation by qPCR or unbiased high-throughput sequencing. Detection of transient and low-abundant interactions is a common pitfall in ChIP assays, especially when sample material is limited, and inaccessibility of chromatin-bound M35 for antibodies or changes of the targeted epitope due to formaldehyde cross-linking may prevent this approach from succeeding.

Nonetheless, the DNA-binding ability of M35 opened the possibility that M35 might modulate expression of further genes aside from *Irfb1*. As an alternative approach, we studied M35's effect on global gene expression with SLAM-seq to allow the unbiased measurement of transcript levels at a wide dynamic range and with additional

temporal resolution by detection of newly synthesized transcripts (71, 83, 84). The herein determined group of ISD-stimulated IRF3-dependent genes is in agreement with those detected upon stimulation of RIG-I signaling in murine cells using mRNA microarrays (20, 85). Likewise, the type I IFN-regulated genes detected in fibroblasts of other species by mRNA sequencing agree with the IFNAR1-responsive group (74). Induction of type I IFN genes could be quantified only by probe-based RT-qPCR, demonstrating its unmatched sensitivity and persisting value for detection of low-abundant transcripts. While in total more than one quarter of the detected gene products responded to IFN- $\beta$  treatment, IRF3 activation regulated only a small group. Moreover, almost all IRF3-dependent genes were also IFNAR1-responsive, underlining the role of IRF3 in priming the induction of a subset of ISGs before type I IFN signaling elicits the full potential of the antiviral response. We also detected IFNAR1-independent IFN- $\beta$ -stimulated regulation of transcripts commonly attributed to the NF- $\kappa$ B-driven response. This may indicate an impurity in the applied IFN- $\beta$  or IFNAR1-independent activation of signaling cascades via IFNAR2 homodimerization as suggested before (86, 87). Moreover, knockout of IRF3 or IFNAR1 severely affects the signaling circuits of the cell-intrinsic antiviral response, including basal transcription of critical signaling components that are themselves ISGs, such as *Stat1*, *Stat2*, and *Irf9*, consistent with previous reports (85). Accordingly, we based our definitions on the responses of WT cells and compared these to the respective knockouts to exclude unspecific responses.

Expressing M35 in iMEFs revealed that its presence alone greatly changed the cellular transcriptome and systematically modulated expression of IRF3-dependent genes. While this correlated with the changes observed in IRF3<sup>-/-</sup> or IFNAR1<sup>-/-</sup> fibroblasts, overexpression of M35 did not simply phenocopy deregulation of the type I IFN system but has discrete effects. We assume that secondary effects contributed to the transcriptional changes of stably M35-expressing cells, such as downmodulation of signaling components, and at least partly obscured M35's direct effect on gene expression. Therefore, we concluded our analysis by confirming that independently of the known antagonism of type I IFN signaling, virus-delivered M35 inhibited the induction of IRF3-dependent genes early in MCMV infection.

Taken together, we propose that tegument-delivered M35 directly binds to selected promoters and in this way antagonizes binding of IRF3 to overlapping recognition sites. The previous characterization of M35 indicated an antagonism of M35 with NF- $\kappa$ B based on (i) M35-mediated downmodulation of induction of an artificial NF- $\kappa$ B luciferase reporter and (ii) correlation of M35's phenotype with reduced levels of proinflammatory TNF- $\alpha$  in macrophages at 16 h post-infection. Our latest data demonstrate that the NF- $\kappa$ B motif was not required for M35-DNA binding in EMSA, nor did M35 antagonize *Irfb1* promoter induction by GFP-p65. Instead, the antagonism of M35 with IRF3 now suggests that the observed modulation of the NF- $\kappa$ B-mediated response is a secondary effect of M35-mediated modulation of the type I IFN response. With this and the speed of type I IFN signaling in mind, we ensured monitoring of direct effects for the present study by assaying early time points after PRR stimulation or after infection and additional inhibition of IFNAR signaling during infection.

Interestingly, a similar antagonism of IRF3-promoter binding is also employed by three unrelated proteins from the *Beta*- and *Gammaherpesvirinae*: namely, the DNA polymerase subunit UL44 of HCMV (63), the latency-associated nuclear antigen (LANA-1) of KSHV (64), and the transcriptional repressor K-bZIP of KSHV (62). In line with the different evolutionary origins of the proteins, the available information, although limited, does not indicate any structural similarities. Like M35, these three proteins localize to the nucleus, bind to the sequence of the IFN- $\beta$  enhancer, reduce binding of IRF3 to the *Irfb1* promoter sequence, and inhibit expression of *Irfb1* and at least one further IRF3-dependent gene. However, the studies of the other antagonists of IRF3-DNA binding had to rely on ectopically expressed proteins, limiting their characterization regarding timing of activity and impact on viral fitness. We generated a recombinant MCMV deficient in M35 expression and application of this virus enabled more detailed



characterization of M35's influence during MCMV infection (54). We demonstrated that M35 is necessary for the virus to successfully replicate in cell culture, as well as in the host organism (54), and that upon infection, tegument-delivered M35 immediately and directly counters induction of IRF3-dependent transcripts. In addition, by examining the global effect of M35 on cellular gene expression, we discovered that M35 not only influences the antiviral response by downregulating type I IFNs but also directly affects expression of several IRF3-dependent genes.

Overall, our data illustrate M35 as a specific inhibitor of IRF3-mediated regulation of antiviral genes. We found that by deploying M35, MCMV targets an essential step of the host response and influences the type I IFN response more broadly than anticipated. MCMV also deploys the protein m152 to modulate induction of type I IFNs (55). Remarkably, m152 delays the activation of IRF3 downstream of the DNA sensor cGAS and thus impairs the type I IFN response but allows activation and signaling of NF- $\kappa$ B to harness its proviral benefits. A study by Kropp and colleagues indicated a proviral role of activated IRF3 for viral gene expression (88), letting us speculate that by modifying the activation of IRF3 with m152 and IRF3 binding to antiviral host promoters with M35, MCMV could exploit this host transcription factor for its own gene expression. Additional studies will be required to address the interplay and effect of the herpesviral immune modulators in the course of type I IFN signaling during viral infection, as well as the potential involvement and regulation of IRF3 and NF- $\kappa$ B in herpesviral gene expression.

## MATERIALS AND METHODS

**Mice for generation of primary cells.** The mice (C57BL/6J) were bred at the animal facility of the Helmholtz Centre for Infection Research in Braunschweig and maintained under specific-pathogen-free conditions in accordance with institutional, state, and federal guidelines. IRF3 and IFNAR1 knockout mice have been described (89, 90). Primary mouse embryonic fibroblasts (MEFs) from C57BL/6J mice were generated by standard protocol (91).

**Plasmids.** pRL-TK expressing *Renilla* luciferase under the control of the thymidine kinase (TK) promoter is commercially available (catalog no. E2241, Promega, Walldorf, Germany). pGL3basic-IFN- $\beta$ -Luc (*mlf1nb1*-FLuc) consists of the 812-bp murine *lfnb1* promoter region cloned into pGL3basic (Promega) upstream of the firefly luciferase gene (92). The firefly luciferase reporter plasmid p-125 (*hlf1nb1*-FLuc), consisting of the human *lfnb1* promoter region (-125 to +19), was kindly provided by Takashi Fujita (Kyoto University, Japan) (93). pFLAG-CMV-hulPS1 expressing Flag-MAVS was kindly provided by Friedemann Weber (Institute of Virology, Justus Liebig University Giessen, Germany) (94). pCMVBL IRF3-5D encoding constitutively active human IRF3 by containing five amino acid substitutions (S396D, S398D, S402D, S404D, and S405D) was kindly provided by John Hiscott (Institut Pasteur Cenci Bolognietti Foundation, Rome, Italy). pEGFP-C1-RelA (GFP-p65, catalog number 23255) is available from Addgene (Watertown, MA, USA). pIRES2-GFP (catalog number 6029-1), pQCXIH, and pQCXIP (catalog number 631516) vectors were purchased from Clontech Laboratories (Mountain View, CA, USA). pcDNA3.1+ empty vector (EV; catalog number V790-20) and pcDNA3.1 TOPO EV (catalog number K480001) are from Invitrogen (Thermo Fisher Scientific). pEGFP-C1-hIRF3 encoding human IRF3 N-terminally fused with eGFP (eGFP-IRF3) was kindly provided by Friedemann Weber (Institute of Virology, Justus Liebig University Giessen, Germany) (95).

Expression constructs for M35-V5/His, M34-V5/His, and M27-V5/His (all in pcDNA3.1 TOPO-V5/His) have been described previously (96). The expression construct pcDNA3.1 TOPO M35\_S (short: aa 1 to 452) was generated by PCR amplifying the M35 aa 1 to 452 sequence with a primer pair that introduces overhangs for restriction enzymes, digesting the product with BamHI and EcoRV and ligating it into pcDNA3.1 TOPO EV linearized with BamHI and PmeI.

Constructs for protein production were generated by PCR amplification of the coding sequences of full-length M35 protein (aa 1 to 519, nucleotides 45,915 to 47,471 of GenBank accession no. [GU305914](#)) and of C-terminally truncated M35 (aa 1 to 452, nucleotides 45,915 to 47,267 of GenBank accession no. [GU305914](#)) followed by sequence- and ligation-independent cloning (SLIC) (97) between the BamHI and AvrII sites of pCAD04, a modified pOpiE2 vector (98) with a Kozak consensus sequence (GGATCACCATGG) in place of pOpiE2's original BamHI site and an N-terminal Twin-Strep tag and TEV cleavage site (MASAWSHPQF EKGSGSGGGS GGSASWHPQF EKSGENLYFQ GS). pOpiE2 contains the promoter of the second immediate early gene of the baculovirus OpMNPV. The resulting plasmids were named pHER08\_M35\_S\_452\_NStr (NStr-M35\_S) and pHER09\_M35\_FL\_NStr (NStr-M35\_FL).

Packaging plasmids VSV-G encoding the envelop protein of vesicular stomatitis virus and gag-pol encoding the retroviral polyprotein group-specific antigen (gag) processed to structural proteins and reverse transcriptase (pol) were a kind gift from Boaz Tirosh (Hebrew University of Jerusalem, Jerusalem, Israel). The pQCXIH M35-myc/His has been described previously (54). For generation of M35 constructs with a C-terminal double hemagglutinin (HA) epitope tag, the HAHA sequence was fused in frame to the full-length M35 ORF by PCR amplification and subcloned into pcDNA3.1(+). M35-HAHA was then

cloned into pcDNA3.1 TOPO using HindIII and SacII restriction sites to generate pcDNA3.1 TOPO M35-HAHA with the same upstream backbone as M35-V5/His. To generate the transduction vector pQCXIP M35-HAHA, the M35-HAHA ORF was PCR amplified with a primer pair introducing overhangs for restriction enzymes, and the digested product was ligated into linearized pQCXIP vector using AgeI and BamHI sites. The expression construct pcDNA3.1 TOPO M35 (full-length) was generated by PCR amplifying M35 aa 1 to 519 from pcDNA3.1 TOPO M35-V5/His (WT) with a T7fwd standard primer and a reverse primer that introduces a stop codon directly after the M35 ORF followed by a PmeI restriction site and ligating the digested product into the linearized pcDNA3.1 TOPO EV using BamHI and PmeI restriction sites.

For the generation of U14 expression constructs based on pcDNA3.1 TOPO, the U14 ORFs of HHV6A (strain U1102), HHV6B (strain HST), and HHV7 (strain JI) were ordered as gBlock gene fragments (Integrated DNA Technologies, Leuven, Belgium) with the same upstream and downstream sequences as the M35 ORF in pcDNA3.1 TOPO M35-V5/His including the sequence of the V5/His epitope tag. gBlocks were subcloned into pcDNA3.1 TOPO EV using BamHI and NotI restriction sites to generate pcDNA3.1 TOPO U14-V5/His with the ORF of HHV6A or HHV6B or HHV7. From there, U14 ORFs with N-terminal triple V5 epitope tags (3×V5-U14) were generated by introducing the upstream sequence encoding the epitope tag and a triple GGS linker and a downstream stop codon alongside restriction sites with PCR primers, followed by ligation of the digested product into pcDNA3.1 TOPO using BamHI and PmeI restriction sites. Untagged U14 ORFs (U14) were generated accordingly by amplifying the ORF from the U14-V5/His subclones with a T7fwd standard primer and the reverse primer used for generation of 3×V5-U14. pcDNA3.1+ expression constructs for UL35-HAHA and untagged UL35 have been described previously (57).

The following M35 derivative constructs were derived from pcDNA3.1 TOPO M35-V5/His using the Q5 site-directed mutagenesis kit (catalog no. E0554, New England Biolabs) according to the manufacturer's protocol: (i) mutations of the  $\beta$ -hairpin: deletion of aa 406 to 424 ( $\Delta\beta$ ), deletion/insertion variants replacing aa 406 to 424 with a single G or P ( $\Delta\beta+G$  and  $\Delta\beta+P$ , respectively); (ii) mutations substituting the residues that form the positive patch: R10A/R20A, R99A/R102A, R257A/R260A, R99A/R102A/R257A/R260A, and R10A/R20A/R99A/R102A/R217A/R257A/R260A/R310A; (3) mutations that substitute the hydrophilic residues along the groove: N42A/R69A, K71A/H72A/R73A, H174A/R177A/D180A, K438A/R439A, N42A, and R69A; and (4) mutations of the loop that is unresolved in M35: deletion/insertion variants replacing aa T343 to R375 with GSG or GPG ( $\Delta T343-R375+GSG$ , short GSG, and  $\Delta T343-R375+GPG$ , short GPG, respectively) or replacing L349 to K373 with GSGS ( $\Delta L349-K373+GSGS$ , short: GSGS). Indicated positions refer to the protein sequence. Q5 mutagenesis was carried out sequentially to combine several point mutations.

All generated constructs were verified by sequencing. Sequences of primers and constructs are available upon request.

**Cell lines.** The mammalian cells were cultured at 37°C in a humidified incubator with 5% or 7.5% CO<sub>2</sub>. M2-10B4 (ATCC no. CRL-1972) and human embryonic kidney 293T (HEK293T; ATCC no. CRL-3216) cells were obtained from ATCC (Manassas, VA, USA) and maintained in Dulbecco's modified Eagle's medium (DMEM; high glucose) supplemented with 10% fetal calf serum (FCS), 2 mM glutamine (Gln), and 1% penicillin/streptomycin (P/S).

The immortalized WT murine bone marrow-derived macrophage (iBMDM) cell line was obtained through BEI Resources, NIAID, National Institutes of Health (NR-9456) and cultured in DMEM (high glucose) supplemented with 10% FCS, 2 mM Gln, 1% P/S, and 50  $\mu$ M  $\beta$ -mercaptoethanol.

Primary mouse embryonic fibroblasts (MEFs) derived from C57BL/6J mice were maintained in MEM supplemented with 10% FCS and 1% P/S. For generation of constitutively M35-expressing stable cell lines, primary MEFs were immortalized with SV40 Large T antigen to generate immortalized MEFs (iMEFs) and maintained in DMEM (high glucose) supplemented with 10% FCS, 1% P/S, 1× nonessential amino acids, and 50  $\mu$ M  $\beta$ -mercaptoethanol. Retroviral particles were generated by cotransfecting a confluent well of a 6-well plate of HEK293T cells with each 1.2  $\mu$ g of the packaging constructs encoding gag-pol and VSV-G and with 1.6  $\mu$ g of the retroviral transduction construct pQCXIH or pQCXIP for stable expression of the respective M35 derivative or with the corresponding empty vector (EV) using Lipofectamine 2000. After 48 h, the culture supernatant was filtered through a 0.45- $\mu$ m syringe-driven filter unit, mixed with Polybrene (Santa Cruz Biotechnology, Dallas, TX, USA) to reach a final concentration of 8  $\mu$ g/mL, and added to WT iMEF in viral harvest medium (DMEM, 20% FCS, P/S, 10 mM HEPES). The cells were centrifuged for 90 min at 800  $\times$  g at room temperature, transferred to 37°C for 3 h, and then the supernatant was changed to fresh medium. After 2 days, 250  $\mu$ g/mL hygromycin or 10  $\mu$ g/mL puromycin was added to the culture media to select for cells successfully transduced with the pQCXIH or pQCXIP vectors, respectively. This yielded M35-myc/His iMEF and M35-HAHA iMEF constitutively expressing M35 and their respective EV iMEF control cell lines.

The High-Five insect cell line (BTI-Tn-5B1-4, High-Five, Thermo Fisher Scientific) was a kind gift from the Boyce Thompson Institute for Plant Research (Ithaca, NY, USA). High-Five cells adapted to EX-CELL 405 medium (Sigma-Aldrich, Darmstadt, Germany) were maintained in suspension culture at 27°C (130 rpm) in exponential growth and diluted by passaging to 0.4 to 0.6  $\times$  10<sup>6</sup> cells/mL every 2 or 3 days (98).

**Viruses.** Generation of MCMV M35stop and MCMV M35stopREV and preparation of MCMV stocks were reported previously (54). In brief, the MCK-2 repaired genome of MCMV strain Smith carried on a bacterial artificial chromosome (BAC) was manipulated by introduction of a stop cassette (GGCTAGTAACTAGCC) at nucleotide position 46,134 (accession no. [GU305914](https://www.ncbi.nlm.nih.gov/nuclot/GU305914)) within the M35 ORF to yield the genome of MCMV M35stop. A revertant of MCMV M35stop (REV) was generated by restoring the WT sequence and thus expression of the M35 ORF. M2-10B4 cells were transfected with the BAC DNA using JetPEI for reconstitution of MCMV M35stop (M35stop) and MCMV M35stopREV (REV), respectively. A single clone of each recombinant

virus was expanded on M2-10B4 cells, and virus from supernatants was concentrated and purified on a 10% Nycodenz cushion. Titers of virus stocks were determined by standard plaque assay on M2-10B4 cells.

**Antibodies and reagents.** Generation of the M35-specific monoclonal antibody M35C.01 ( $\alpha$ -M35) was described previously (54). Murine anti-V5 tag (clone 7/4, catalog no. 680602) and rabbit anti-V5 tag (Polyclonal, catalog no. 903801) antibodies were purchased from BioLegend (San Diego, CA, USA). Anti-V5 tag MAb-magnetic beads (catalog no. M167-11) were purchased from MBL International (Woburn, MA, USA). Anti-myc tag (clone 9E10, catalog no. 05-419) was purchased from Merck Millipore (Darmstadt, Germany). Rabbit anti-IRF3 antibody (polyclonal, catalog no. A303-383A) and rabbit IgG isotype control (catalog no. 120-101) for ChIP experiments were purchased from Bethyl Laboratories (Montgomery, TX, USA). Murine anti-myc tag (clone 9B11, catalog no. 2276), rabbit anti-phospho-IRF3 (clone 4D4G, Serine 396, catalog no. 4947), rabbit anti-fibrillarin (clone C13C3, catalog no. 2639), anti-GAPDH (clone 14C10, catalog no. 2118), and rabbit anti-HA tag (clone C29F4, catalog no. 3724) antibodies for immunoblots were purchased from Cell Signaling Technology (Frankfurt am Main, Germany). Mouse anti- $\beta$ -actin (clone AC-15, catalog no. A5441) antibody was purchased from Sigma-Aldrich. Horseradish peroxidase (HRP)-coupled GFP antibody (clone B-2, catalog no. sc-9996 HRP) was purchased from Santa Cruz Biotechnology (Heidelberg, Germany). Anti-mouse and anti-rabbit HRP-conjugated or Alexa Fluor 488-conjugated secondary antibodies were purchased from Dianova (Hamburg, Germany) and Invitrogen (Thermo Fisher Scientific), respectively. High molecular weight poly(I:C) (catalog no. tirl-pic) was purchased from Invivogen (San Diego, CA, USA).

Interferon-stimulatory DNA (ISD) was generated by mixing the complementary forward (ISD45 bp-for: 5'-TACAGATCTACTAGTATCTATGACTGATCTGTACATGACTACA) and reverse (ISD45 bp-rev: 5'-TG TAGATCATGTACAGATCAGTCATAGATCACTAGTAGATCTGTA) 45-bp oligonucleotides, heating to 70°C for 10 min, and then annealing at room temperature. For preparation of Alexa Fluor 488-labeled ISD, the forward oligonucleotide was ordered with a 5'-Alexa Fluor 488 conjugate and processed in the same way.

The transfection reagents Lipofectamine 2000 (catalog no. 11668019, Invitrogen, Thermo Fisher Scientific), FuGENE HD (catalog no. E2312, Promega, Walldorf, Germany), and linear polyethylenimine (PEI, 25K, catalog no. 23966-100, Polysciences, Warrington, PA, USA) were purchased from Life Technologies, Promega, and Polysciences, respectively. JetPEI was obtained from Polyplus (Illkirch, France). Gibco Opti-MEM, DMEM, and further additives for cell culture media were obtained from Thermo Fisher Scientific. Protease inhibitors (Pis, cComplete, catalog no. 4693116001) and phosphatase inhibitors (Phs, PhosSTOP, catalog no. 4906837001) were from Roche (Mannheim, Germany). Recombinant murine IFN- $\beta$  (catalog no. 12405-1) was ordered from PBL Assay Science (Piscataway, NJ, USA), and Ruxolitinib (IFNAR inhibitor, dissolved in DMSO, catalog no. S1378) was from Selleck Chemicals GmbH (Absource Diagnostics, Munich, Germany).

**Production and purification of recombinant proteins.** Full-length M35 and the M35\_S were produced by transient transfection of High-Five insect cells with the respective pHER plasmids, followed by purification of two steps of affinity chromatography. 1 L High-Five insect cell culture was transfected using PEI as described (99), resulting in about 25 g cell pellet (wet weight). The cells were resuspended in 50 mL lysis buffer (50 mM Tris, pH 7.4, 0.5 M NaCl, 10% glycerol, 1 mM Tris(2-carboxyethyl)phosphine hydrochloride [TCEP], 0.5% [vol/vol] IGEPAL CA-630) after addition of 1  $\mu$ L benzonase (25U/ $\mu$ L) and 1 tablet of PI and lysed by vortexing and repeated shearing by pressing the extract with a syringe through a needle of 0.9-mm diameter. Subsequently, the extract was cleared by two runs of centrifugation for 20 min at 16,000  $\times$  g in a Sorvall F18-12  $\times$  50, rotor (Thermo Fisher Scientific). The soluble protein fraction was filtered through a 0.45- $\mu$ m filter. First, the tagged NStr-M35\_FL or NStr-M35\_S protein were purified by StrepTactin Superflow high-capacity (IBA Lifesciences, Göttingen, Germany) chromatography with a 1 mL self-made column (Mobicol, MoBiTec GmbH, Göttingen, Germany) after preincubation in batch for 2 h at 4°C with the column material (primary purification). The column was rinsed with a wash buffer (50 mM Tris, pH 8.0, 0.5 M NaCl, 10% glycerol, 5 mM  $\beta$ -mercaptoethanol). For elution, 10 mM des-thiobiotin was added to the wash buffer, and eluates were collected at a flow rate of 1 mL/min in 0.5-mL fractions. The eluted fractions were analyzed by SDS-PAGE and stained with InstantBlue Coomassie protein stain. The eluted protein samples were pooled and digested overnight at 4°C using TEV-protease (2 mg/mL) at a ratio of 1:10 (TEV-protease:M35 protein). For the second and final purification, the untagged M35\_FL or M35\_S protein were purified on a Superdex 200 (26/60) column (Cytiva, Freiburg, Germany) using storage buffer (50 mM Tris, pH 7.4, 0.25 M NaCl, 10% glycerol, 1 mM dithiothreitol [DTT]).

**Luciferase-based reporter assays.** To study induction of the *lfnb1* promoter in the luciferase reporter assay, specific components of the signaling cascade were ectopically expressed to mimic pathway activation from a known level. For all reporter assays, 25,000 HEK293T cells were seeded in 96-well plates in 100  $\mu$ L of culture medium/well and transfected on the following day. All samples were transfected and measured in technical duplicates.

**(i) MAVS-stimulated assay of murine *lfnb1* reporter.** Cells were transiently transfected with 10 ng Flag-MAVS (stimulated) or pcDNA3.1(+) (unstimulated) together with 100 ng *mlfnb1*-FLuc, 10 ng pRL-TK, and 100 ng expression plasmid for the protein of interest complexed with 0.75  $\mu$ L FuGENE HD in 10  $\mu$ L Opti-MEM/well.

**(ii) MAVS-stimulated assay of human *lfnb1*-reporter.** Cells were transiently transfected with 10 ng Flag-MAVS (stimulated) or pcDNA3.1(+) (unstimulated) together with 50 ng *hlfnb1*-FLuc, 10 ng pRL-TK, and 100 ng expression plasmid for the protein of interest complexed with 0.75  $\mu$ L FuGENE HD in 10  $\mu$ L Opti-MEM/well.

**(iii) IRF3-5D-stimulated assay.** Cells were transiently transfected with 60 ng pIRF3-5D (stimulated) or pIRES2-GFP (unstimulated) together with 100 ng *mlfnb1*-FLuc, 10 ng pRL-TK, and 120 ng expression plasmid for the protein of interest complexed with 1.0  $\mu$ L FuGENE HD in 10  $\mu$ L Opti-MEM/well.

**(iv) p65-stimulated assay.** Cells were transiently transfected with 20 ng GFP-p65 (stimulated) or

**TABLE 1** Oligonucleotides used to generate EMSA probes<sup>a</sup>

Name <sup>b</sup>	Sequence (5' to 3') <sup>c</sup>
Bio_hIFN <sub>b</sub> _fwd	TAAATGACATAGGAAAAGCTGAAAGGGAGAAGTAAAGTGGGAAATTCCTCTGAATAG
Bio_hIFN <sub>b</sub> _rev	ACTATTCAGAGGAATTTCCCACTTTCACTTCTCCCTTTCAGTTTCTATGTCATTT
Bio_ScrHIFN <sub>b</sub> _fwd	ATAAGAGAACTAAGCGGAATAAGTAAGAGATGATCGGATTAGTCGCTAAGAAATGAGA
Bio_ScrHIFN <sub>b</sub> _rev	TTCTCATTCTAGCGACTAATCCGATCATCTTACTTATTCCGCTTACTTCTCTTA
Bio_hIFN <sub>b</sub> 1-38_fwd	TAAATGACATAGGAAAAGCTGAAAGGGAGAAGTAAAGT <u>GACATGCTACCGAATGAAT</u>
Bio_hIFN <sub>b</sub> 1-38_rev	AATTCATTCCGTAGCATGTCACCTTCACTTCTCCCTTTCAGTTTCTATGTCATTT
Bio_hIFN <sub>b</sub> 15-57_fwd	ATATAAGACGGAAATAAACTGAAAGGGAGAAGTAAAGTGGGAAATTCCTCTGAATAG
Bio_hIFN <sub>b</sub> 15-57_rev	ACTATTCAGAGGAATTTCCCACTTTCACTTCTCCCTTTCAGTTTATTCCGCTTATA
Bio_hIFN <sub>b</sub> 15-38_fwd	ATATAAGACGGAAATAAACTGAAAGGGAGAAGTAAAGT <u>GACATGCTACCGAATGAAT</u>
Bio_hIFN <sub>b</sub> 15-38_rev	AATTCATTCCGTAGCATGTCACCTTCACTTCTCCCTTTCAGTTTATTCCGCTTATA
Bio_hIFN <sub>b</sub> 18-29_fwd	ATAAGAGAACTAAGCTACTGAAAGGGAGATTGAGATGAATGACTAGGAATGAGAAGA
Bio_hIFN <sub>b</sub> 18-29_rev	TCTTCTATTCTAGTCATTCATCTCAATCTCCCTTTCAGTAGCTTAGTCTCTTAT
Bio_hIFN <sub>b</sub> 13-18_fwd	TAAATGACATAGATCTGATGAAAGGGAGAAGTAAAGTGGGAAATTCCTCTGAATAG
Bio_hIFN <sub>b</sub> 13-18_rev	CTATTCAGAGGAATTTCCCACTTTCACTTCTCCCTTTCATCAGATCATGTCATTTA
Bio_hIFN <sub>b</sub> 33-38_fwd	TAAATGACATAGGAAAAGCTGAAAGGGAGAAGT <u>ATCTGAGGGAAATTCCTCTGAATAG</u>
Bio_hIFN <sub>b</sub> 33-38_rev	CTATTCAGAGGAATTTCCCTCAGATACTTCTCCCTTTCAGTTTCTATGTCATTTA
Bio_hIFN <sub>b</sub> 19-25_fwd	TAAATGACATAGGAAAAGCTATCGCTGAGAAGTAAAGTGGGAAATTCCTCTGAATAG
Bio_hIFN <sub>b</sub> 19-25_rev	ACTATTCAGAGGAATTTCCCACTTTCACTTCTCAGCGATAGTTTCTATGTCATTT
Bio_hIFN <sub>b</sub> 25-30_fwd	TAAATGACATAGGAAAAGCTGAAAGT <u>TCGCTGTGAAAGTGGGAAATTCCTCTGAATAG</u>
Bio_hIFN <sub>b</sub> 25-30_rev	CTATTCAGAGGAATTTCCCACTTTCACTTCTCAGAGCATCTTTCAGTTTCTATGTCATTTA
Bio_hIFN <sub>b</sub> 13-18 33-38_fwd	TAAATGACATAGATCTGATGAAAGGGAGAAGT <u>ATCTGAGGGAAATTCCTCTGAATAG</u>
Bio_hIFN <sub>b</sub> 13-18 33-38_rev	ACTATTCAGAGGAATTTCCCTCAGATACTTCTCCCTTTCATCAGATCATGTCATTT
Bio_hIFN <sub>b</sub> 13-18 25-30_fwd	TAAATGACATAGATCTGATGAAAGT <u>TCGCTGTGAAAGTGGGAAATTCCTCTGAATAG</u>
Bio_hIFN <sub>b</sub> 13-18 25-30_rev	ACTATTCAGAGGAATTTCCCACTTTCACTTCTCAGCGATCTTTCATCAGATCATGTCATTT
Bio_hIFN <sub>b</sub> 19-25 33-38_fwd	TAAATGACATAGGAAAAGCTATCGCTGAGAAGT <u>ATCTGAGGGAAATTCCTCTGAATAG</u>
Bio_hIFN <sub>b</sub> 19-25 33-38_rev	ACTATTCAGAGGAATTTCCCTCAGATACTTCTCAGCGATAGTTTCTATGTCATTT
Bio_mIFN <sub>b</sub> _fwd	AAAATGACAGAGGAAAAGCTGAAAGGGAGAAGTAAAGTGGGAAATTCCTCTGAGGCA
Bio_mIFN <sub>b</sub> _rev	CTGCCTCAGAGGAATTTCCCACTTTCACTTCTCCCTTTCAGTTTCTATGTCATTT

<sup>a</sup>EMSA, electrophoretic mobility shift assay; fwd, forward; rev, reverse.

<sup>b</sup>All oligonucleotides used to prepare EMSA probes were 57 nucleotides long, with 5'-biotinylation, forming 56-bp double-stranded DNA upon annealing.

<sup>c</sup>Sequences replaced in mutant probes by random sequences are underlined in the respective forward primer.

pcDNA3.1(+), (unstimulated) together with 100 ng *mlf1b*-FLuc, 10 ng pRL-TK, and 200 ng expression plasmid for the protein of interest complexed with 1.1 µL FuGENE HD in 10 µL Opti-MEM/well.

For all luciferase assays, cells were lysed in 50 µL of 1× passive lysis buffer (Promega) per 96 wells at 20 h post-transfection. Luciferase production was measured with the Dual-Luciferase reporter assay system (Promega, catalog no. E1980) at a Tecan Infinite 200 Pro microplate luminometer (Tecan, Männedorf, Switzerland) with signal integration over 2,000 ms. Fold induction of firefly luciferase was calculated by dividing firefly luciferase values through *Renilla* luciferase values for normalization and then dividing obtained values from stimulated samples by the corresponding values from unstimulated samples.

**Electrophoretic mobility shift assay (EMSA).** Complementary 5'-biotinylated oligonucleotides pairs harboring the human or murine IFN-β enhancer sequence and corresponding mutated sequences (Table 1) were purchased from Integrated DNA Technologies (Leuven, Belgium). Sense and antisense oligonucleotides were annealed together at a 1:1 molar ratio in water at 95°C for 5 min, with the temperature decreasing 1°C/min until the corresponding melting temperature ( $T_m$ ) of the oligonucleotide pair (73°C) was reached, held for 30 min, followed by another 1°C/min decrease cycle until 4°C. The reactions were carried out according to the manufacturer's instructions with the Gelshift chemiluminescent EMSA kit (catalog no. 37341, Active Motif, Waterloo, Belgium). Purified M35<sub>5</sub> protein was diluted in storage buffer to reach the indicated concentration (0.1 to 10 µM, referring to the 50.1-kDa M35<sub>5</sub> monomer) and incubated in 1× kit binding buffer supplemented with 50 ng/µL poly(dI-dC), 0.05% (vol/vol) Nonidet P-40, 5 mM MgCl<sub>2</sub>, 1 mM EDTA, 50 mM KCl, and 3 µg bovine serum albumin (BSA) together with 2 fmol of the indicated biotinylated oligonucleotides. For competitive EMSA reactions, 200 fmol competitor (nonbiotinylated oligonucleotides) was added. The reaction mixtures were incubated for 30 min on ice. The sample was separated into DNA-protein complexes and free probes by electrophoresis of samples mixed with provided 5× loading dye on a 6% native polyacrylamide gel in 0.5× TBE containing 2.5% glycerol at 4°C. EMSA gels were prerun for at least 30 min at 4°C prior sample loading. Biotinylated DNA was transferred onto a nylon membrane (Amersham Hybond N+, catalog no. RPN203B, Cytiva, Freiburg, Germany) at 380 mA for 40 min at 4°C. The membranes were fixed with 120 J/cm<sup>2</sup> UV-B irradiation using a Bio-Link BXL cross-linker (Wilber Lourmat, Eberhardzell, Germany). Blocking, washing, and detection were performed using the Gelshift chemiluminescent EMSA kit according to the manufacturer's instructions. The membranes were imaged using a ChemoStar ECL Imager (INTAS, Göttingen, Germany).

For determination of the bound probe fraction, bands of the free probe and the complexed probe were quantified for each replicate using Fiji (version 1.53f51) (100). The relative band intensities of the complexed probe were divided by the total signal of the free and complexed probes to obtain the

bound fraction. The bound fractions determined in three independent experiments were plotted against the protein concentration in GraphPad Prism (version 5; GraphPad Software, San Diego, CA, USA) and fitted using the binding-saturation module "Specific binding with Hill slope."

**Protein crystallography.** Structure determination by protein crystallography followed standard protocols. Briefly, initial crystallization conditions were identified with automated procedures using the sitting-drop vapor-diffusion method. Crystallization experiments were performed at room temperature. Conditions for crystallization of M35\_S were determined using a NeXtal JCSG+ matrix screen (catalog no. 130920, NeXtal, Holland, OH, USA) and M35\_S (aa1-452 of 519) readily crystallized in well F10 (1.1 M Na<sub>2</sub> Malon, 0.1 M HEPES, pH 7.0, 0.5% [vol/vol], Jeffamine ED-2001). Therefore, equal amounts of precipitant solution were mixed with M35\_S (3.6 mg/mL in 50 mM Tris pH 7.4, 10% [vol/vol] glycerol, 250 mM NaCl, and 1 mM DTT) and incubated at 19°C, yielding a single crystal. Diffraction data of the flash-cooled crystal (cryoprotected with 12% [vol/vol] 2,3-butanediol) were collected at 100K on Beamline P11 of the PETRAIII Synchrotron (101) and reduced with autoPROC (102) and STARANISO (103) for scaling. Phasing was achieved by molecular replacement in PHASER (104) using PDB entry 5B1Q as a search model. Refinement involved alternating rounds of manual adjustments in COOT (105) and minimization with phenix.refine of the PHENIX software suite (106). Data collection and refinement statistics are listed in Table S2. The figures have been prepared with PyMOL (107).

**Size-exclusion chromatography combined with multiangle light scattering (SEC-MALS).** Experiments were performed on an Agilent 1260 Infinity II high-pressure liquid chromatography (HPLC) system equipped with a Superdex 200 Increase 10/300 column (Cytiva), a miniDAWN TREOS MALS detector, and an Optilab T-REX 505 refractometer (Wyatt Technology Corp., Santa Barbara, CA, USA). The column was equilibrated in 50 mM Tris, pH 7.4, 10% (vol/vol) glycerol, 250 mM NaCl, and 1 mM DTT. Then 100  $\mu$ g of protein was injected and SEC-separated on the system. The data were processed with the Astra software package (Wyatt Technology Corp.).

**Immunoblotting.** Standard Tris-glycine buffer chemistry (25 mM Tris-base, 192 mM glycine, pH 8.3) was applied for SDS, as well as native PAGE and wet transfer. SDS-PAGE used 10% polyacrylamide gels with 0.1% SDS that were run in Tris-glycine running buffer with 0.1% SDS, and the gels were blotted in Tris-glycine transfer buffer with 0.05% SDS and 20% methanol for 1 h at 350 mA.

For analysis of protein levels in luciferase assay samples, lysates of technical duplicates were pooled and centrifuged at 11,000 rpm for 10 min to spin out debris. Supernatant was mixed with 4 $\times$  SDS loading buffer (0.25 M Tris-HCl, pH 6.8, 40% glycerol, 8% SDS, 0.04% bromophenol blue, 10%  $\beta$ -mercaptoethanol in H<sub>2</sub>O) and boiled at 95°C for 10 min; then 10 or 15  $\mu$ L SDS sample was subjected to denaturing SDS-PAGE, followed by blotting on a nitrocellulose membrane (Amersham Protean 0.45  $\mu$ m NC, catalog no. 10600002, Cytiva) as above. Protein transfer for aliquots of the EMSA reactions run on EMSA gels was performed equally. For analysis of chromatin samples prepared for ChIP, aliquots of the prepared chromatin were subjected to SDS-PAGE and blotted on polyvinylidene difluoride (PVDF) membrane (Amersham Hybond P 0.2  $\mu$ m PVDF, catalog no. 10600021, Cytiva).

For coimmunoprecipitation of M35-HAHA with M35-V5/His, 800,000 HEK293T cells were seeded and transfected the next day with 4  $\mu$ g total DNA complexed with 15  $\mu$ L PEI diluted in a total volume of 300  $\mu$ L Opti-MEM. At 24 h post-transfection, the cells were lysed in radioimmunoprecipitation assay (RIPA) lysis buffer (20 mM Tris-HCl, pH 7.5, 100 mM NaCl, 1 mM EDTA, 1% Triton X-100, 0.1% SDS, 0.5% sodium deoxycholate) freshly supplemented with PI and incubated for 1 h at 4°C on a rotator. As the input control, 10% of the lysate was used, the remainder was precleared by coincubation with 40  $\mu$ L of PureProteome protein A/G magnetic beads (Merck Millipore, LSKMAGAG10) per sample and rotation for 1 h at 4°C. Supernatant was incubated for 1 h with 50  $\mu$ L anti-V5 tag MAb-Magnetic beads (catalog no. M167-11, MBL) blocked with 1 mg/mL BSA (catalog no. B9000S, New England Biolabs). The beads were washed seven times with lysis buffer, and bound protein was eluted by resuspending beads in 1 $\times$  SDS loading dye in lysis buffer and incubation for 10 min at 95°C. One-third of the IP samples and one-fourth of the 10% input samples was subjected to SDS-PAGE and immunoblot for analysis. For validation of M35-HAHA expression in stable cell line, 150,000 cells were washed with phosphate-buffered saline (PBS) and lysed in 100  $\mu$ L RIPA lysis buffer freshly supplemented with PI for 20 min, and 15  $\mu$ L were mixed with 4 $\times$  SDS loading buffer, incubated as above, and subjected to SDS-PAGE and immunoblotting.

For native PAGE (adapted from (108)), 150,000 HEK293T cells were seeded and transfected the next day with 405 ng total DNA complexed with 1.6  $\mu$ L FuGENE HD in 30  $\mu$ L Opti-MEM/well. The cells were lysed 20 h post-transfection in 75  $\mu$ L RIPA lysis buffer freshly supplemented with PI and incubated for 1 h at 4°C. Debris was pelleted by centrifugation, and sample supernatant was mixed with 2 $\times$  native loading buffer (125 mM Tris-HCl, pH 6.8, 60% glycerol, 0.2% bromophenol blue) and loaded on prerun native gels with 5% polyacrylamide stacking gel and 7.5% separating gel. Native gels were run at 4°C at 10 mA/gel using Tris-Glycine buffer with 0.2% sodium deoxycholate as cathode buffer and standard Tris-glycine buffer as anode buffer until the dye ran out. A size marker was omitted because the migration behavior of a protein in a native gel is influenced by its overall conformation (size and shape or compactness) and net charge (pI). Available markers can serve only as a very rough estimate of size and thus may be misleading; instead, whole membranes of native gels are shown. Separated samples were transferred in cold Tris-glycine buffer for 1 h at 350 mA on a nitrocellulose membrane; then the membrane was incubated for 15 min in fixation solution (40% ethanol, 7% acetic acid, 3% glycerol in H<sub>2</sub>O) at room temperature (RT) and washed three times in PBS before developing as described below.

After transfer or fixation, the membranes were blocked with 5% BSA in TBS with 0.1% Tween 20 (blocking solution), followed by incubation with primary and secondary HRP-coupled antibodies diluted in blocking solution. The membranes were developed with Lumi-Light (catalog no. 12015200001,

Roche) or Pierce ECL (catalog no. 32106, Thermo Fisher Scientific) Western Blotting substrates and imaged on a ChemoStar ECL Imager (INTAS).

**Multiple sequence alignment.** Members of the *Betaherpesvirinae* were selected based on the master species list of the International Committee on Taxonomy of Viruses (109) (accessed 24 February 2021 at <https://ictv.global/msl>, list version 2018b.v2), including the type species of every genus, at least one virus species per family of host organisms, all murine and human members relevant for our comparison, and the bat herpesvirus recently suggested to belong to this subfamily (110). Sequences of the U14 proteins of HHV6A, HHV6B, and HHV7 were taken from the same virus strains as in the previous comparison (60). Sequences were aligned online with Clustal Omega (111, 112) (accessed 24 April 2021 at <https://www.ebi.ac.uk/Tools/msa/clustalo/>). Based on the generated alignment, a phylogenetic tree was created and visualized using the software MEGA-X (113) (version 10.2.5). The alignment was illustrated in Jalview (114) (version 2.11.2.5) by highlighting amino acids by characters (color setting: Clustal X) and by conservation (shade). The percent amino acid (% aa) identities of the virus proteins compared to MCMV M35 were calculated based on the optimal global or local alignment in the online EMBOSS tools Needle and Water (112), respectively (both accessed 15 September 2022).

**Immunofluorescence assay.** To characterize M35 derivatives, respective expression constructs were transfected in HEK293T cells in a setup comparable to the luciferase reporter assays. For this, acid-washed glass coverslips (12 mm) were placed in the wells of a 24-well plate and coated by covering with poly-D-lysine solution (100 mg/mL in H<sub>2</sub>O) for 15 min. Coverslips were then washed three times with PBS, and 50,000 HEK293T cells were seeded in culture medium. The next day, 405 ng of the plasmid of interest was mixed with 1.6  $\mu$ L FuGENE HD in 30  $\mu$ L Opti-MEM/well, incubated for 15 min, and added dropwise to conditioned medium. The cells were permeabilized 24 h post-transfection by incubation in ice-cold methanol for 5 min at  $-20^{\circ}\text{C}$  followed by fixation with 4% paraformaldehyde (PFA) in PBS for 20 min at room temperature. The cells were washed three times with PBS, and then incubated in immunofluorescence (IF) assay blocking solution (10% FCS, 1% BSA in PBS) for 1 h at room temperature. Blocked coverslips were incubated with the primary antibody diluted in 1% BSA in PBS overnight at  $4^{\circ}\text{C}$ , followed by three washes with PBS and incubation with secondary antibody and Hoechst (1:500; catalog no. 33342, Thermo Fisher Scientific) in 1% BSA in PBS for 45 min at room temperature. Coverslips were mounted on glass slides with Prolong Gold (catalog no. P36930, Invitrogen, Thermo Fisher Scientific). Imaging was performed on a Nikon ECLIPSE Ti-E-inverted microscope equipped with a spinning disk device (Perkin Elmer Ultraview, Perkin Elmer, Hamburg, Germany), and images were processed using Volocity software (version 6.2.1, Perkin Elmer).

To characterize the stably expressing M35-HAHA compared to EV iMEFs; 150,000 iMEFs were seeded per well of a 12-well plate, allowed to settle for about 6 h, and processed in the wells as described above. Imaging was performed with an EVOS FL cell imaging system (Thermo Fisher Scientific).

**Chromatin immunoprecipitation (ChIP).** To prepare samples for ChIP,  $2.5 \times 10^6$  EV or M35-myc/His iMEFs were seeded in 10-cm dishes. After settling for 6 h, poly(I:C) was diluted in Opti-MEM and mixed with diluted Lipofectamine 2000 (1:1), incubated for 20 min at RT, mixed into fresh medium, and applied to the cells to obtain a final concentration of 10  $\mu\text{g}/\text{mL}$ . Control cells were mock-treated with Opti-MEM.

After 6 h, formaldehyde (16%, catalog no. 28908, Thermo Fisher Scientific) was added directly into the culture medium to yield 1% final concentration and incubated for 10 min at RT. To quench, the fixation medium was aspirated, replaced by cold PBS with 0.125 M glycine, and incubated for 5 min at RT. Then, the samples were processed on ice. The cells were washed three times for 10 min with cold PBS, collected by scraping, and pelleted at  $800 \times g$  for 5 min at  $4^{\circ}\text{C}$ . The supernatant was aspirated, and the pellets were snap-frozen. The pellets were resuspended in 900  $\mu\text{L}$  L1 buffer (50 mM Tris-HCl, pH 8.0, 2 mM EDTA, 0.1% Nonidet P-40 substitute [catalog no. 74385, Fluka], 10% glycerol) freshly supplemented with PI and PhI and incubated for 5 min on ice to lyse the cell membrane. The nuclei were pelleted by centrifugation at  $4^{\circ}\text{C}$  for 5 min at  $3,000 \times g$  and resuspended in 300  $\mu\text{L}$  L2 buffer (50 mM Tris-HCl, pH 8.0, 5 mM EDTA, 1% SDS) freshly supplemented with PI and PhI. Chromatin was sonicated in 1.5-mL TPX microtubes (catalog no. C30010010, Diagenode, Seraing, Belgium) for 20 cycles (30 s on/30 s off, high-intensity) in a Bioruptor NextGen (Diagenode). Chromatin and DNA samples were processed in DNA LoBind tubes from here on (Eppendorf catalog no. 2023-04-28; catalog no. 2023-01-28). For control, aliquots of the chromatin (5%) were subjected to SDS-PAGE and immunoblotting as described above.

Per ChIP sample, 10  $\mu\text{g}$  of chromatin were diluted with 9 volumes of ChIP dilution buffer (50 mM Tris-HCl, pH 8.0, 5 mM EDTA, 200 mM NaCl, 0.5% Nonidet P-40 substitute), and 1% was removed and purified as input. 50  $\mu\text{L}$  Dynabeads protein G magnetic beads (catalog no. 10007D, Invitrogen, Thermo Fisher Scientific) were coupled with 5  $\mu\text{g}$  of the indicated antibody by incubation for 10 min at RT, added to the chromatin, and incubated overnight rotating at  $4^{\circ}\text{C}$ . After 16 h, the samples were washed in 1 mL of the following buffers freshly supplemented with PI and PhI for each 5 min rotating at  $4^{\circ}\text{C}$ : once in ChIP dilution buffer, three times in high-salt washing buffer (20 mM Tris-HCl, pH 8.0, 0.1% SDS, 2 mM EDTA, 1% Nonidet P-40 substitute, 500 mM NaCl), once in LiCl washing buffer (10 mM Tris-HCl, pH 8.0, 0.25 M LiCl, 1 mM EDTA, 1% sodium deoxycholate, 1% Nonidet P-40 substitute), and twice in TE buffer (10 mM Tris-HCl, pH 8.0, 1 mM EDTA). Lastly, supernatant was discarded, and the beads were resuspended in 100  $\mu\text{L}$  elution buffer (1% SDS, 0.1 M NaHCO<sub>3</sub>) and incubated for 15 min shaking at  $65^{\circ}\text{C}$ . Supernatant was collected, and the beads were eluted with another 100  $\mu\text{L}$  elution buffer. The eluates were combined and incubated overnight at  $65^{\circ}\text{C}$ . Input samples were filled up to 200  $\mu\text{L}$  with elution buffer and processed alongside ChIP samples. The next day, 4  $\mu\text{L}$  of 10 mg/mL RNase A (DNeasy blood and tissue kit, catalog no. 69504, Qiagen, Hilden, Germany) was added to each sample and incubated at  $37^{\circ}\text{C}$  for 2 h. Then 2  $\mu\text{L}$  of 20 mg/mL proteinase K (catalog no. 3115879001, Roche) was added and again incubated at  $55^{\circ}\text{C}$  for 2 h. DNA was purified using the NucleoSpin gel and PCR clean-up

(catalog no. 74609.250, Macherey-Nagel, Düren, Germany) kit with NTB binding buffer (catalog no. 740595.150, Macherey-Nagel) according to the manufacturer's instructions and eluted in 30  $\mu$ L.

For analysis, 1  $\mu$ L per input or ChIP sample was used in a qPCR using the GoTaq Mastermix (catalog no. M7133, Promega) and primer pairs for the amplification of the *Irfb1* promoter region (ChIP\_IFNb1\_fwd 5'-GCCAGGAGCTTGAATAAAATG, and ChIP\_IFNb1\_rev 5'-GATGGCTCTTCTGCCTCAG) or the *Irf6* promoter region upstream of the predicted IRF3-binding site (ChIP\_Ctrl\_IL-6\_fwd 5'-CTAGTACTCCCTGCAGCC, and ChIP\_Ctrl\_IL-6\_rev 5'-ACCTGCAAACCTGGCAAATCG) as control. Enrichment was calculated by the percent input method, as follows:

$$\% \text{ input} = 2^{-(C_q(\text{input}) - \text{Log}_2(\text{dilution factor}) - C_q(\text{ChIP sample}))} \times 100.$$

**Stimulation.** The time point for analysis of upregulated transcripts after IFN- $\beta$  treatment was determined in a small kinetic experiment. A total of 350,000 WT MEFs cells were seeded per well of a 6-well plate in the evening and stimulated the next morning by diluting IFN- $\beta$  in Opti-MEM and mixing the predilution into the conditioned medium. A parallel sample was transfected with 5  $\mu$ g/ $\mu$ L of ISD with Lipofectamine 2000 as described above; an untreated sample served as the control. IFN- $\beta$ -treated cells were harvested after 1, 2, 3, or 4 h, ISD-treated or untreated cells were harvested after 4 h, and the samples were analyzed by RT-qPCR.

To assess induction of *Irfna4* expression in WT, IRF3<sup>-/-</sup>, or IFNAR1<sup>-/-</sup> MEFs, 100,000 cells were seeded per well of a 12-well plate in the evening and stimulated the next day for 3 h with 100 U/mL of IFN- $\beta$  or for 4 h by transfection of 5  $\mu$ g/mL ISD with Lipofectamine 2000 as described above. Untreated and mock-transfected cells served as control, respectively. The samples were analyzed by RT-qPCR.

For validation of the M35-mediated phenotype in M35-HAHA compared to EV iMEFs, 80,000 cells were seeded per well of a 12-well plate in the evening and stimulated the next day by transfection of 10  $\mu$ g/mL of poly(I:C) with Lipofectamine 2000 as described above. The samples were harvested after 4 h and analyzed by RT-qPCR.

The time points for analysis of transcripts regulated in response to (Alexa Fluor 488-labeled) ISD transfection were determined in a small kinetic experiment. A total of 450,000 EV iMEFs were seeded per well of a 6-well plate in the evening and stimulated the next morning by transfection with 5  $\mu$ g/mL Alexa Fluor 488-labeled ISD. The samples were harvested after 1, 2, 3, 4, 5, 6, or 8 h and analyzed by RT-qPCR. Untreated cells and mock-transfected cells harvested after 4 h served as control.

**Infection of iBMDMs.** To determine the effect of M35 on IRF3-dependent gene expression during MCMV infection, 800,000 iBMDMs were seeded in wells of a 6-well plate the day prior to the experiment and pretreated by replacing conditioned medium with fresh medium containing 1  $\mu$ M ruxolitinib. After 20 min, the cells were infected on ice by replacing the cell culture supernatant with diluted MCMV REV or M35stop in fresh medium supplemented with 1  $\mu$ M ruxolitinib to obtain a multiplicity of infection (MOI) of 0.1. Plates with cells were centrifuged at 805  $\times$  g and 4°C for 30 min to enhance infection before shifting samples to 37°C with 5% CO<sub>2</sub>. The moment when the infected cells were shifted to 37°C incubation was defined as time point 0. After 30 min at 37°C, the medium was replaced with fresh medium supplemented with 1  $\mu$ M ruxolitinib. Samples were harvested after 4 h for analysis by RT-qPCR.

To control the activity of ruxolitinib, an additional set of iBMDMs was pretreated with DMSO or 1  $\mu$ M ruxolitinib for 20 min and then treated with 100 U/mL of murine IFN- $\beta$  and ruxolitinib, treated with ruxolitinib alone, or mock-treated with DMSO. The cells were harvested after 3 h and analyzed by RT-qPCR.

**Quantitative PCR with reverse transcription (RT-qPCR).** For simultaneous analysis of multiple transcripts in primary MEF or iBMDM, cDNA was generated and then applied to SYBR green-based qPCR. RNA was extracted using the innuPREP RNA minikit 2.0 (catalog no. 845-KS-2040250, Analytik Jena, Jena, Germany), genomic DNA was removed using the iScript gDNA Clear cDNA synthesis kit (catalog no. 1725035, Bio-Rad Laboratories, Feldkirchen, Germany), and cDNA was synthesized with the iScript cDNA Synthesis kit (catalog no. 1708891, Bio-Rad Laboratories) according to the manufacturers' instructions. Quantification of transcripts was performed using the GoTaq qPCR Master Mix (catalog no. A6002, Promega) on a LightCycler 96 instrument (Roche). The qPCR primers were as follows: *Rpl8* (*Rpl8*\_for: 5'-CAACAGAGCCGTTGTGGT-3', *Rpl8*\_rev: 5'-CAGCCTTAAAGATAGGCTGTCA-3'), *Irfb1* (*IFNb*\_for: 5'-CTGGCTCCATCATGAACAA-3', *IFNb*\_rev: 5'-AGAGGGCTGTGGTGAGAA-3'), *Irfna4* (*IFNa4*\_for: 5'-TCAAGCCATCCTGTGTAA-3', *IFNa4*\_rev: 5'-GTCTTTTGATGTGAAGAGGTTCAA-3'), *Isg15* (*mISG15*\_fwd 5'-AGTCGACCCAGTCTCTGACTCT-3', *mISG15*\_rev 5'-CCCCAGCATCTTCACCTTA-3'), *Irfi3* (*mIrfi3*\_fwd 5'-TGGACTGAGATTCTGAAGTGC-3', *mIrfi3*\_rev 5'-AGAGATCCCGGTTGACCTC-3'), *Rsdad2* (*mRsdad2*\_fwd 5'-GGAAGGTTTTCCAGTGCCTCCT-3', *mRsdad2*\_rev 5'-ACAGGACACCTCTTGTGACGC-3'), *Stat1* (*mStat1*\_for 5'-GCCTCTCATTGTACCCGAAGAAC-3', *mStat1*\_rev 5'-TGGCTGACGTTGGAGATACCA-3'), *Nfkbia* (*mNfkbia*\_for 5'-GCCAGGAATTGCTGAGGCACTT-3', *mNfkbia*\_rev 5'-GTCTGCGTCAAGACTGTACAC-3'), and *Tgfb1* (*mTgfb1*\_for 5'-TGATACGCCTGAGTGGCTGTCT-3', *mTgfb1*\_rev 5'-CAACAGCAGTGAGCGCTGAA-3').

To determine induction of *Irfna4* expression in primary MEF, RNA was prepared using the innuPREP RNA minikit 2.0, followed by removal of genomic DNA using the DNA-free kit (Ambion, Thermo Fisher Scientific). cDNA synthesis and quantification of transcripts was carried out using the EXPRESS one-step Superscript RT-qPCR kit (catalog no. 11781200, Invitrogen, Thermo Fisher Scientific) with 100 ng RNA per sample on a LightCycler 96 instrument (Roche). PCR primers for *Rpl8* and *Irfna4* were used as given above together with the universal probe library probes (UPL, Roche) 5 and 3, respectively.

To determine the induction of *Irfb1* expression in EV and M35-HAHA iMEFs, the samples were lysed in RLT buffer supplemented with  $\beta$ -mercaptoethanol, and RNA was purified using the RNeasy minikit (catalog no. 7410, Qiagen) with on-column DNase treatment (catalog no. 79254, Qiagen) according to the manufacturer's instructions. cDNA synthesis and quantification of transcripts was carried out using

the EXPRESS one-step Superscript RT-qPCR kit as described above, using the *Rpl8* primer pair with probe 5 and the *Ifnb1* primer pair with probe 18. Relative fold inductions were calculated using the  $2^{-\Delta\Delta Ct}$  method.

**Statistical analysis.** For luciferase reporter assays, RT-qPCR, and ChIP-qPCR, differences between two groups were evaluated by Student's *t* test (unpaired, two-tailed) using GraphPad Prism (version 5.0, GraphPad Software, San Diego, CA). *P* values < 0.05 were considered statistically significant: \*, *P* < 0.05; \*\*, *P* < 0.01; \*\*\*, *P* < 0.001; \*\*\*\*, *P* < 0.0001. Significance (*P*) of overlaps between two given groups of regulated gene products was determined by one-sided Fisher's exact test, alternative = greater.

**SLAM-seq.** To determine the amount of 4-thiouridine (4sU; catalog no. NT06186, Biosynth Carbosynth) for efficient labeling of nascent transcripts, 350,000 primary WT MEFs were seeded per well of a 6-well plate a day prior to the experiment. The cells were incubated with 100, 200, 400, or 800  $\mu$ M 4sU diluted into the conditioned medium and harvested after 2 h. Untreated cells served as control. The samples were harvested at indicated time points by lysis in 750  $\mu$ L TRIzol (catalog no. 5596026, Invitrogen, Thermo Fisher Scientific) per well for 2 min. RNA of half of the sample volume was purified using the DirectZOL Microprep kit (catalog no. 2060, Zymo Research) according to the manufacturer's instructions, including the on-column DNase digestion. For SLAM conversion, 90  $\mu$ L of 20 mM iodoacetamide (Pierce IAA, catalog no. A39271, Thermo Fisher Scientific) solution in DMSO was mixed with 90  $\mu$ L of RNA in 1 $\times$  PBS and incubated at 50°C and 1,000 rpm for 30 min in the dark. The reaction was stopped by mixing with 20  $\mu$ L of 1 M dithiothreitol (DTT). Converted RNA was purified using the RNA Clean and Concentrator-5 (catalog no. R1015, Zymo Research).

Quality and integrity of total RNA was controlled using a 2100 Bioanalyzer instrument with an RNA 6000 nano chip (catalog no. 5067-1511, Agilent Technologies, Santa Clara, CA, USA). The RNA sequencing library was generated from 300 ng total RNA using the TruSeq Stranded mRNA library prep kit (catalog no. 20020595, Illumina, San Diego, CA, USA) with oligo(dT) beads for capture of poly(A)-mRNA according to the manufacturer's protocol. Quality and integrity of the libraries was controlled using a Bioanalyzer DNA 1000 chip (catalog no. 5067-1504, Agilent). The libraries were treated with Illumina Free Adapter Blocking Reagent (catalog no. 20024145) and sequenced on an Illumina NextSeq 500 system using the NextSeq 500/550 Mid Output kit v2.5 (catalog no. 20024904, Illumina; 150 cycles, paired-end run 2  $\times$  75 bp) with an average of  $1 \times 10^7$  reads/RNA sample.

For characterization of IRF3- and type I IFN-dependent genes, 300,000 primary WT, IRF3<sup>-/-</sup>, or IFNAR1<sup>-/-</sup> MEFs were seeded per well of a 6-well plate a day prior to harvest to reach 80% confluence. To stimulate PRR signaling, ISD was mixed with an equal volume of Lipofectamine 2000 in 100  $\mu$ L Opti-MEM, incubated for 20 min, and added to the conditioned medium to yield 5  $\mu$ g/mL final concentration of ISD. For control, the cells were mock-treated with the same amount of Lipofectamine 2000 diluted in Opti-MEM. Type I IFN signaling was stimulated in a parallel set of samples by prediluting murine IFN- $\beta$  in Opti-MEM and adding the mix into the conditioned medium to reach a final concentration of 100 U/mL. Untreated samples served as controls. All samples were prepared in quadruplicate. At 2 h before lysis, 200  $\mu$ M 4sU was added to the culture medium to label nascent RNAs. A set of untreated cells without 4sU treatment was prepared to control the incorporation rate. Samples were harvested at indicated time points by lysis in 750  $\mu$ L TRIzol and processed as described above.

The quality and integrity of total RNA was controlled on a 5200 fragment analyzer system (Agilent Technologies, Santa Clara, CA, USA). The RNA sequencing library was generated from 200 ng total RNA using Dynabeads mRNA DIRECT micro purification kit (Thermo Fisher Scientific) for mRNA purification followed by NEBNext Ultra II Directional RNA library prep kit (New England Biolabs) according to the manufacturer's protocols. The libraries were treated with Illumina free adapter blocking reagent (Illumina, San Diego, CA, USA) and were sequenced on Illumina NovaSeq 6000 using a NovaSeq 6000 S1 reagent kit (150 cycles, paired-end run 2  $\times$  150 bp) with an average of  $3 \times 10^7$  reads/RNA sample.

Samples subjected to total transcriptome analysis were generated and processed similar to SLAM-seq samples with minor changes: 450,000 EV or M35-HAHA iMEFs were seeded per sample, stimulation was conducted by transfection of 5  $\mu$ g/mL of Alexa Fluor 488-coupled ISD, and 200  $\mu$ M 4sU was added for 90 min prior to lysis. RNA was purified using the DirectZOL miniprep kit (catalog no. R2050, Zymo Research, Freiburg, Germany), and 2  $\mu$ g RNA/sample was used for SLAM conversion. Converted RNA was purified using the RNeasy micro kit (catalog no. 74004, Qiagen) and measured using a Qubit fluorometer (Thermo Fisher Scientific) with the Qubit RNA HS assay kit (catalog no. Q32852, Thermo Fisher Scientific). The RNA sequencing library was generated from 100 ng RNA using the NEBNext Ultra II Directional RNA library prep kit for Illumina (catalog no. 577605 and catalog no. 577655, New England Biolabs, Frankfurt am Main, Germany) with the NEBNext Poly(A) mRNA magnetic isolation module (catalog no. E7490, New England Biolabs) and SPRIselect beads (catalog no. B23319, Beckman Coulter) according to the manufacturer's protocols. The quality and integrity of the libraries were controlled on a 2100 bioanalyzer instrument (Agilent) using a DNA chip (catalog no. 5067, Agilent). The libraries were treated with Illumina free adapter blocking reagent (catalog no. 20024145) and sequenced on an Illumina NovaSeq 6000 system using the NovaSeq 6000 S4 individual lane loading reagent kit (catalog no. 20028313, Illumina; 150 cycles, paired-end run 1  $\times$  111 bp) with an average of  $2 \times 10^7$  reads/sample. However, the conversion efficiency was too low to quantify newly synthesized transcripts, while the overall integrity of transcripts was not influenced; therefore, the total transcripts were processed to evaluate this experiment.

**Data evaluation of SLAM-seq experiments.** Reads from all three data sets (4sU titration, WT versus IRF3<sup>-/-</sup> versus IFNAR1<sup>-/-</sup> MEFs, and M35 versus EV iMEFs) were processed by the same pipeline with the same parameters. First, reads were mapped against murine rRNA (less than 3% of reads in all cases) and common mycoplasma contaminations (less than 0.1% of reads in all cases) using bowtie2 version 2.3.0 (115) with standard parameters. All remaining reads were mapped to the murine genome (Ensembl version 90) using STAR version 2.5.3a (116) using parameters `-outFilterMismatchNmax 20 -outFilterScoreMinOverRead 0.4 -`



outFilterMatchNminOverLread 0.4 –alignEndsType Extend5pOfReads12 –outSAMattributes nM MD NH (uniquely mappable reads > 85% in all cases). Mapped reads from each of the three experiments were then further processed separately using GRAND-SLAM 2.0.7 (117) with parameters –trim5p 15 –modelall. The output tables of GRAND-SLAM were then further analyzed using our grandR package 0.2.1 (118). Toxicity plots for the 4sU titration experiments were generated using the PlotToxicityTest function. Genes for the WT versus IRF3<sup>-/-</sup> versus IFNAR1<sup>-/-</sup> MEFs (E1) and M35 versus EV iMEFs (E2) experiments were filtered such that at least 100 reads were present on average across replicates for at least one condition of E1 and one condition of E2. Differential gene expression was computed using the Wald test implemented in DESeq2 (119) with Benjamini-Hochberg multiple testing correction and the lfc package (120).

The statistical tests and Spearman correlation were calculated with R. The venn diagrams were created using the R VennDiagram package. The heat maps were created using the R pheatmap package, and clustering was performed according to Euclidean distances with Ward's clustering criterion.

**Functional enrichment analysis.** The analysis for enriched biological processes based on Gene Ontology (GO) terms or for regulatory DNA motifs based on the transcription factor database TRANSFAC (121) was performed using the online tool g:GOST of the g:Profiler web server (<https://biit.cs.ut.ee/gprofiler/gost>, version e107\_eg54\_p17\_bf42210, accessed 25.01.2023 for GO biological processes; version e107\_eg54\_p17\_bf42210, accessed 20.02.2023 for transcription factors) (122) using our own background data. The *P* values were corrected for multiple testing using the method by Benjamini and Hochberg for controlling the FDR. Terms with FDR < 0.001 were considered statistically significant.

**Data availability.** The SLAM-seq data sets have been deposited in the NCBI GEO database, with the accession numbers [GSE224855](https://www.ncbi.nlm.nih.gov/geo/query/acc.cgi?acc=GSE224855) (classification of IRF3-dependent versus IFNAR1-responsive gene induction in murine fibroblasts) and [GSE224852](https://www.ncbi.nlm.nih.gov/geo/query/acc.cgi?acc=GSE224852) (effect of MCMV M35 on global gene expression during PRR signaling in murine fibroblasts).

## SUPPLEMENTAL MATERIAL

Supplemental material is available online only.

**SUPPLEMENTAL FILE 1**, PDF file, 0.4 MB.

**SUPPLEMENTAL FILE 2**, DOCX file, 3.7 MB.

## ACKNOWLEDGMENTS

We thank Markus Stempel, Friedemann Weber, and Baca Chan for fruitful discussions and Sara Becker, Niels Lemmermann, and Kai Kropp for insightful comments. We also thank Daniela Gebauer, Maria Ebel, Christine Standfuß-Gabisch, Lennart Krause, and Susanne Zock-Emmenthal for excellent technical assistance. Special thanks go to the staff of Beamline P11 at the PETRAIII synchrotron (DESY campus, Hamburg, Germany).

This project was funded by the Deutsche Forschungsgemeinschaft in the framework of Research Unit FOR5200 DEEP-DV (443644894) through projects BR 3432/7-1 (H.S., M.M.B.), FR 2938/11-1 (C.C.F.), ER 927/4-1 (F.E.), DO 1275/12-1 (T.H., L.D.), GR 3318/5-1 (T.G., A.G.), LA 2941/18-1 (E.W., M.L.), and the Helmholtz Association (W2/W3-090) (V.G.M., M.M.B.), and was supported by the Helmholtz Protein Sample Production Facility.

The funders had no role in the design of the study; in the collection, analysis, or interpretation of data; in the writing of the manuscript; or in the decision to publish the results.

Conceptualization, H.S., V.G.M., S.S., E.W., F.E., W.B., M.M.B.; Data Curation, H.S., V.G.M., S.S., E.W., M.v.H., J.v.d.H., W.B., C.C.F., F.E., M.M.B.; Formal analysis, H.S., S.S., E.W., M.v.H., T.G., C.C.F., F.E.; Funding acquisition, L.J., W.B., M.L., A.G., L.D., C.C.F., F.E., M.M.B.; Investigation, H.S., V.G.M., S.S., E.W., T.H., T.G., K.B., M.v.H., J.v.d.H.; Methodology, H.S., V.G.M., S.S., E.W., T.G., K.B., J.v.d.H., L.J., W.B., F.E., M.M.B.; Project administration, M.M.B.; Resources, L.J., J.v.d.H., M.L., L.D., A.G., W.B., C.C.F., F.E., M.M.B.; Software, S.S., F.E., C.C.F., T.G.; Supervision, H.S., M.M.B.; Validation, H.S., V.G.M., F.E.; Visualization, H.S., S.S., C.C.F., F.E.; Writing – original draft, H.S., V.G.M., S.S., J.v.d.H., C.C.F., F.E.; Writing – reviewing and editing, H.S., V.G.M., S.S., E.W., T.H., T.G., A.G., L.D., M.L., M.v.H., L.J., K.B., W.B., C.C.F., F.E., M.M.B.

## REFERENCES

1. Isaacs A, Lindenmann J, Andrewes CH. 1997. Virus interference. I. The interferon. *Proc R Soc Lond B Biol Sci* 147:258–267.
2. Stark GR, Kerr IM, Williams BRG, Silverman RH, Schreiber RD. 1998. How cells respond to interferons. *Annu Rev Biochem* 67:227–264. <https://doi.org/10.1146/annurev.biochem.67.1.227>.
3. Wang BX, Fish EN. 2019. Global virus outbreaks: interferons as 1st responders. *Semin Immunol* 43:101300. <https://doi.org/10.1016/j.smim.2019.101300>.
4. Guy C, Bowie AG. 2022. Recent insights into innate immune nucleic acid sensing during viral infection. *Curr Opin Immunol* 78:102250. <https://doi.org/10.1016/j.coi.2022.102250>.

5. Shaulian E, Karin M. 2002. AP-1 as a regulator of cell life and death. *Nat Cell Biol* 4:E131–E136. <https://doi.org/10.1038/ncb0502-e131>.
6. Liu T, Zhang L, Joo D, Sun S-C. 2017. NF- $\kappa$ B signaling in inflammation. *Signal Transduct Target Ther* 2:17023–17023. <https://doi.org/10.1038/sigtrans.2017.23>.
7. Génin P, Lin R, Hiscott J, Civas A. 2009. Differential regulation of human interferon A gene expression by interferon regulatory factors 3 and 7. *Mol Cell Biol* 29:3435–3450. <https://doi.org/10.1128/MCB.01805-08>.
8. Sato M, Suemori H, Hata N, Asagiri M, Ogasawara K, Nakao K, Nakaya T, Katsuki M, Noguchi S, Tanaka N, Taniguchi T. 2000. Distinct and essential roles of transcription factors IRF-3 and IRF-7 in response to viruses for IFN- $\alpha/\beta$  gene induction. *Immunity* 13:539–548. [https://doi.org/10.1016/S1074-7613\(00\)00053-4](https://doi.org/10.1016/S1074-7613(00)00053-4).
9. Nakaya T, Sato M, Hata N, Asagiri M, Suemori H, Noguchi S, Tanaka N, Taniguchi T. 2001. Gene induction pathways mediated by distinct IRFs during viral infection. *Biochem Biophys Res Commun* 283:1150–1156. <https://doi.org/10.1006/bbrc.2001.4913>.
10. Du W, Maniatis T. 1992. An ATF/CREB binding site is required for virus induction of the human interferon beta gene [corrected]. *Proc Natl Acad Sci U S A* 89:2150–2154. <https://doi.org/10.1073/pnas.89.6.2150>.
11. Yoneyama M, Suhara W, Fukuhara Y, Fukuda M, Nishida E, Fujita T. 1998. Direct triggering of the type I interferon system by virus infection: activation of a transcription factor complex containing IRF-3 and CBP/p300. *EMBO J* 17:1087–1095. <https://doi.org/10.1093/emboj/17.4.1087>.
12. Thanos D, Maniatis T. 1992. The high mobility group protein HMGI(Y) is required for NF- $\kappa$ B-dependent virus induction of the human IFN- $\beta$  gene. *Cell* 71:777–789. [https://doi.org/10.1016/0092-8674\(92\)90554-p](https://doi.org/10.1016/0092-8674(92)90554-p).
13. Sato M, Tanaka N, Hata N, Oda E, Taniguchi T. 1998. Involvement of the IRF family transcription factor IRF-3 in virus-induced activation of the IFN- $\beta$  gene. *FEBS Lett* 425:112–116. [https://doi.org/10.1016/S0014-5793\(98\)00210-5](https://doi.org/10.1016/S0014-5793(98)00210-5).
14. Schoggins JW. 2019. Interferon-stimulated genes: what do they all do? *Annu Rev Virol* 6:567–584. <https://doi.org/10.1146/annurev-virology-092818-015756>.
15. Michalska A, Blaszczyk K, Wesoly J, Bluyssen HAR. 2018. A positive feedback amplifier circuit that regulates interferon (IFN)-stimulated gene expression and controls type I and type II IFN responses. *Front Immunol* 9:1135. <https://doi.org/10.3389/fimmu.2018.01135>.
16. Wathlet MG, Clauss IM, Nols CB, Content J, Huez GA. 1987. New inducers revealed by the promoter sequence analysis of two interferon-activated human genes. *Eur J Biochem* 169:313–321. <https://doi.org/10.1111/j.1432-1033.1987.tb13614.x>.
17. Grandvaux N, Servant MJ, tenOever B, Sen GC, Balachandran S, Barber GN, Lin R, Hiscott J. 2002. Transcriptional profiling of interferon regulatory factor 3 target genes: direct involvement in the regulation of interferon-stimulated genes. *J Virol* 76:5532–5539. <https://doi.org/10.1128/jvi.76.11.5532-5539.2002>.
18. Browne EP, Wing B, Coleman D, Shenk T. 2001. Altered cellular mRNA levels in human cytomegalovirus-infected fibroblasts: viral block to the accumulation of antiviral mRNAs. *J Virol* 75:12319–12330. <https://doi.org/10.1128/JVI.75.24.12319-12330.2001>.
19. DeFilippis VR, Robinson B, Keck TM, Hansen SG, Nelson JA, Früh KJ. 2006. Interferon regulatory factor 3 is necessary for induction of antiviral genes during human cytomegalovirus infection. *J Virol* 80:1032–1037. <https://doi.org/10.1128/JVI.80.2.1032-1037.2006>.
20. Andersen J, VanScoy S, Cheng T-F, Gomez D, Reich NC. 2008. IRF-3-dependent and augmented target genes during viral infection. *Genes Immun* 9:168–175. <https://doi.org/10.1038/sj.gene.6364449>.
21. Ashley CL, Abendroth A, McSharry BP, Slobedman B. 2019. Interferon-independent upregulation of interferon-stimulated genes during human cytomegalovirus infection is dependent on IRF3 expression. *Viruses* 11:246. <https://doi.org/10.3390/v11030246>.
22. Ashley CL, Abendroth A, McSharry BP, Slobedman B. 2019. Interferon-independent innate responses to cytomegalovirus. *Front Immunol* 10:2751. <https://doi.org/10.3389/fimmu.2019.02751>.
23. Fensterl V, Sen GC. 2015. Interferon-induced Ifit proteins: their role in viral pathogenesis. *J Virol* 89:2462–2468. <https://doi.org/10.1128/JVI.02744-14>.
24. Schneider WM, Chevillotte MD, Rice CM. 2014. Interferon-stimulated genes: a complex web of host defenses. *Annu Rev Immunol* 32:513–545. <https://doi.org/10.1146/annurev-immunol-032713-120231>.
25. Au WC, Moore PA, Lowther W, Juang YT, Pitha PM. 1995. Identification of a member of the interferon regulatory factor family that binds to the interferon-stimulated response element and activates expression of interferon-induced genes. *Proc Natl Acad Sci U S A* 92:11657–11661. <https://doi.org/10.1073/pnas.92.25.11657>.
26. Honda K, Yanai H, Negishi H, Asagiri M, Sato M, Mizutani T, Shimada N, Ohba Y, Takaoka A, Yoshida N, Taniguchi T. 2005. IRF-7 is the master regulator of type-I interferon-dependent immune responses. *Nature* 434:772–777. <https://doi.org/10.1038/nature03464>.
27. Sato M, Hata N, Asagiri M, Nakaya T, Taniguchi T, Tanaka N. 1998. Positive feedback regulation of type I IFN genes by the IFN-inducible transcription factor IRF-7. *FEBS Lett* 441:106–110. [https://doi.org/10.1016/S0014-5793\(98\)01514-2](https://doi.org/10.1016/S0014-5793(98)01514-2).
28. Marié I, Durbin JE, Levy DE. 1998. Differential viral induction of distinct interferon- $\alpha$  genes by positive feedback through interferon regulatory factor-7. *EMBO J* 17:6660–6669. <https://doi.org/10.1093/emboj/17.22.6660>.
29. Thanos D, Maniatis T. 1995. Virus induction of human IFN beta gene expression requires the assembly of an enhancosome. *Cell* 83:1091–1100. [https://doi.org/10.1016/0092-8674\(95\)90136-1](https://doi.org/10.1016/0092-8674(95)90136-1).
30. Schwanke H, Stempel M, Brinkmann MM. 2020. Of keeping and tipping the balance: host regulation and viral modulation of IRF3-dependent IFN $\beta$  expression. *Viruses* 12:733. <https://doi.org/10.3390/v12070733>.
31. Tanaka N, Kawakami T, Taniguchi T. 1993. Recognition DNA sequences of interferon regulatory factor 1 (IRF-1) and IRF-2, regulators of cell growth and the interferon system. *Mol Cell Biol* 13:4531–4538. <https://doi.org/10.1128/mcb.13.8.4531-4538.1993>.
32. Panne D, Maniatis T, Harrison SC. 2004. Crystal structure of ATF-2/c-Jun and IRF-3 bound to the interferon-beta enhancer. *EMBO J* 23:4384–4393. <https://doi.org/10.1038/sj.emboj.7600453>.
33. Escalante CR, Nistal-Villán E, Shen L, García-Sastre A, Aggarwal AK. 2007. Structure of IRF-3 bound to the PRDIII-I regulatory element of the human interferon- $\beta$  enhancer. *Mol Cell* 26:703–716. <https://doi.org/10.1016/j.molcel.2007.04.022>.
34. Panne D, Maniatis T, Harrison SC. 2007. An atomic model of the interferon-beta enhancosome. *Cell* 129:1111–1123. <https://doi.org/10.1016/j.cell.2007.05.019>.
35. Chaturanga K, Weerawardhana A, Dodantenna N, Lee J-S. 2021. Regulation of antiviral innate immune signaling and viral evasion following viral genome sensing. *Exp Mol Med* 53:1647–1668. <https://doi.org/10.1038/s12276-021-00691-y>.
36. Rojas JM, Alejo A, Martín V, Sevilla N. 2021. Viral pathogen-induced mechanisms to antagonize mammalian interferon (IFN) signaling pathway. *Cell Mol Life Sci* 78:1423–1444. <https://doi.org/10.1007/s00018-020-03671-z>.
37. Zuhair M, Smit GSA, Wallis G, Jabbar F, Smith C, Devleeschauwer B, Griffiths P. 2019. Estimation of the worldwide seroprevalence of cytomegalovirus: a systematic review and meta-analysis. *Rev Med Virol* 29:e2034. <https://doi.org/10.1002/rmv.2034>.
38. Adler B, Sinzger C. 2009. Endothelial cells in human cytomegalovirus infection: one host cell out of many or a crucial target for virus spread? *Thromb Haemost* 102:1057–1063. <https://doi.org/10.1160/TH09-04-0213>.
39. Gerna G, Kabanova A, Lilleri D. 2019. Human cytomegalovirus cell tropism and host cell receptors. *Vaccines* 7:70. <https://doi.org/10.3390/vaccines7030070>.
40. Stinski MF, Thomsen DR, Rodriguez JE. 1982. Synthesis of human cytomegalovirus-specified RNA and protein in interferon-treated cells at early times after infection. *J Gen Virol* 60:261–270. <https://doi.org/10.1099/0022-1317-60-2-261>.
41. Torigoe S, Campbell DE, Starr SE. 1997. Cytokines released by human peripheral blood mononuclear cells inhibit the production of early and late cytomegalovirus proteins. *Microbiol Immunol* 41:403–413. <https://doi.org/10.1111/j.1348-0421.1997.tb01871.x>.
42. McSharry BP, Forbes SK, Avdic S, Randall RE, Wilkinson GWG, Abendroth A, Slobedman B. 2015. Abrogation of the interferon response promotes more efficient human cytomegalovirus replication. *J Virol* 89:1479–1483. <https://doi.org/10.1128/JVI.02988-14>.
43. Le VTK, Trilling M, Zimmermann A, Hengel H. 2008. Mouse cytomegalovirus inhibits beta interferon (IFN-beta) gene expression and controls activation pathways of the IFN-beta enhancosome. *J Gen Virol* 89:1131–1141. <https://doi.org/10.1099/vir.0.83538-0>.
44. Loewendorf A, Benedict CA. 2010. Modulation of host innate and adaptive immune defenses by cytomegalovirus: timing is everything. *J Intern Med* 267:483–501. <https://doi.org/10.1111/j.1365-2796.2010.02220.x>.
45. Dell'Oste V, Biolatti M, Galitska G, Griffante G, Gugliesi F, Pasquero S, Zingoni A, Cerboni C, De Andrea M. 2020. Tuning the orchestra: HCMV vs. innate immunity. *Front Microbiol* 11:661. <https://doi.org/10.3389/fmicb.2020.00661>.

46. Dadwal SS, Papanicolaou G, Boeckh M. 2023. How I prevent viral reactivation in high-risk patients. *Blood* 141:2052–2074. <https://doi.org/10.1182/blood.2021014676>.
47. Azevedo LS, Pierrotti LC, Abdala E, Costa SF, Strabelli TMV, Campos SV, Ramos JF, Latif AZA, Litvinov N, Maluf NZ, Filho HHC, Pannuti CS, Lopes MH, dos Santos VA, da Cruz Gouveia Linardi C, Yasuda MAS, de Sousa Marques HH. 2015. Cytomegalovirus infection in transplant recipients. *Clinics* 70:515–523. [https://doi.org/10.6061/clinics/2015\(07\)09](https://doi.org/10.6061/clinics/2015(07)09).
48. Manicklal S, Emery VC, Lazzarotto T, Boppana SB, Gupta RK. 2013. The “silent” global burden of congenital cytomegalovirus. *Clin Microbiol Rev* 26:86–102. <https://doi.org/10.1128/CMR.00062-12>.
49. Reddehase MJ, Lemmermann NAW. 2018. Mouse model of cytomegalovirus disease and immunotherapy in the immunocompromised host: predictions for medical translation that survived the “test of time.” *Viruses* 10:693. <https://doi.org/10.3390/v10120693>.
50. Fisher MA, Lloyd ML. 2020. A review of murine cytomegalovirus as a model for human cytomegalovirus disease—do mice lie? *Int J Mol Sci* 22:214. <https://doi.org/10.3390/ijms22010214>.
51. Zhan X, Lee M, Abenes G, Von Reis I, Kittinunvorakoon C, Ross-Macdonald P, Snyder M, Liu F. 2000. Mutagenesis of murine cytomegalovirus using a Tn3-based transposon. *Virology* 266:264–274. <https://doi.org/10.1006/viro.1999.0089>.
52. Zimmermann A, Trilling M, Wagner M, Wilborn M, Bubic I, Jonjic S, Koszinowski U, Hengel H. 2005. A cytomegaloviral protein reveals a dual role for STAT2 in IFN- $\gamma$  signaling and antiviral responses. *J Exp Med* 201:1543–1553. <https://doi.org/10.1084/jem.20041401>.
53. Döring M, Lessin I, Frenz T, Spanier J, Kessler A, Tegtmeyer P, Dağ F, Thiel N, Trilling M, Lienenklaus S, Weiss S, Scheu S, Messerle M, Cicin-Sain L, Hengel H, Kalinke U. 2014. M27 expressed by cytomegalovirus counteracts effective type I interferon induction of myeloid cells but not of plasmacytoid dendritic cells. *J Virol* 88:13638–13650. <https://doi.org/10.1128/JVI.00216-14>.
54. Chan B, Magalhães VG, Lemmermann NAW, Lisnić VJ, Stempel M, Bussey KA, Reimer E, Podlech J, Lienenklaus S, Reddehase MJ, Jonjić S, Brinkmann MM. 2017. The murine cytomegalovirus M35 protein antagonizes type I IFN induction downstream of pattern recognition receptors by targeting NF- $\kappa$ B mediated transcription. *PLoS Pathog* 13:e1006382. <https://doi.org/10.1371/journal.ppat.1006382>.
55. Stempel M, Chan B, Juranić Lisnić V, Krmpotić A, Hartung J, Paludan SR, Füllbrunn N, Lemmermann NA, Brinkmann MM. 2019. The herpesviral antagonist m152 reveals differential activation of STING-dependent IRF and NF- $\kappa$ B signaling and STING’s dual role during MCMV infection. *EMBO J* 38:e100983. <https://doi.org/10.15252/emboj.2018100983>.
56. Liu Y, Biegalka BJ. 2002. The human cytomegalovirus UL35 gene encodes two proteins with different functions. *J Virol* 76:2460–2468. <https://doi.org/10.1128/jvi.76.5.2460-2468.2002>.
57. Fabits M, Gonçalves Magalhães V, Chan B, Girault V, Elbasani E, Rossetti E, Saeland E, Messerle M, Pichlmair A, Lisnić VJ, Brinkmann MM. 2020. The cytomegalovirus tegument protein UL35 antagonizes pattern recognition receptor-mediated type I IFN transcription. *Microorganisms* 8:790. <https://doi.org/10.3390/microorganisms8060790>.
58. Munshi N, Agalioti T, Lomvardas S, Merika M, Chen G, Thanos D. 2001. Coordination of a transcriptional switch by HMG(Y) acetylation. *Science* 293:1133–1136. <https://doi.org/10.1126/science.293.5532.1133>.
59. Apostolou E, Thanos D. 2008. Virus infection induces NF- $\kappa$ B-dependent interchromosomal associations mediating monoallelic IFN- $\beta$  gene expression. *Cell* 134:85–96. <https://doi.org/10.1016/j.cell.2008.05.052>.
60. Wang B, Nishimura M, Tang H, Kawabata A, Mahmoud NF, Khanlari Z, Hamada D, Tsuruta H, Mori Y. 2016. Crystal structure of human herpesvirus 6B tegument protein U14. *PLoS Pathog* 12:e1005594. <https://doi.org/10.1371/journal.ppat.1005594>.
61. Panne D. 2008. The enhanceosome. *Curr Opin Struct Biol* 18:236–242. <https://doi.org/10.1016/j.sbi.2007.12.002>.
62. Lefort S, Soucy-Faulkner A, Grandvaux N, Flamand L. 2007. Binding of Kaposi’s sarcoma-associated herpesvirus K-bZIP to interferon-responsive factor 3 elements modulates antiviral gene expression. *J Virol* 81:10950–10960. <https://doi.org/10.1128/JVI.00183-07>.
63. Fu Y-Z, Su S, Zou H-M, Guo Y, Wang S-Y, Li S, Luo M-H, Wang Y-Y. 2019. Human cytomegalovirus DNA polymerase subunit UL44 antagonizes antiviral immune responses by suppressing IRF3- and NF- $\kappa$ B-mediated transcription. *J Virol* 93:e00181-19. <https://doi.org/10.1128/JVI.00181-19>.
64. Cloutier N, Flamand L. 2010. Kaposi sarcoma-associated herpesvirus latency-associated nuclear antigen inhibits interferon (IFN) beta expression by competing with IFN regulatory factor-3 for binding to IFNB promoter. *J Biol Chem* 285:7208–7221. <https://doi.org/10.1074/jbc.M109.018838>.
65. Eilbrecht M, Le-Trilling VTK, Trilling M. 2020. Mouse cytomegalovirus M34 encodes a non-essential, nuclear, early-late expressed protein required for efficient viral replication. *Front Cell Infect Microbiol* 10:171. <https://doi.org/10.3389/fcimb.2020.00171>.
66. Gompels UA, Nicholas J, Lawrence G, Jones M, Thomson BJ, Martin ME, Efstathiou S, Craxton M, Macaulay HA. 1995. The DNA sequence of human herpesvirus-6: structure, coding content, and genome evolution. *Virology* 209:29–51. <https://doi.org/10.1006/viro.1995.1228>.
67. Nicholas J. 1996. Determination and analysis of the complete nucleotide sequence of human herpesvirus. *J Virol* 70:5975–5989. <https://doi.org/10.1128/JVI.70.9.5975-5989.1996>.
68. Isegawa Y, Mukai T, Nakano K, Kagawa M, Chen J, Mori Y, Sunagawa T, Kawanishi K, Sashihara J, Hata A, Zou P, Kosuge H, Yamanishi K. 1999. Comparison of the complete DNA sequences of human herpesvirus 6 variants A and B. *J Virol* 73:8053–8063. <https://doi.org/10.1128/JVI.73.10.8053-8063.1999>.
69. Harteis S, Schneider S. 2014. Making the bend: DNA tertiary structure and protein-DNA interactions. *Int J Mol Sci* 15:12335–12363. <https://doi.org/10.3390/ijms150712335>.
70. Schoggins JW, MacDuff DA, Imanaka N, Gainey MD, Shrestha B, Eitson JL, Mar KB, Richardson RB, Ratushny AV, Litvak V, Dabelic R, Manicassamy B, Aitchison JD, Aderem A, Elliott RM, García-Sastre A, Racaniello V, Snijder EJ, Yokoyama WM, Diamond MS, Virgin HW, Rice CM. 2014. Pan-viral specificity of IFN-induced genes reveals new roles for cGAS in innate immunity. *Nature* 505:691–695. <https://doi.org/10.1038/nature12862>.
71. Herzog VA, Reichholf B, Neumann T, Rescheneder P, Bhat P, Burkard TR, Wlotzka W, von Haeseler A, Zuber J, Ameres SL. 2017. Thiol-linked alkylation of RNA to assess expression dynamics. *Nat Methods* 14:1198–1204. <https://doi.org/10.1038/nmeth.4435>.
72. Muhar M, Ebert A, Neumann T, Umkehrer C, Jude J, Wieshofer C, Rescheneder P, Lipp JJ, Herzog VA, Reichholf B, Cisneros DA, Hoffmann T, Schlapansky MF, Bhat P, von Haeseler A, Köcher T, Obenauf AC, Popow J, Ameres SL, Zuber J. 2018. SLAM-seq defines direct gene-regulatory functions of the BRD4-MYC axis. *Science* 360:800–805. <https://doi.org/10.1126/science.aao2793>.
73. Lio C-WJ, McDonald B, Takahashi M, Dhanwani R, Sharma N, Huang J, Pham E, Benedict CA, Sharma S. 2016. cGAS-STING signaling regulates initial innate control of cytomegalovirus infection. *J Virol* 90:7789–7797. <https://doi.org/10.1128/JVI.01040-16>.
74. Shaw AE, Hughes J, Gu Q, Behdenna A, Singer JB, Dennis T, Orton RJ, Varela M, Gifford RJ, Wilson SJ, Palmarini M. 2017. Fundamental properties of the mammalian innate immune system revealed by multispecies comparison of type I interferon responses. *PLoS Biol* 15:e2004086. <https://doi.org/10.1371/journal.pbio.2004086>.
75. Pattison MJ, Mackenzie KF, Arthur JSC. 2012. Inhibition of JAKs in macrophages increases lipopolysaccharide-induced cytokine production by blocking IL-10-mediated feedback. *J Immunol* 189:2784–2792. <https://doi.org/10.4049/jimmunol.1200310>.
76. Stempel M, Chan B, Brinkmann MM. 2019. Coevolution pays off: herpesviruses have the license to escape the DNA sensing pathway. *Med Microbiol Immunol* 208:495–512. <https://doi.org/10.1007/s00430-019-00582-0>.
77. Aktar S, Ariei J, Tjan LH, Nishimura M, Mori Y. 2021. Human herpesvirus 6A tegument protein U14 induces NF- $\kappa$ B signaling by interacting with p65. *J Virol* 95:e01269-21. <https://doi.org/10.1128/JVI.01269-21>.
78. Agalioti T, Lomvardas S, Parekh B, Yie J, Maniatis T, Thanos D. 2000. Ordered recruitment of chromatin modifying and general transcription factors to the IFN- $\beta$  promoter. *Cell* 103:667–678. [https://doi.org/10.1016/s0092-8674\(00\)00169-0](https://doi.org/10.1016/s0092-8674(00)00169-0).
79. Dragan AI, Hargreaves VV, Makeyeva EN, Privalov PL. 2007. Mechanisms of activation of interferon regulator factor 3: the role of C-terminal domain phosphorylation in IRF-3 dimerization and DNA binding. *Nucleic Acids Res* 35:3525–3534. <https://doi.org/10.1093/nar/gkm142>.
80. Sahara W, Yoneyama M, Kitabayashi I, Fujita T. 2002. Direct involvement of CREB-binding protein/p300 in sequence-specific DNA binding of virus-activated interferon regulatory factor-3 holocomplex. *J Biol Chem* 277:22304–22313. <https://doi.org/10.1074/jbc.M200192200>.
81. Yang H, Lin CH, Ma G, Orr M, Baffi MO, Wathélet MG. 2002. Transcriptional activity of interferon regulatory factor (IRF)-3 depends on multiple protein-protein interactions. *Eur J Biochem* 269:6142–6151. <https://doi.org/10.1046/j.1432-1033.2002.03330.x>.
82. Fossum E, Friedel CC, Rajagopala SV, Titz B, Baiker A, Schmidt T, Kraus T, Stellberger T, Rutenberg C, Suthram S, Bandyopadhyay S, Rose D, von Brunn A, Uhlmann M, Zeretzke C, Dong Y-A, Boulet H, Koegl M, Bailor

- SM, Koszinowski U, Ideker T, Uetz P, Zimmer R, Haas J. 2009. Evolutionarily conserved herpesviral protein interaction networks. *PLoS Pathog* 5:e1000570. <https://doi.org/10.1371/journal.ppat.1000570>.
83. Wilhelm BT, Landry J-R. 2009. RNA-Seq-quantitative measurement of expression through massively parallel RNA-sequencing. *Methods* 48:249–257. <https://doi.org/10.1016/j.jymeth.2009.03.016>.
84. Zhao S, Fung-Leung W-P, Bittner A, Ngo K, Liu X. 2014. Comparison of RNA-Seq and microarray in transcriptome profiling of activated T cells. *PLoS One* 9:e78644. <https://doi.org/10.1371/journal.pone.0078644>.
85. Ourthague DR, Birnbaum H, Ortenlöf N, Vargas JD, Wollman R, Hoffmann A. 2015. Limited specificity of IRF3 and ISGF3 in the transcriptional innate-immune response to double-stranded RNA. *J Leukoc Biol* 98:119–128. <https://doi.org/10.1189/jlb.4A1014-483RR>.
86. Shepardson KM, Larson K, Johns LL, Stanek K, Cho H, Wellham J, Henderson H, Rynda-Apple A. 2018. IFNAR2 is required for anti-influenza immunity and alters susceptibility to post-influenza bacterial superinfections. *Front Immunol* 9:2589. <https://doi.org/10.3389/fimmu.2018.02589>.
87. Lewerenz M, Mogensen KE, Uzé G. 1998. Shared receptor components but distinct complexes for  $\alpha$  and  $\beta$  interferons. *J Mol Biol* 282:585–599. <https://doi.org/10.1006/jmbi.1998.2026>.
88. Kropp KA, Hsieh WY, Isern E, Forster T, Krause E, Brune W, Angulo A, Ghazal P. 2015. A temporal gate for viral enhancers to co-opt Toll-like-receptor transcriptional activation pathways upon acute infection. *PLoS Pathog* 11:e1004737. <https://doi.org/10.1371/journal.ppat.1004737>.
89. Hatesuer B, Hoang HTT, Riese P, Trittel S, Gerhauer I, Elbahesh H, Geffers R, Wilk E, Schughart K. 2017. Deletion of Irf3 and Irf7 genes in mice results in altered interferon pathway activation and granulocyte-dominated inflammatory responses to influenza A infection. *J Innate Immun* 9:145–161. <https://doi.org/10.1159/000450705>.
90. Müller U, Steinhoff U, Reis LF, Hemmi S, Pavlovic J, Zinkernagel RM, Aguet M. 1994. Functional role of type I and type II interferons in antiviral defense. *Science* 264:1918–1921. <https://doi.org/10.1126/science.8009221>.
91. Podlech J, Holtappels R, Grzimek NKA, Reddehase MJ. 2002. Animal models: murine cytomegalovirus, p 493-IN11. In *Methods in microbiology*. Academic Press, Cambridge, MA.
92. Erlandsson L, Blumenthal R, Eloranta ML, Engel H, Alm G, Weiss S, Leanderson T. 1998. Interferon-beta is required for interferon-alpha production in mouse fibroblasts. *Curr Biol* 8:223–226. [https://doi.org/10.1016/s0960-9822\(98\)70086-7](https://doi.org/10.1016/s0960-9822(98)70086-7).
93. Yoneyama M, Suhara W, Fukuhara Y, Sato M, Ozato K, Fujita T. 1996. Autocrine amplification of type I interferon gene expression mediated by interferon stimulated gene factor 3 (ISGF3). *J Biochem* 120:160–169. <https://doi.org/10.1093/oxfordjournals.jbchem.a021379>.
94. Kawai T, Takahashi K, Sato S, Coban C, Kumar H, Kato H, Ishii KJ, Takeuchi O, Akira S. 2005. IPS-1, an adaptor triggering RIG-I- and Mda5-mediated type I interferon induction. *Nat Immunol* 6:981–988. <https://doi.org/10.1038/ni1243>.
95. Basler CF, Mikulasova A, Martinez-Sobrido L, Paragas J, Mühlberger E, Bray M, Klenk H-D, Palese P, Garcia-Sastre A. 2003. The ebola virus VP30 protein inhibits activation of interferon regulatory factor 3. *J Virol* 77:7945–7956. <https://doi.org/10.1128/jvi.77.14.7945-7956.2003>.
96. Munks MW, Gold MC, Zajac AL, Doom CM, Morello CS, Spector DH, Hill AB. 2006. Genome-wide analysis reveals a highly diverse CD8 T cell response to murine cytomegalovirus. *J Immunol* 176:3760–3766. <https://doi.org/10.4049/jimmunol.176.6.3760>.
97. Li MZ, Elledge SJ. 2012. SLIC: a method for sequence- and ligation-independent cloning. *Methods Mol Biol* 852:51–59. [https://doi.org/10.1007/978-1-61779-564-0\\_5](https://doi.org/10.1007/978-1-61779-564-0_5).
98. Bleckmann M, Fritz MH-Y, Bhujra S, Jarek M, Schüring M, Geffers R, Benes V, Besir H, van den Heuvel J. 2015. Genomic analysis and isolation of RNA polymerase II dependent promoters from *Spodoptera frugiperda*. *PLoS One* 10:e0132898. <https://doi.org/10.1371/journal.pone.0132898>.
99. Karste K, Bleckmann M, van den Heuvel J. 2017. Not limited to *E. coli*: versatile expression vectors for mammalian protein expression. *Methods Mol Biol* 1586:313–324. [https://doi.org/10.1007/978-1-4939-6887-9\\_20](https://doi.org/10.1007/978-1-4939-6887-9_20).
100. Schindelin J, Arganda-Carreras I, Frise E, Kaynig V, Longair M, Pietzsch T, Preibisch S, Rueden C, Saalfeld S, Schmid B, Tinevez J-Y, White DJ, Hartenstein V, Eliceiri K, Tomancak P, Cardona A. 2012. Fiji: an open-source platform for biological-image analysis. *Nat Methods* 9:676–682. <https://doi.org/10.1038/nmeth.2019>.
101. Burkhardt A, Pakendorf T, Reime B, Meyer J, Fischer P, Stübe N, Panteerselvam S, Lorbeer O, Stachnik K, Warmer M, Rödiger P, Göries D, Meenters A. 2016. Status of the crystallography beamlines at PETRA III. *Eur Phys J Plus* 131:56. <https://doi.org/10.1140/epjp/i2016-16056-0>.
102. Vonrhein C, Flensburg C, Keller P, Sharff A, Smart O, Paciorek W, Womack T, Bricogne G. 2011. Data processing and analysis with the autoPROC toolbox. *Acta Crystallogr D Biol Crystallogr* 67:293–302. <https://doi.org/10.1107/S0907444911007773>.
103. Tickle IJ, Flensburg C, Keller P, Paciorek W, Sharff A, Vonrhein C, Bricogne G. 2018. STARANISO. Global Phasing Ltd., Cambridge, UK.
104. McCoy AJ, Grosse-Kunstleve RW, Adams PD, Winn MD, Storoni LC, Read RJ. 2007. Phaser crystallographic software. *J Appl Crystallogr* 40:658–674. <https://doi.org/10.1107/S0021889807021206>.
105. Emsley P, Lohkamp B, Scott WG, Cowtan K. 2010. Features and development of COOT. *Acta Crystallogr D Biol Crystallogr* 66:486–501. <https://doi.org/10.1107/S0907444910007493>.
106. Liebschner D, Afonine PV, Baker ML, Bunkóczi G, Chen VB, Croll TI, Hintze B, Hung L-W, Jain S, McCoy AJ, Moriarty NW, Oeffner RD, Poon BK, Prisant MG, Read RJ, Richardson JS, Richardson DC, Sammito MD, Sobolev OV, Stockwell DH, Terwilliger TC, Urzhumtsev AG, Videau LL, Williams CJ, Adams PD. 2019. Macromolecular structure determination using X-rays, neutrons and electrons: recent developments in Phenix. *Acta Crystallogr D Struct Biol* 75:861–877. <https://doi.org/10.1107/S2059798319011471>.
107. Schrödinger, LLC. 2015. PyMOL molecular graphics system, version 1.8. Schrödinger, LLC, New York, NY.
108. Robitaille AC, Mariani MK, Fortin A, Grandvaux N. 2016. A high resolution method to monitor phosphorylation-dependent activation of IRF3. *J Vis Exp*:e53723.
109. Lefkowitz EJ, Dempsey DM, Hendrickson RC, Orton RJ, Suddell SG, Smith DB. 2018. Virus taxonomy: the database of the International Committee on Taxonomy of Viruses (ICTV). *Nucleic Acids Res* 46:D708–D717. <https://doi.org/10.1093/nar/gkx932>.
110. James S, Donato D, de Thoisy B, Lavergne A, Lacoste V. 2020. Novel herpesviruses in neotropical bats and their relationship with other members of the *Herpesviridae* family. *Infect Genet Evol* 84:104367. <https://doi.org/10.1016/j.meegid.2020.104367>.
111. Sievers F, Wilm A, Dineen D, Gibson TJ, Karplus K, Li W, Lopez R, McWilliam H, Remmert M, Söding J, Thompson JD, Higgins DG. 2011. Fast, scalable generation of high-quality protein multiple sequence alignments using Clustal Omega. *Mol Syst Biol* 7:539. <https://doi.org/10.1038/msb.2011.75>.
112. Madeira F, Pearce M, Tivey ARN, Basutkar P, Lee J, Edbali O, Madhusoodanan N, Kolesnikov A, Lopez R. 2022. Search and sequence analysis tools services from EMBL-EBI in 2022. *Nucleic Acids Res* 50:W276–W279. <https://doi.org/10.1093/nar/gkac240>.
113. Kumar S, Stecher G, Li M, Knyaz C, Tamura K. 2018. MEGA X: molecular evolutionary genetics analysis across computing platforms. *Mol Biol Evol* 35:1547–1549. <https://doi.org/10.1093/molbev/msy096>.
114. Waterhouse AM, Procter JB, Martin DMA, Clamp M, Barton GJ. 2009. Jalview version 2—a multiple sequence alignment editor and analysis workbench. *Bioinformatics* 25:1189–1191. <https://doi.org/10.1093/bioinformatics/btp033>.
115. Langmead B, Trapnell C, Pop M, Salzberg SL. 2009. Ultrafast and memory-efficient alignment of short DNA sequences to the human genome. *Genome Biol* 10:R25. <https://doi.org/10.1186/gb-2009-10-3-r25>.
116. Dobin A, Davis CA, Schlesinger F, Drenkow J, Zaleski C, Jha S, Batut P, Chaisson M, Gingeras TR. 2013. STAR: ultrafast universal RNA-seq aligner. *Bioinformatics* 29:15–21. <https://doi.org/10.1093/bioinformatics/bts635>.
117. Jürges C, Dölken L, Erhard F. 2018. Dissecting newly transcribed and old RNA using GRAND-SLAM. *Bioinformatics* 34:i218–i226. <https://doi.org/10.1093/bioinformatics/bty256>.
118. Rummel T, Sakellaridi L, Erhard F. 2022. grandR: a comprehensive package for nucleotide deconvolution sequencing data analysis. *bioRxiv*. <https://doi.org/10.1101/2022.09.12.507665>.
119. Love MI, Huber W, Anders S. 2014. Moderated estimation of fold change and dispersion for RNA-seq data with DESeq2. *Genome Biol* 15:50. <https://doi.org/10.1186/s13059-014-0550-8>.
120. Erhard F. 2018. Estimating pseudocounts and fold changes for digital expression measurements. *Bioinformatics* 34:4054–4063. <https://doi.org/10.1093/bioinformatics/bty471>.
121. Matys V, Kel-Margoulis OV, Fricke E, Liebich I, Land S, Barre-Dirrie A, Reuter I, Chekmenev D, Krull M, Hornischer K, Voss N, Stegmaier P, Lewicki-Potapov B, Saxel H, Kel AE, Wingender E. 2006. TRANSFAC and its module TRANS-Compel: transcriptional gene regulation in eukaryotes. *Nucleic Acids Res* 34:D108–D110. <https://doi.org/10.1093/nar/gkj143>.
122. Raudvere U, Kolberg L, Kuzmin I, Arak T, Adler P, Peterson H, Vilo J. 2019. g:Profiler: a web server for functional enrichment analysis and conversions of gene lists (2019 update). *Nucleic Acids Res* 47:W191–W198. <https://doi.org/10.1093/nar/gkz369>.